2024-08-09

Extreme Ultraviolet and Xray Applications of Carbon Nanotube Devices

Scott Olsen
Brigham Young University

Extreme Ultraviolet and Xray Applications of Carbon Nanotube Devices

Scott Olsen

A dissertation submitted to the faculty of
Brigham Young University
in partial fulfillment of the requirements for the degree of

Doctor of Philosophy

Richard Vanfleet, Chair
David Allred
Vance Robinson
Robert Davis
Ben Frandsen

Department of Physics and Astronomy

Brigham Young University

ABSTRACT

Extreme Ultraviolet and Xray Applications of Carbon Nanotube Devices

Scott Olsen
Department of Physics and Astronomy, BYU
Doctor of Philosophy

The vacuum ultraviolet (VUV), extreme ultraviolet (EUV) and xray ranges of the electromagnetic spectrum have many unique properties and applications, such as medical treatment, photolithography, and astronomical observation. However, these applications require unique optical element designs, setups, and materials. carbon nanotubes (CNTs) are a fascinating material with thermal, mechanical, and chemical properties that may be beneficial for VUV, EUV, and xray applications. They are conductive, can be patterned into high aspect ratio structures, and are stable in high temperature vacuum. In this work, we report several carbon nanotube devices developed for the VUV, EUV, and xray range. These devices include a CNT collimator with peak VUV transmission over 18% and a pressure differential of 0.001 or less, a vertically aligned CNT array field emitter that can withstand fields up to 1.16 V/μm and emit up to 3 mA of current, a CNT lobster eye optic concept to act as a wide bandpass lens, a CNT zone plate array for xray lithography, a doped vertically aligned CNT array as a laser-induced plasma target for EUV and xray production, and a CNT high harmonic generation device for EUV production.

Keywords: Carbon nanotubes, vacuum ultraviolet, extreme ultraviolet, xray, hollow cathode, McPherson 629, collimation, differential pumping, field emission, vertically aligned carbon nanotube arrays

Contents

List of Figures

List of Tables

Chapter 1

Introduction

The vacuum ultraviolet (VUV), extreme ultraviolet (EUV) and xray ranges of the electromagnetic spectrum (approximately 100 nm wavelength to 0.1 nm wavelength) have many unique properties and applications. VUV is used in medical treatment, surface cleaning, and sterilization (1); it can be used to characterize soft materials such as polymers (2) and other complex materials (3); and for observing astronomical phenomena (4). EUV has also been used for observing astronomical phenomena on several missions ((5), (6)), and it is also a good candidate for lithography- it's shorter wavelength allows for smaller and finer features (7). Xray lithography is also a promising field for improving semiconductor fabrication (8).

The unique properties of these electromagnetic ranges are due to their high absorbance with all materials and their refractive index being less than one. However, this means that unique optical element designs, setups, and materials are necessary (7). Devices such as zone plates, windowless vacuum transitions, multilayered mirrors, and others require much work in design and fabrication.

In this work, we consider the applications of carbon nanotubes (CNTs) in these electromagnetic ranges. Their unique thermal, mechanical, and chemical properties make them stable at high temperatures and within high vacuum environments (9). They can be grown into various structures with high aspect ratios using simple fabrication processes. These structures can also be infiltrated

with a filler material. The resulting structures have the shape of the grown CNT bulk (called a forest), but the properties of the filler material (10).

We utilized the unique properties of CNTs to develop several devices for VUV, EUV, and xray applications. Our work is organized as follows:

- Empirical analysis of a hollow cathode's intensity distribution in the vacuum ultraviolet range (accepted into JVST A).
- Carbon nanotube collimator as a vacuum ultraviolet window (accepted into JVST B).
- Field emission from flipped and patterned vertically aligned carbon nanotube arrays (under revision for Nanotechnology).

A conclusion summarizes discoveries made and discusses current and future work. After the conclusion are several appendices that discuss other applications. These applications were incomplete or unsuccessful and are provided here for documentation.

1.1 References

Bibliography

[1] S. Zhao, M. Djavid, and Z. Mi. Surface emitting, high efficiency near-vacuum ultraviolet light source with aluminum nitride nanowires monolithically grown on silicon. *Nano Lett.*, 15:7006–7009, 2015.

[2] M. Kaku, D. Kai, M. Katto, A. Yokotani, S. Kubodera, and W. Sasaki. Surface analysis by photo-stimulated desorption using tunable VUV radiation. *Appl. Phys. B*, 119:427–433, 2015.

[3] A. Lelevic, V. Souchon, M. Moreaud, C. Lorentz, and C. Geantet. Gas chromatography vacuum ultraviolet spectroscopy: A review. *J. Sep. Sci.*, 43:150–173, 2019.

[4] W. Zheng, J.Lemin, and F. Huang. Vacuum-ultraviolet photon detections. *iScience*, 23, 2020.

[5] R.S. Warwick. *EUV Astronomy with the Rosat Wide Field Camera*, pages 57–66. Springer Netherlands, Dordrecht, 1994.

[6] M.M. Sirk, J.V. Vallerga, D.S. Finley, P. Jelinsky, and R.F. Malina. Performance of the extreme ultraviolet explorer imaging telescopes. *The Astrophysical Journal*, 110:347–356, 1997.

[7] D. Attwood and A. Sakdinawat. Cambridge University Press, 2 edition, 2016.

[8] F. Cerrina. X-ray imaging: applications to patterning and lithography. *Journal of Physics D: Applied Physics*, 33:R103–R116, 2000.

[9] Bocharov G and Eletskii A. Theory of Carbon Nanotube (CNT)-Based Electron Field Emitters. *Nanomaterials-Basel*, 3:393–442, 2013.

[10] D. Hutchison, N. Morrill, Q. Aten, B. Turner, B. Jensen, L. Howell, R. Vanfleet, and R. Davis. Carbon nanotubes as a framework for high-aspect-ratio MEMs fabrication. *J Microelectromech S*, 19(1):75–82, 2010.

Chapter 2

Empirical analysis of a hollow cathode's intensity distribution in the vacuum ultraviolet range

2.1 Abstract

(A version of this chapter has been accepted into JVST A) Hollow cathodes are a common type of vacuum ultraviolet light (VUV) source with a wide range of design and application. We determined the VUV (58.4 nm) intensity distribution of a hollow cathode as a function of current and pressure. Our model describes the intensity distribution of a McPherson 629-like hollow cathode helium plasma within the range of 0.50-1.00 A and 0.50-1.00 torr as a ring with a center peak. We found that for all pressures and currents considered, the ring emits more VUV light than the center peak. We also found that the center peak has a minimum VUV light emission near 0.9 torr.

2.2 Introduction

Vacuum ultraviolet light (VUV) has many applications in many fields. It is used for medical treatment, surface, cleaning, and sterilization (1); for characterizing soft materials such as polymers (2); for improving analysis of complex samples (3); and for observing astronomical phenomena that may influence life on earth (4). Common sources of VUV are windowless discharge lamps that involve a hollow cathode and a capillary. Many designs have been reported over the years (5), such as a cone-shaped cathode with 700 μm diameter bore for emission below 140 nm (6), a pulsed microdischarge for achieving higher VUV efficiency than common DC discharges (7), and table-top sources with controllable wavelength and polarization (8). With the applications and designs of VUV discharge lamps being so broad, knowledge of the lamp's intensity distribution would be beneficial in maximizing VUV flux.

Hollow cathodes are a commonly used cathode design. They have been known for decades to increase the current and emission of plasmas. The negative glow region, where much of the radiation is emitted, tends to reside within the bore of the cathode. With the proper operating pressure and anode alignment, the light emission consists of very intense and very narrow spectral lines of the discharge gas (9). This is due to what is called the pendulum effect-electrons inside the bore oscillate across the bore. This creates more secondary electrons as the primary electrons make their way to the end of the bore (10).

The intensity distribution of the light emitted by a hollow cathode plasma depends on the pressure, current, and wavelength being observed. A few works have observed the intensity distribution of a hollow cathode at various parameters. In many of these works, the distribution is described as radially symmetric with either a peak at the center or along the edges (9), (11), (12). The peaks are understood to be the negative glow regions of the plasma (13), therefore the conditions where the center peak is separated into peaks along the edges (a ring around around the hollow cathode bore) is understood to be the conditions where the negative glow regions from the

opposing sides of the bore separate to form an inner dark space.

Though much work has been done to describe hollow cathode intensity distributions in the visible, there is limited work in the literature that reports the intensity distribution of hollow cathode plasmas in the VUV range. In this work, we considered a hollow cathode helium plasma with a cathode design similar to a McPherson 629 model (14). The wavelength observed was 58.4 nm. The plasma was run at various pressure and current values ranging from 1.00 torr, 1.00 A to 0.50 torr, 0.50 A. We developed an empirical model for the intensity distribution of VUV as a function of current and pressure.

2.3 Methods

Fig 2.1 shows a photograph and a diagram of the system used in the experiment. The system was built on an optical table. A box was constructed around the system to block out stray light from other sources such as the room lights. The system had three main components: an upper chamber where a plasma is ignited and maintained, a lower chamber where the VUV distribution may be observed, and an aperture between them. For the upper chamber, we used a hollow cathode helium plasma (similar to a McPherson 629 design) connected to a helium line and a high voltage power supply (Universal Voltronics Corp.). We selected this hollow cathode design because it is known to be very durable, have a stable emission output(15), and is an excellent source for VUV spectroscopy. The helium line included a sapphire leak valve (Varian, model number 951-5106) to control the pressure. The upper chamber was connected to a roughing pump (W.M. Welch Manufacturing Company), a turbomolecular pump (Leybold TurboVac 50), a residual gas analyzer (RGA, ExTorr Inc., model number XT100), and a micropirani pressure gauge (MKS 925 MicroPirani Transducer, part number 925-61025). At the base of the upper chamber a 3 mm deep well was machined for placement of the aperture.

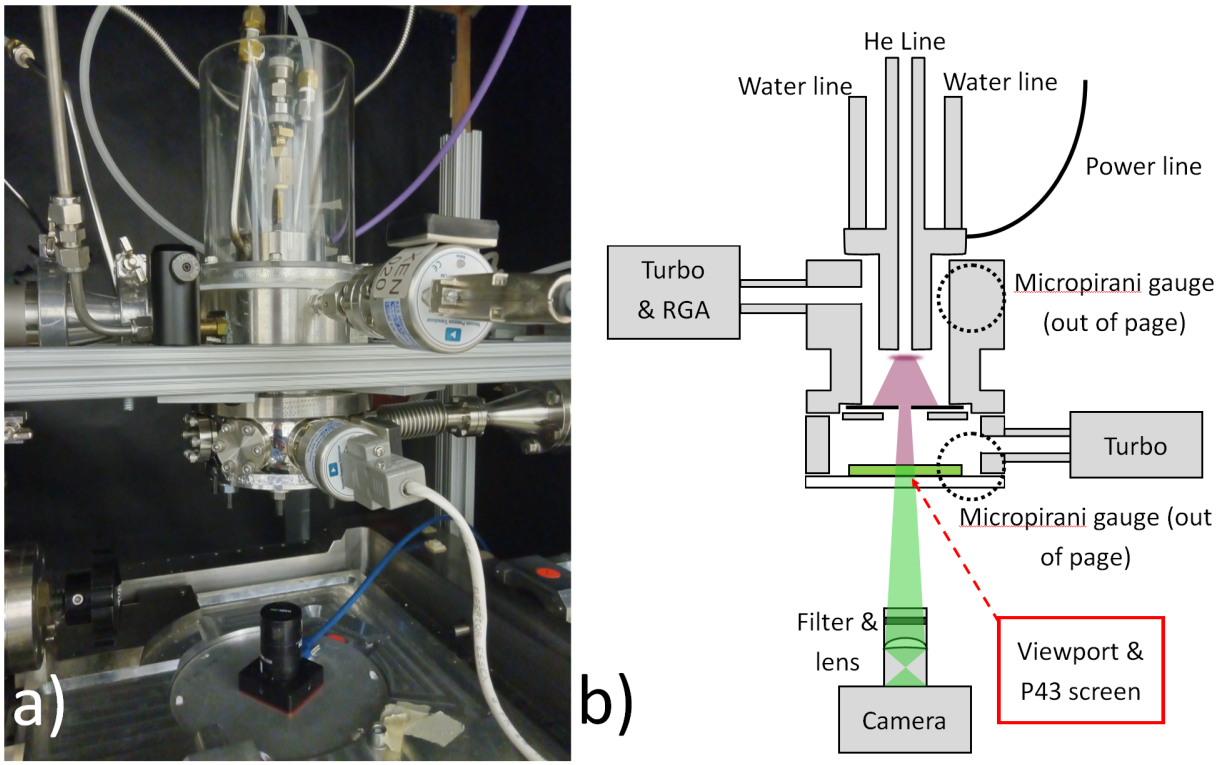

Figure 2.1 a) A photo of the system used to observe the hollow cathode plasma's intensity distribution in the VUV range (58.4 nm). The upper chamber is an anode for a McPherson 629-like hollow cathode. The lower chamber is for observing the VUV emission. Turbo-molecular pumps, roughing pump, and RGA are not shown. Micropirani gauges can seen coming out of the page. The horizontal bar is part of a frame constructed to suspend the chamber above a camera. b) A diagram of the system. Note that the diagram is not drawn to scale.

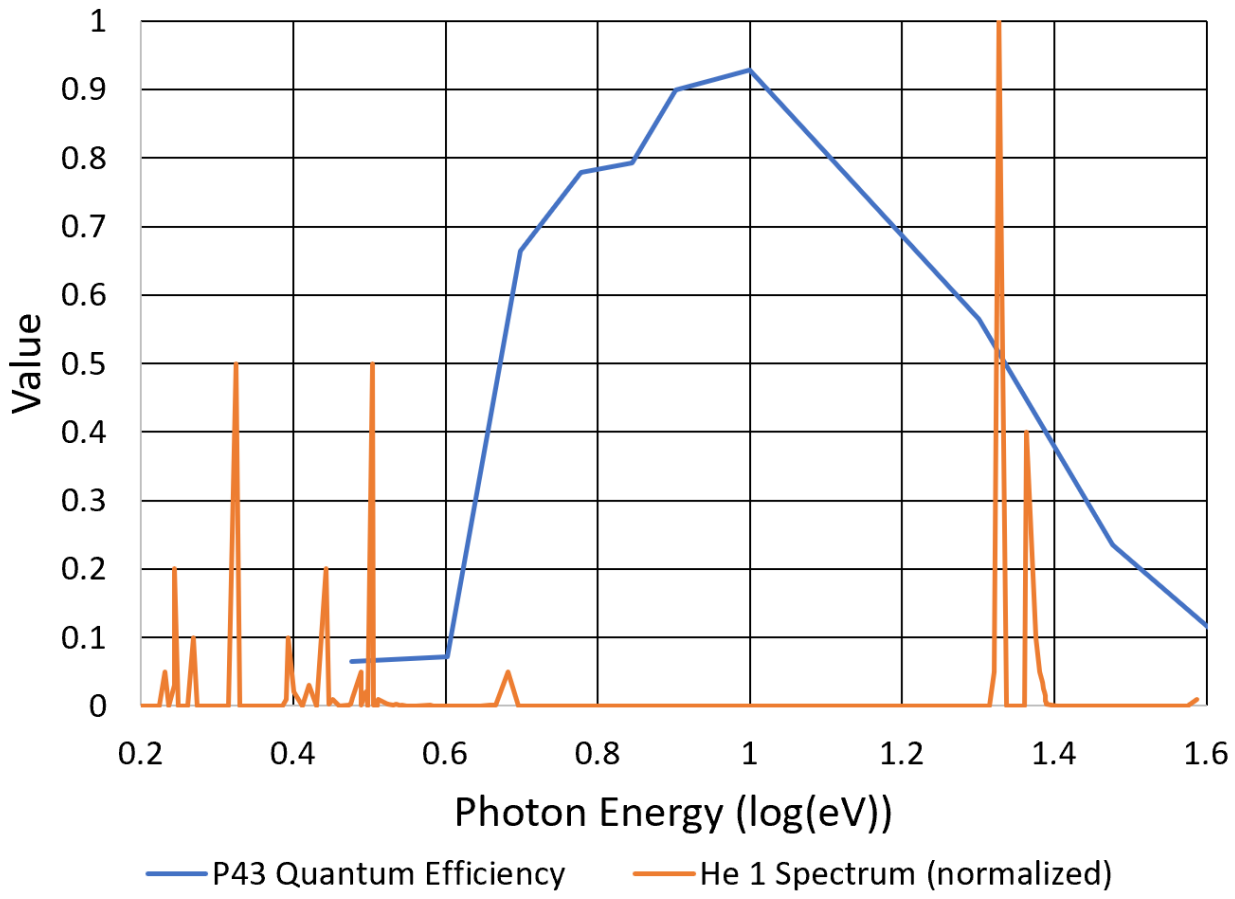

Figure 2.2 The normalized spectrum of neutral helium emission lines provided by NIST(16) plotted against the responsivity of P43 phosphor provided by Proxivision(17). Note that the 58.4 nm line has the greatest intensity and responsitivity.

The lower chamber was a Kimball Physics 4.5-inch spherical octagon chamber with tapped holes (model number MCF450-SphOct-E2A8) connected to the upper chamber via one of the 4.5-inch CF sealing surfaces. The other 4.5-inch CF surface was sealed with an acrylic viewport. A P43 phosphor window (custom made by Scintek) was held in place over the viewport with a polyimide film. Plotting the helium's emission spectrum(16) with the responsivity of P43 (provided by Proxivision(17)) shows that the only wavelength we expect to fluoresce the phosphor is 58.4 nm (peak near 1.3 log(eV) in Fig 2.2). The side ports of the chamber were connected to the roughing pump, a turbomolecular pump (Leybold TurboVac 50, 50 L/s for helium), and a micropirani gauge.

About 168 mm underneath the viewport was a camera (ThorLab 1.6 MP CMOS compact scientific camera, item number CS165MU) with a 543.5 nm laser line filter (10 ± 2 nm FWHM, ThorLab part number FL543.5-10) and a focusing lens (25 mm focal length).

The aperture was a 0.3 mm thick shim stock diaphragm with a 2.1 mm diameter aperture. It was mounted into the machined well using a custom designed plate with wide bolt holes along its edge. The wide bolt holes enabled aperture alignment with the optical axis (described later).

The experiment procedure began with opening the box, removing the camera from underneath the octagon chamber, and removing the chamber from the lower chamber. After removing the plate and aperture, the cathode and anode were cleaned of tarnish using an emery cloth and IPA.

Fig 3.4 shows the steps of aligning the aperture with the optical axis. The helium line to the cathode was removed and a LED light was inserted into the cathode bore with the wires exiting through the helium line connection. When the LED was turned on, the light exiting the cathode bore made a circle on a screen placed about 654 mm from the bore. The circle was traced on the screen and the center of the circle marked. A second screen placed about 249 mm from the bore was inserted into the optical path. A circle was traced on the second screen with a hole punctured at the center. The second screen was then shifted until the light emanating through its centered hole aligned with the center of the first screen. The centers of the two screens defined the optical axis.

The aperture with the plate were then placed in the machined well (about 36 mm above the acrylic viewport) and shifted until the LED light emanating through the aperture was centered with the circle on the second screen. Once the aperture was aligned, the bolts holding the aperture and plate were tightened, the LED was removed, and the system was reassembled.

The system was then pumped down to a base pressure of a few millitorr. A mass spectrum was taken using the RGA to ensure water and hydrocarbons were low. Argon was used for leak checking. After leak checking, the turbomolecular pump connected to the upper chamber was turned off and allowed to slow down for 5 minutes before opening the helium line.

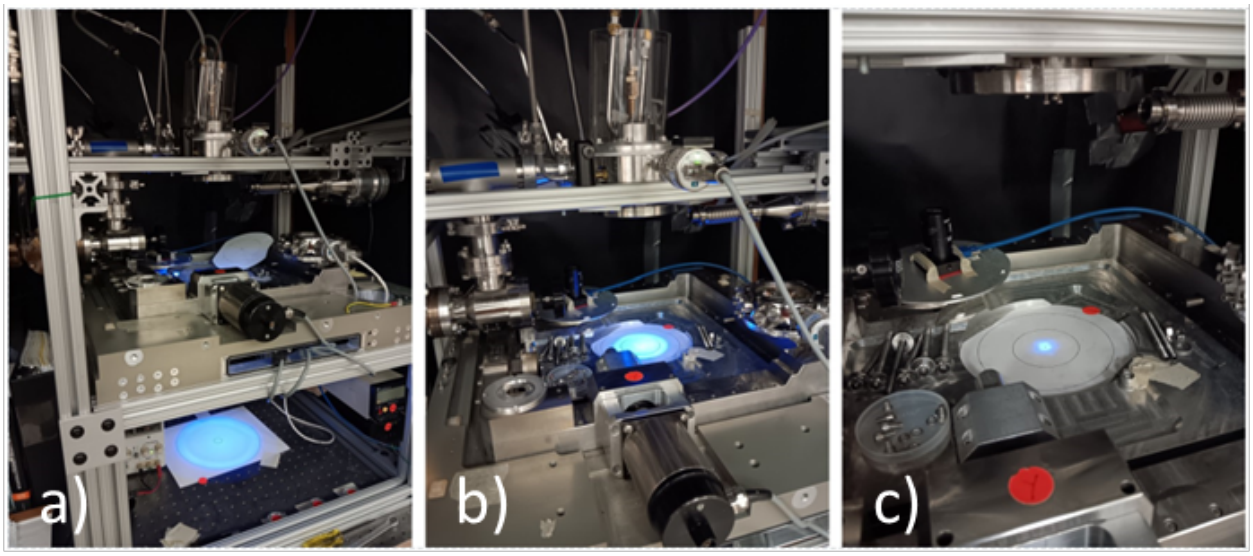

Figure 2.3 Photographs of the alignment procedure. a) The first screen is centered on the light illuminating from the bore. b) The second screen is centered using a XY stage. c) An aperture is mounted in the machined well of the anode and centered.

The helium pressure was controlled using a sapphire leak valve connected upstream from the cathode. The system was then purged with helium at 2.5 torr in the upper chamber for 1 hour.

After the helium purge, the plasma was ignited with the upper chamber at 2.5 torr. The sapphire leak valve and applied voltage were adjusted until the upper chamber pressure read 1 torr and the high voltage power supply read 1 A of current. The plasma conditions were fine-tuned for five minutes. The box was closed and a LabView program recorded forty data points of pressure from the upper chamber's and the lower chamber's micropirani gauges (twenty each) over the course of about five minutes. Meanwhile, ten images were taken by the ThorLab camera. After the five minutes, the pressure and current were adjusted to the next desired value, and the process was repeated. Four pressure and current combinations were run per trial, with the first and last being at 1 torr and 1 A to test repeatability.

After the last run, the plasma was extinguished, and a dark run was conducted to image the background signal. The sapphire leak valve was then closed and the turbomolecular pump connected

to the lower chamber turned off. After 30 minutes the roughing lines were closed and the roughing pump was turned off.

The ten images of the dark run were averaged. The ten images of each run were averaged and the averaged dark run image subtracted to give a final image.

2.4 Results and Discussion

An example of a final image of the phosphor screen fluorescing from the plasma's emitted VUV light is shown in Fig 2.4. Table 2.1 lists the trials conducted in the VUV range. The current and pressure of the plasma (the upper chamber's pressure, P_H) are reported, as well as the pressure of the lower chamber (P_L) and the peak intensity of the distribution. Note that the intensities listed are values observed by the CCD camera from the phosphor screen fluorescing, not values of VUV light emitted by the plasma.

Note in Fig 2.4 that the width of the observed distribution is in the range of 15 mm. Considering the system forms a simple pinhole camera where the image is the object smeared by the aperture, the wide image implies that the VUV intensity distribution of the plasma is wider than the cathode bore (7.5 mm diameter). Therefore there must be significant VUV emission at the end of the cathode and outside the bore.

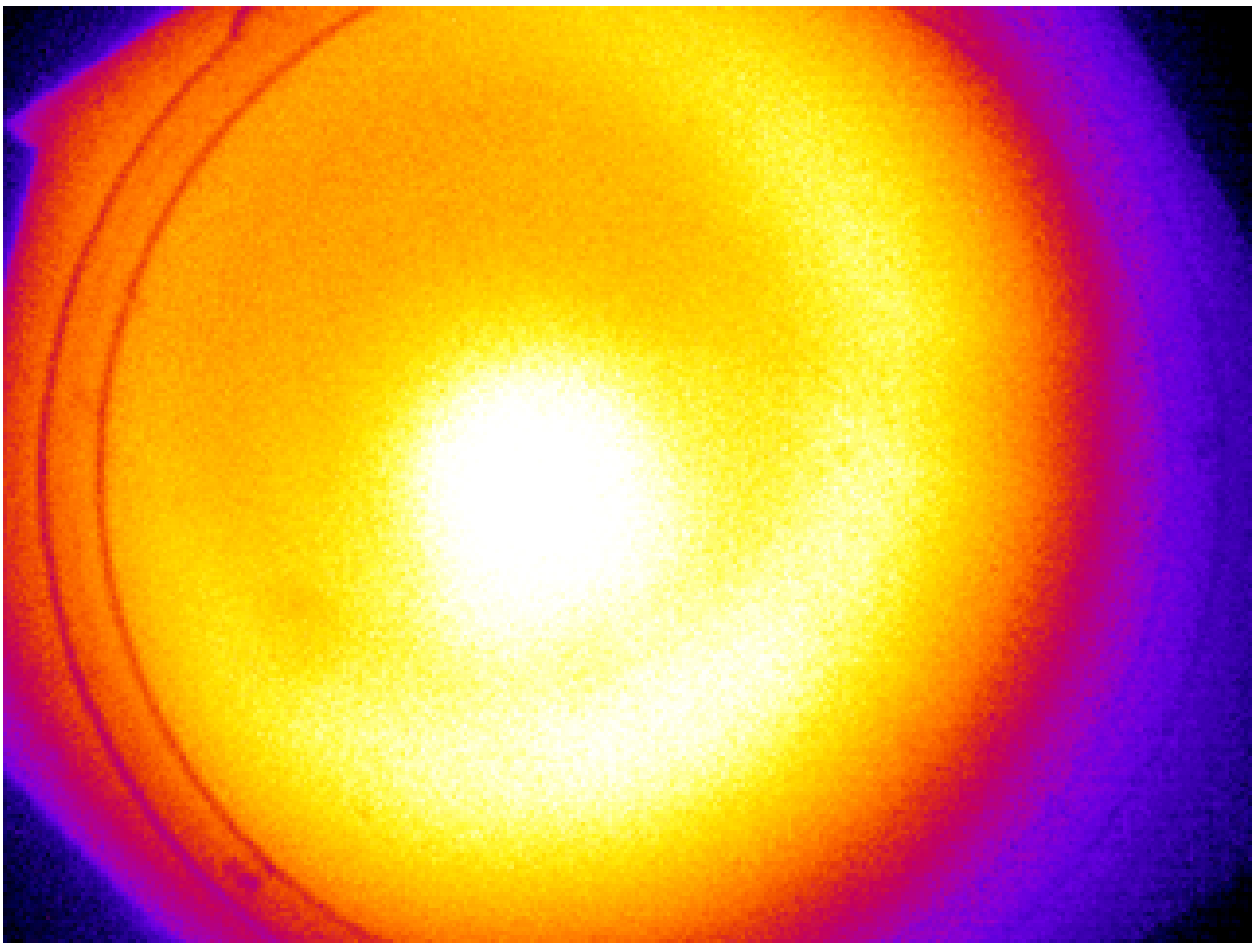

Figure 2.4 Image of the VUV intensity distribution on the viewing screen from a 1.00 A, 1.03 torr plasma (Trial 3, Run 4). The two dark rings are the sides of a 15 mm diameter groove machined into the viewport. Note that it appears that the distribution appears to be a central spot with a ring on the scale of 10 mm in diameter. This implies that the source distribution is likewise a central spot with a ring. The central spot being off-centered implies that the aperture may not have been on the optical axis.

The VUV light distribution was modelled as a centered bright spot with a ring, both two dimensional and located at the end of the cathode:

$$I_s(r_s) = A(De^{-Br_s^2} + (1-D)e^{-B(|r_s|-C)^2}) \tag{2.1}$$

in pixel value where $r_s = \sqrt{x_s^2 + y_s^2}$ is the location of interest (x_s, y_s) on the source plane in meters (the subscript "s" stands for the source plane) and A, B, C, and D are variables that describe the distribution: A is a scaling term (pixel value), B is related to the width of the centered bright spot and ring ($1/m^2$), C is the radius of the ring (m), and D is the relative brightness of the centered spot to the ring. To determine if these variables depended on the plasma's current and pressure, we calculated the anticipated intensity distribution on the viewing screen and compared it to the image. The intensity (I_p, the subscript "p" for the photo plane) in at a given point on the viewing screen (x_p, y_p in meters) is the sum of all the light coming from the intensity distribution at the end of the cathode that makes it through the aperture and arrives at the point of interest. Treating the intensity distribution as an array of infinitesimal point sources, the sum becomes an integral over the area of the aperture (indicated by subscript "a"):

$$I_p(x_p, y_p) = \int \frac{I_s(x_s, y_s)}{4\pi R^2} \delta A_a \tag{2.2}$$

. Setting the height of the observation plane at $z_p = 0$, the height of the aperture plane at z_a (m), and the height of the end of the cathode at z_s (m), we find that $x_s = x_a - (\frac{z_s}{z_a} - 1)(x_p - x_a)$ and $y_s = y_a - (\frac{z_s}{z_a} - 1)(y_p - y_a)$.

A Matlab program selected 961 points (31 by 31 grid within a roughly 10x10 mm area) from the image, calculated Eq 2.2 for each point, and calculated the Root Mean Square Error (RMSE) between the 961 image values and the calculated values. The RMSE can be interpreted as the average amount each point on the model's distribution is off from the image. To determine the variables B, C, and D, the image was normalized to the peak intensity value and the variables were varied until a minimal RMSE was found.

Table 2.1 Plasma distributions observed in the VUV with their plasma parameters, peak intensity observed, and RMSE between the distributions and the model.

Trial	Run	I (A)	P_H (torr)	P_L (torr)	A (pixel value)	B $1/m^2$	C m	D	Peak Intensity (pixel value)	RMSE (pixel value)
1	1	1.00	1.03	0.27	1123535	297370	0.005	0.86	27	1.07
	2	0.75	1.01	0.27	851779	340573	0.005	0.85	21	1.15
	3	0.50	1.00	0.27	602250	255100	0.005	0.85	15	0.56
	4	1.00	1.03	0.27	1123535	297370	0.005	0.86	27	0.96
2	1	1.00	1.03	0.27	1123535	297370	0.005	0.86	27	0.90
	2	1.00	0.75	0.15	970000	199188	0.005	0.75	29	1.18
	3	1.00	0.52	0.09	1369151	118538	0.006	0.66	39	2.12
	4	1.00	1.03	0.27	1123535	297370	0.005	0.86	28	1.33
3	1	1.00	1.04	0.27	1142005	300876	0.005	0.87	27	1.11
	2	0.76	0.76	0.16	780479	269275	0.005	0.75	21	1.37
	3	0.50	0.52	0.09	1078261	150028	0.006	0.66	24	2.37
	4	1.00	1.03	0.27	1123535	297370	0.005	0.86	27	0.93

When the values that provided minimal RMSE were found for each Run, they were plotted against the Run's current (I in A) and pressure (P in torr) and a function was fitted to the values. To determine the variable A, the procedure was repeated with the images not normalized and the fitted values of B, C, and D. The functions are listed below with their final RMSE listed in Table 2.1. The Runs with the lowest and highest RMSE with respect to the peak intensity are given in Fig 2.5. Discrepancies between the model and the data may be due to VUV absorption of the helium gas, aperture misalignment, and carbon buildup on the phosphor screen.

$$\begin{aligned} A &= (38.27 + 1.91I - 81.74P + 7.515IP + 44.78P^2) * 10^5 \\ B &= (-3.978 + 14.02I + 0.8715P - 10.68I^2 + 2.635IP) * 10^5 \\ C &= (7.759 - 6.347I + 0.3495P + 5.908I^2 - 2.838IP) * 10^{-3} \\ D &= 0.4467 + 0.4036P \end{aligned} \tag{2.3}$$

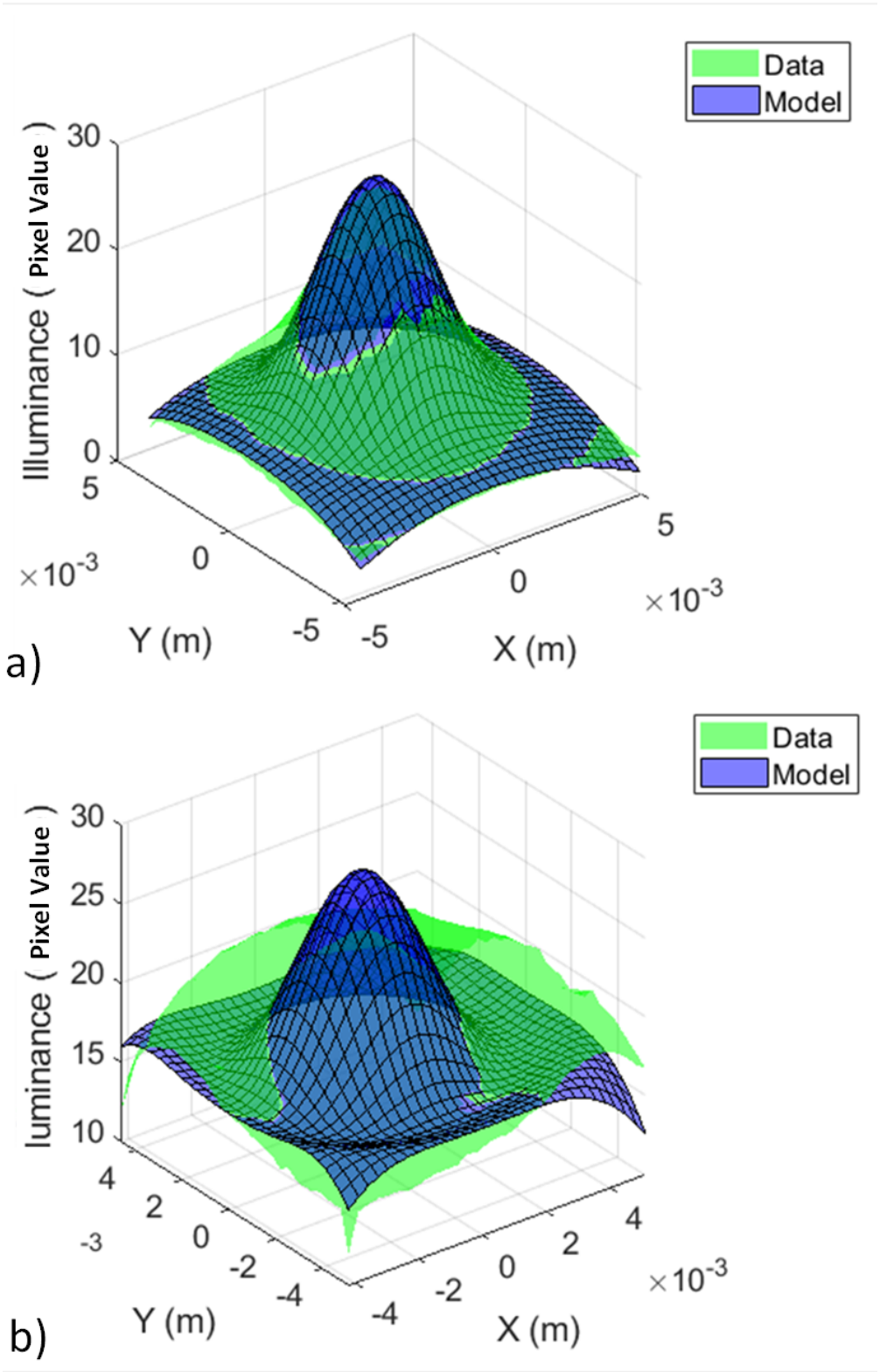

Figure 2.5 a) Lowest RMSE value for VUV (Trial 2, Run 1, 3.35% of peak intensity value). b) Highest RMSE value for VUV (Trial 3, Run 3, 9.86%).

Within the observed current and pressure range (1 A, 1 torr to 0.5 A, 0.5 torr), B varies from from a minimum of 738525 $1/m^2$ to a maximum of 2658350. This gives the center peak and ring widths of about 1.16 mm to 0.6 mm. C (the radius of the ring) varies from 4.5 mm to 6.1 mm, meaning that the Gaussian ring remains mostly outside the bore of the cathode (radius about 3.75 mm) while the center peak remains completely within the bore. This implies that there are two main regions of VUV emission: a center peak within the bore and a ring near the bore's end.

The behavior of these regions may be related to the electron concentration in the plasma. In hollow cathodes, electrons emitted from the cathode surface within the bore oscillate back and forth as they make their way towards the end of the cathode. This phenomenon, known as the pendulum effect, creates a high concentration of primary and secondary electrons (10). These electrons ignite and sustain the plasma, as well as excite neutral helium atoms. VUV is emitted when the excited neutral helium atoms transition to the ground state (16). Regions of higher VUV intensity therefore must have higher electron concentration. The electron concentration of a helium plasma was investigated by Bernatskiy et al. The cathode they investigated was a rectangular open box with a 100x10 mm opening. They measured the electron concentration of the plasma at various points from the cathode to the anode to build a three dimensional map of the concentration. They found that along the 10 mm direction (which is comparable to our 7.5 mm diameter cylindrical cathode), the electron concentration had a peak at the center near the cathode that decreased as one moved closer to the anode. They also found that the electron concentration was low near the edges of the cathode, but that it increased to a maximum a few millimeters towards the anode, then decreased again. This creates two regions: a center peak near the cathode opening due to exiting electrons and an outer region beyond the cathode due to electrons diffusing out (18). These regions match well to the center peak region and the outer ring of our VUV intensity distribution model.

Fig 2.6 shows how the parameters describing the VUV intensity distribution change with current and pressure. With constant pressure and increasing current, A (the overall intensity) increases,

B increases (widths decrease), *C* changes minimally (radius of the ring is unchanged), and *D* is unaffected (center spot and ring stay proportional). The increased brightness may be due to the current increasing the electron concentration and therefore also the number of excited helium atoms that emit VUV. Higher currents require higher electric fields, which would cause the electrons oscillating in the electric fields to be more confined, causing the VUV emission region to be more narrow. Many of the electrons exiting the bore where the center peak region is located will diffuse to the ring region, meaning the center peak and ring regions will stay proportionally the same.

With constant current and increasing pressure, *A* decreases to a minimum in the range of 0.8-0.9 torr before again increasing (overall intensity decreases, then slightly increases), *B* increases (widths decrease), *C* decreases (ring becomes smaller), and *D* increases (the center spot becomes proportionally brighter). The minimum in brightness may be due to the competing effects of electron energy and population. At lower pressures, the electrons have a larger mean free path. This means that a lower electric field is needed to accelerate the electrons to an energy where they can excite helium atoms and cause VUV emission. This would cause the regions to be wider than at higher pressures. However, the larger mean free path also means that there are fewer electron-atom collisions within the regions. As the pressure increases, the size of the regions shrink, causing a decrease in intensity. At higher pressures, the regions continue to shrink, but the number of electron-atom collisions within the regions increases drastically. The increase of collisions causes the overall intensity to increase.

Fig 2.7 shows the power emitted from the center spot and the outer ring. Values were calculated by integrating Eq 2.1 over the hollow cathode bore for the center spot and over all space excluding the bore for the outer ring with constant current and pressure. Note that for all pressures and currents considered, the outer ring emits significantly more VUV light than the center spot. Though the amplitude of the center spot is much higher than the ring, it is distributed over a much smaller area. Thus, the total VUV light generated in the center peak is much less than that of the ring.

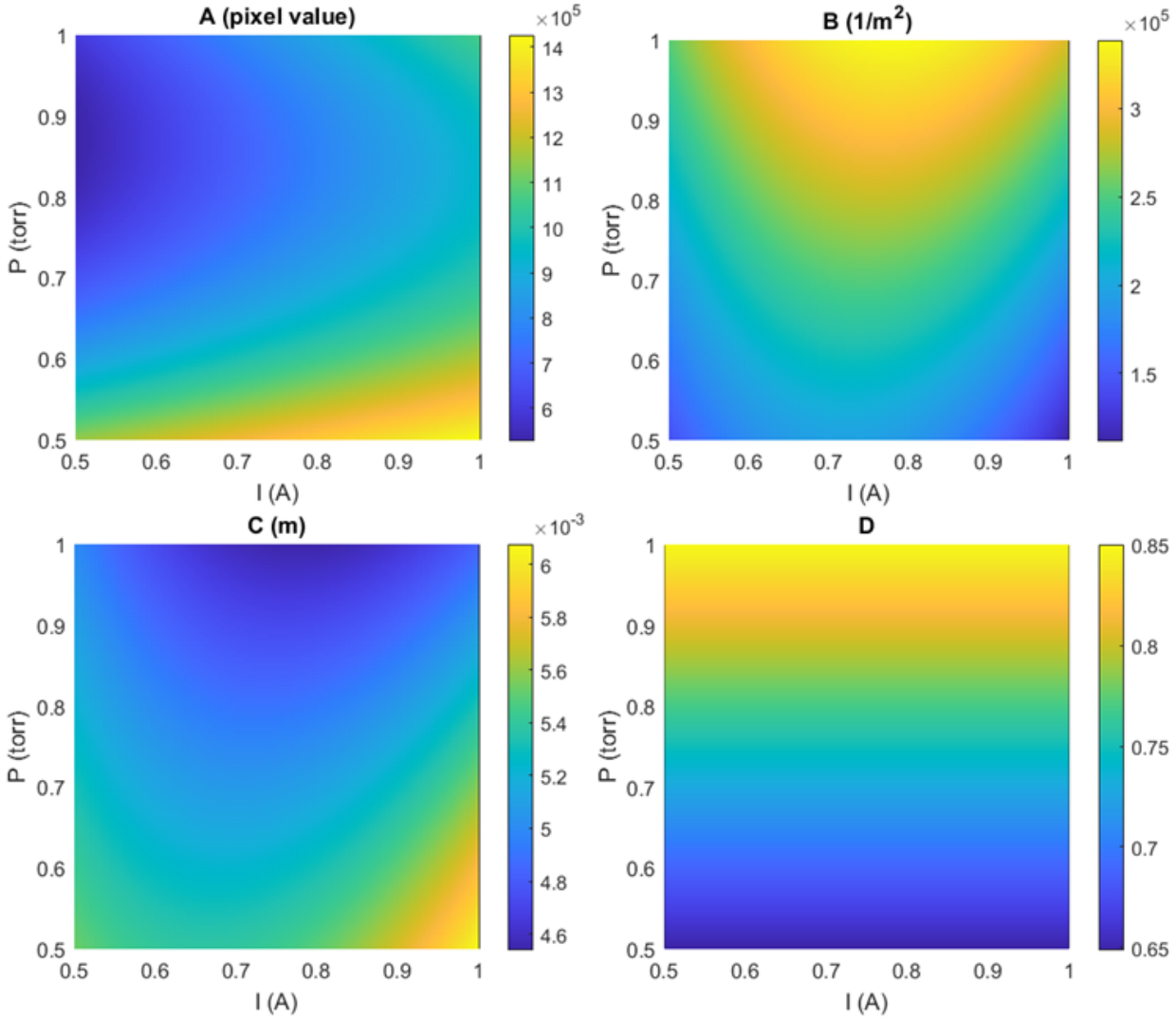

Figure 2.6 Parameters describing a hollow cathode helium plasma intensity distribution in the VUV range (58.4 nm) as functions of current and pressure. *A* is the total intensity (pixel value), *B* measures the width of the spot and ring features (large number is a small width, $1/m^2$), *C* is the radius of the ring (m), and *D* the relative brightness of the spot vs ring (peak intensity comparison).

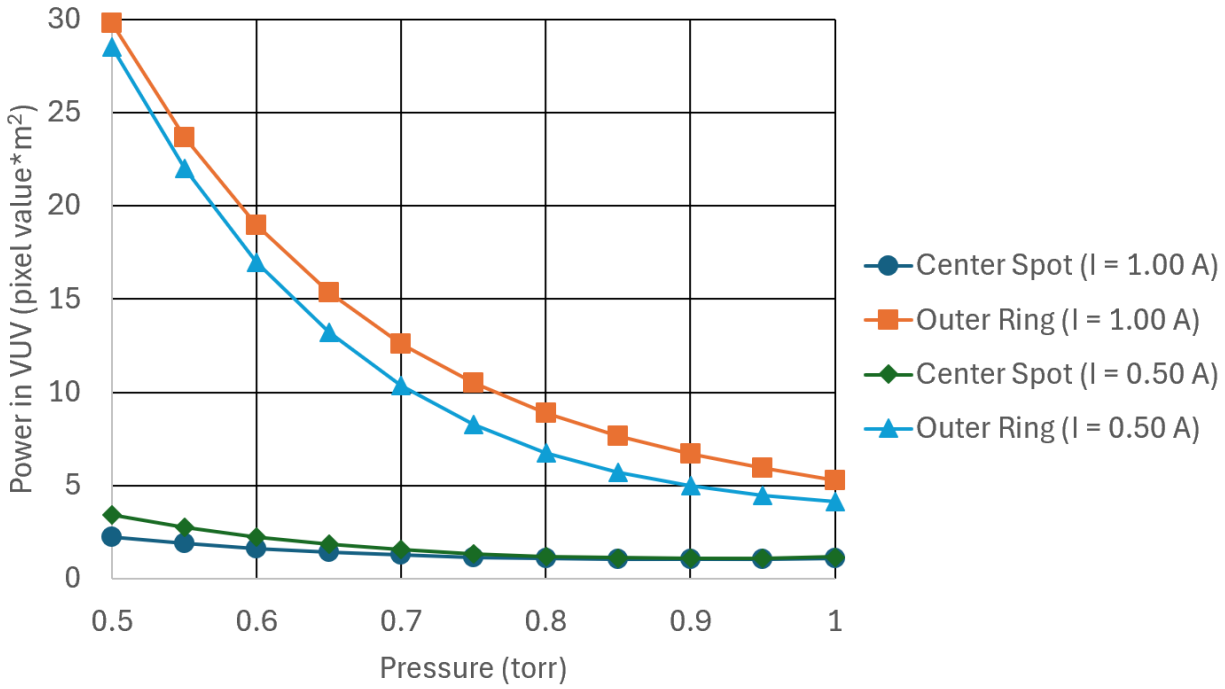

Figure 2.7 The VUV light emission power of the center spot and outer ring for various current and pressure values. Note that for all current and pressure values considered, the outer ring emits more VUV light than the center spot.

The outer ring emits more VUV light at higher currents and lower pressures. The center spot emission also decreases with increased pressure but in contrast to the ring, it decreases with increased current. Though the amplitude of the center spot increases with current, it also becomes narrower. The decrease in distribution area causes the total VUV light generated in the center spot to decrease with increasing current.

2.5 Conclusion

We have imaged the VUV light distribution from the hollow cathode helium plasma source, projected through an aperture to a phosphor screen. These images were used to build an empirical model of the VUV light distribution of the plasma as a function of current and pressure. The model predicts

the observed distribution within 9.86% RMSE (normalized to peak) or less within the current and pressure ranges of 0.50-1.00 A and 0.50-1.00 torr. The model describes the intensity distribution as a center peak within the bore of the cathode and a ring at the end of the cathode. The model also states that while the center peak amplitude is somewhat higher than the amplitude of the ring, the larger area of the ring means that the majority of the VUV light emitted is from the ring. For VUV spectroscopy involving a McPherson 629 model hollow cathode helium plasma, more VUV output can be achieved by utilizing the ring rather than the center spot.

2.6 Conflicts of Interest

The authors state that there is no conflicts of interest.

2.7 Acknowledgments

We wish to acknowledge the support of Brigham Young University (BYU), the NASA Space Grant Consortium (#NNX15AI24H), BYU Graduate Studies HIDRA Fellowship, (BYU) College of Physical and Mathematical Sciences, John Ellsworth, and Jeremy Peterson (BYU Physics Machine Shop).

Data Availability Statement

The data that support the findings of this study are available from the corresponding author upon reasonable request.

2.8 References

Bibliography

[1] S. Zhao, M. Djavid, and Z. Mi. Surface emitting, high efficiency near-vacuum ultraviolet light source with aluminum nitride nanowires monolithically grown on silicon. *Nano Lett.*, 15:7006–7009, 2015.

[2] M. Kaku, D. Kai, M. Katto, A. Yokotani, S. Kubodera, and W. Sasaki. Surface analysis by photo-stimulated desorption using tunable VUV radiation. *Appl. Phys. B*, 119:427–433, 2015.

[3] A. Lelevic, V. Souchon, M. Moreaud, C. Lorentz, and C. Geantet. Gas chromatography vacuum ultraviolet spectroscopy: A review. *J. Sep. Sci.*, 43:150–173, 2019.

[4] W. Zheng, J.Lemin, and F. Huang. Vacuum-ultraviolet photon detections. *iScience*, 23, 2020.

[5] F. Roberts and S. Anderson. Note: Hollow cathode lamp with integral, high optical efficiency isolation valve: A modular vacuum ultraviolet source. *Rev. Sci. Instrum.*, 84(126101), 2013.

[6] D. Han and S. Moon. Development of vacuum ultraviolet emission source using a cone-shaped O_2 / He hollow cathode discharge. *J. NanoSci. Nanotechno.*, 17(11), 2017.

[7] J. Stephens, A. Fierro, B. Walls, J. Dickens, and A. Neuber. Nanosecond, repetitively pulsed microdischarge vacuum ultraviolet source. *Appl. Phys. Lett.*, 104(7), 2014.

[8] Y. Wan, Z. Liu, J. Yao, B. Xu, J. Chen, F. Zhang, Z. Zhang, L. Qiao, and Y. Cheng. A spectrally bright wavelength-switchable vacuum ultraviolet source driven by quantum coherence in strong-field-ionized molecules. *New J. Phys.*, 23, 2021.

[9] M.E. Pillow. A critical review of spectral and related physical properties of the hollow cathode discharge. *Spectrochim. Acta*, 36(B):821–843, 1981.

[10] Wikipedia contributors. Hollow cathode effect — Wikipedia, the free encyclopedia, 2022. [Online; accessed 3-June-2024].

[11] G.H. Freeman and W. H. King. Vacuum ultraviolet wavelength comparison of two copper sources using an imaging system. *J. Phys. E: Sci. Instrum.*, 12(282), 1979.

[12] R. Mavrodineanu. Hollow cathode discharges. *J. Res. Natl. Bur. Stand.*, 89(2):143–185, 1984.

[13] A. Gilmutdinov, B. Radzuik, M. Sperling, B. Welz, and K. Nagulin. Spatial distribution of radiant intensity from primary sources for atomic absorption spectrometry. Part I: Hollow Cathode Lamps. *Appl. Spectrosc.*, 49(4):413–424, 1995.

[14] S. Paresce and C. Bowyer. Continuous discharge line source for the extreme ultraviolet. *Appl. Optics*, 10(8), 1971.

[15] F. Paresce, S. Kumar, and C. Bowyer. Continuous discharge line source for the extreme ultraviolet. *Appl. Optics*, 10(8):1904, 1971.

[16] A. Kramida, Y. Ralchenko, J. Reader and NIST ASD Team. NIST Atomic Spectra Database (ver. 5.11), [Online]. Available: `https://physics.nist.gov/asd` [2024, February 14]. National Institute of Standards and Technology, Gaithersburg, MD., 2023.

[17] Phosphor screens. Technical report, Proxivision.

[18] A. Bernatskiy, I. Draganov, N. Dyatko, L. Kochetov, and V. Ochkin. Spatial distribution of electron concentration in a dc glow discharge supported by a hollow cathode. *Plasma Chem. Plasma P.*, 44:651–666, 2024.

[19] R. Bartlow and S. Griffin. Axial evolution of the negative glow in a hollow cathode discharge. *Anal. Chem.*, 64:2751–2757, 1992.

Chapter 3

Carbon nanotube collimator as an vacuum ultraviolet window

3.1 Abstract

(A version of this chapter has been accepted into JVST B) Windows for vacuum ultraviolet (VUV) sources are valuable for many applications but difficult to fabricate due to most materials being too absorptive at VUV wavelengths. We have designed, fabricated, and characterized a carbon nanotube (CNT) collimator as a window with high (VUV) transmission and significant differential pumping. The CNT collimators are arrays of square channels of various dimensions and height with side walls composed of vertically aligned CNT forests. The CNT collimators in this work exhibited peak intensity transmissions for VUV light (58.4 nm) of 18% to 37% of that reported for the same system without a collimator present(1). Further analysis found that the peak intensity transmissions were lowered due to carbon deposition on the phosphor viewing screen from contaminants. The CNT collimator also had significant sidewall reflection in the VUV range ($\mathbf{R = 0.21 \pm 0.08}$ in the VUV range for angles 15.6 degrees and below). Pressure ratios (low pressure over high pressure) in the

VUV transmission experiment were dominated by leaks in the alignment mechanism. Additional experiments demonstrated the CNT collimator's reflection and superior differential pumping with pressure ratios less than 0.001.

3.2 Introduction

The vacuum ultraviolet (VUV) range of the electromagnetic spectrum can be used in various sample characterization methods, such as photo-ionization and photoelectron spectroscopy (2). However, VUV is strongly absorbed by all materials, including air. This often requires the VUV source and the sample of interest to be in different chambers with a windowless transition between them (3).

Several attempts have been made to create these windowless transitions. Giuliani et al reports how others have designed a series of vacuum chambers pumped at different rates in order transmit soft xrays from a beamline into a helium atmosphere(3). Preston et al designed a more compact differential pumping unit composed of several small concentric orifices (4). Nishizawa et al. used four chambers with relatively large apertures between them so as not to compromise the detection solid angle (5). Filho et al. considered small capillaries with aspect ratios (diameter over length) ranging from 0.02 to 0.05 (6). In all these designs, the windowless transitions required multiple components with individual pumping systems.

In this work, we describe a carbon nanotube (CNT) collimator we have designed, fabricated, and characterized to act as a window that allows VUV transmission while restricting gas flow. Fig 3.1 provides SEM images of the CNT collimators used in this study. The collimator design is an array of open square channels with high aspect ratios (height of collimator over width of channel, ranging from about 14.3 to 33.3 for the collimators considered) and thin side walls composed for vertically aligned CNT forests infiltrated with amorphous carbon. The open area of channels allows VUV light through, while the high aspect ratio makes gas flow difficult. The square shape of the

channels simplifies modelling light transmission and conductance. We also chose CNTs to fabricate the collimator due to their simple fabrication process, their ability to create structures with high aspect ratios, and the mechanical properties of their filler material (7). Amorphous carbon was chosen as the filler material because it is a simple change to the CNT growth conditions, it infiltrates well into the CNT matrix, and it improves the CNT collimator's rigidity. Infiltration does increase light reflection from the surface and decrease the absorption by the material (8).

This CNT collimator design was previously demonstrated to allow visible light transmission (9). In that work, the transmission through the CNT collimator was found to be described well using a geometric model. Discrepancies between the model and data were due to diffraction and double-wall reflections. Diffraction caused the transmission as a function of tilt angle to broaden, while the double-wall reflections caused small peaks of transmission at tilt angles beyond the cut-off angles. In this work, we demonstrate the CNT collimator's transmission for VUV light (58.4 nm) and its restriction of gas flow. Our light source was a hollow cathode helium plasma run at pressures of about 1 torr and less and currents of about 1 A and less. For the CNT collimators considered, we observed peak intensity transmissions of 18% to 37%(1). We also found that single-wall and double-wall reflections significantly affected the VUV transmission. Pressure ratios in the light transmission experiments are dominated by leaks in the alignment mechanism but in specific differential pumping experiments are as low as 0.001.

3.3 Methods

The fabrication of the CNT collimators is outlined next. The Experiment section which follows outlines the experiment layout, procedure of installing a CNT collimator into the system, and the procedure for testing the CNT collimator.

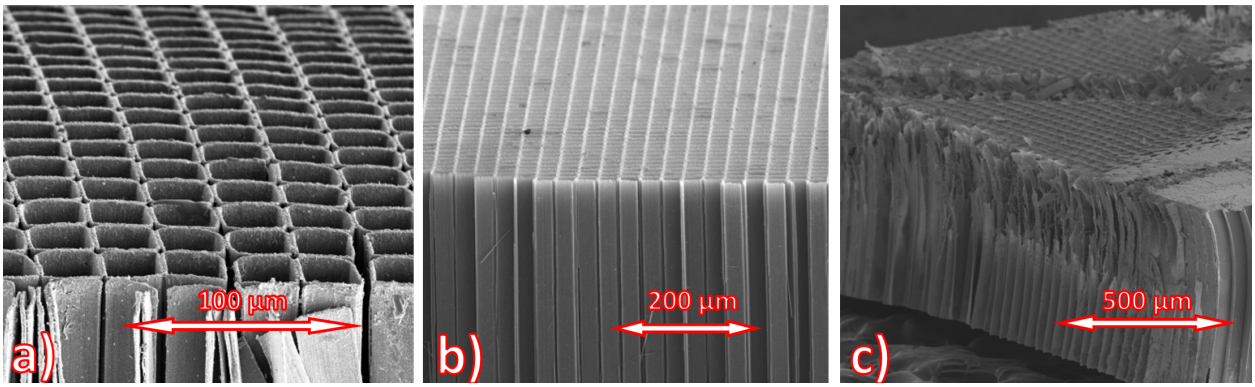

Figure 3.1 SEM images of the three different CNT collimators considered. Note that the portions imaged were removed from the edges of the collimators and therefore are not the portions that were over the aperture. Damage seen was caused by removing the portions and placing them on SEM stubs. a) collimator A with channel width 25 μm, height 750 μm, and aperture diameter 2.2 mm. b) collimator B with channel width 25 μm, height 500 μm, and aperture diameter 2.1 mm. c) collimator C with channel width 50 μm, height 760 μm, and aperture diameter 2.2 mm.

3.3.1 Fabrication

The fabrication followed closely to that given by Westover et al(9). Substrate preparation started with sputtering 70 nm of alumina onto a n-doped Si (100) wafer. Hexamethyldisilazane (HMDS) and photoresist AZ3330 were spin coated onto the wafer using a Laurell spinner (model number WS-400A-6NPP-LITE) at 6000 rpm for 60 seconds. After a one-minute bake at 90°C, the collimator pattern was photolithographed onto the wafer using a Karl Suss Aligner (MA 150 CC). The wafer was then developed in an alkaline solution. Four nm of iron was deposited using a thermal evaporator. The wafer was then diced into individual die, sonicated in N-methyl-2-pyrrolidone (NMP) for 20 minutes, and dried with a nitrogen gun. The end result was a Si die coated with alumina and a patterned Fe film.

The patterned vertically aligned CNT forests were grown in a 1-inch diameter quartz tube furnace (Lindberg/Blue, model number TF55030COMA-1) at 750°C with 311 sccm of hydrogen and 338 sccm of ethylene for 30 minutes. Carbon infiltration was done at 900°C with 311 sccm

of hydrogen and 338 sccm of ethylene for four to five minutes. The infiltration filled the walls of the CNT collimator with carbon which made the collimator more rigid, but also deposited a floor layer over the whole sample. Once removed from the furnace, the collimator was put into a heated (65°C) 45% by weight potassium hydroxide bath for several hours until the die separated from the collimator. The collimator was then placed in a water bath for several hours, then rinsed with isopropyl alcohol (IPA). When dried, it was plasma etched (Technics Planar Etch 2) with oxygen at about 100 mtorr and 200 W for two to five minutes. The plasma etch removed the floor layer that covered the bottom of the open channels. The CNT collimator was then mounted using carbon tape onto a shim-stock diaphragm (about 0.3 mm thick) with an aperture about two mm in diameter.

3.3.2 Experiment

The VUV light source was a hollow cathode plasma lamp. It is composed of an upper chamber and a lower chamber with a place for the CNT collimator to be mounted between them. The upper chamber has similar dimensions to a McPherson 629 model hollow-cathode light source. (The upper chamber – filled in with a gray-color– at the top of each figure in Fig, 3 is the hollow cathode drawn in cross section.) The outer wall contained the low-pressure gas and acted as an anode for the discharge. The cathode was connected to a high-voltage power supply (the black line to the right) and to a metered helium gas line that flowed down the bore of the cathode (along the optical axis). The upper chamber was connected to a turbomolecular pump, a roughing pump, a residual gas analyzer, and a MKS 925 MicroPirani® vacuum pressure gauge. The lower chamber was connected to a different turbomolecular pump, the roughing pump, and another micropirani gauge. At the bottom of the lower chamber a viewport with a P43 phosphor screen to convert VUV to visible light was mounted. Outside of vacuum and under the lower chamber was a camera with a laser line filter and a focusing lens to image the phosphor screen. The VUV light from the plasma was found to come from the inside of the bore and from the flat end of the bore as described elsewhere(1).

The setting up of the experiment followed very closely to that described elsewhere(1). After opening the system, cleaning the cathode of tarnish, and inserting an LED light into the bore of the cathode, two screens were inserted into the optical path and aligned with the optical axis (Fig 3.3, a and b and Fig 3.4, a and b). The shim stock diaphragm with the CNT collimator was then mounted to the base of the upper chamber using a mounting plate (Fig 3.2). The plate had wide bolt holes along the edge and threaded bolt holes near a center hole. The wide bolt holes along the edge allowed for aperture alignment while the threaded bolt holes allowed for tilting the CNT collimator for collimator alignment.

With the LED light illuminated, the diaphragm and plate were shifted until the transmitted light was centered on the screens (Fig 3.3, c and Fig 3.4, c). After removing the cathode source (shown in cross section) and LED light, a red laser pointer was suspended above the upper chamber and aligned with the optical axis (Fig 3.3, d). The laser light and CNT collimator created an interference pattern on the upper screen. If the collimator was tilted, the interference pattern was asymmetric (Fig 3.4, d). Using bolts in the threaded bolt holes of the plate, the collimator was tilted until the interference pattern became symmetric. The laser pointer was then removed and the system reassembled. The screens were removed and the camera with the line filter and focusing lens were placed back under the lower chamber.

The system was pumped down to a base pressure of a few millitorr for 30 min. A mass spectrum of the system was taken with the residual gas analyzer to check for contaminants. If contamination was low, the system was purged with helium for one hour at 2.5 torr. After the purge, the plasma was ignited. The pressure and current were then adjusted to the desired value for the run, 10 images of the phosphor screen were taken, and 20 pressure measurements from the upper and lower chambers were recorded over the course of about five minutes. The plasma was then extinguished, and 10 images additional images were taken for the background noise.

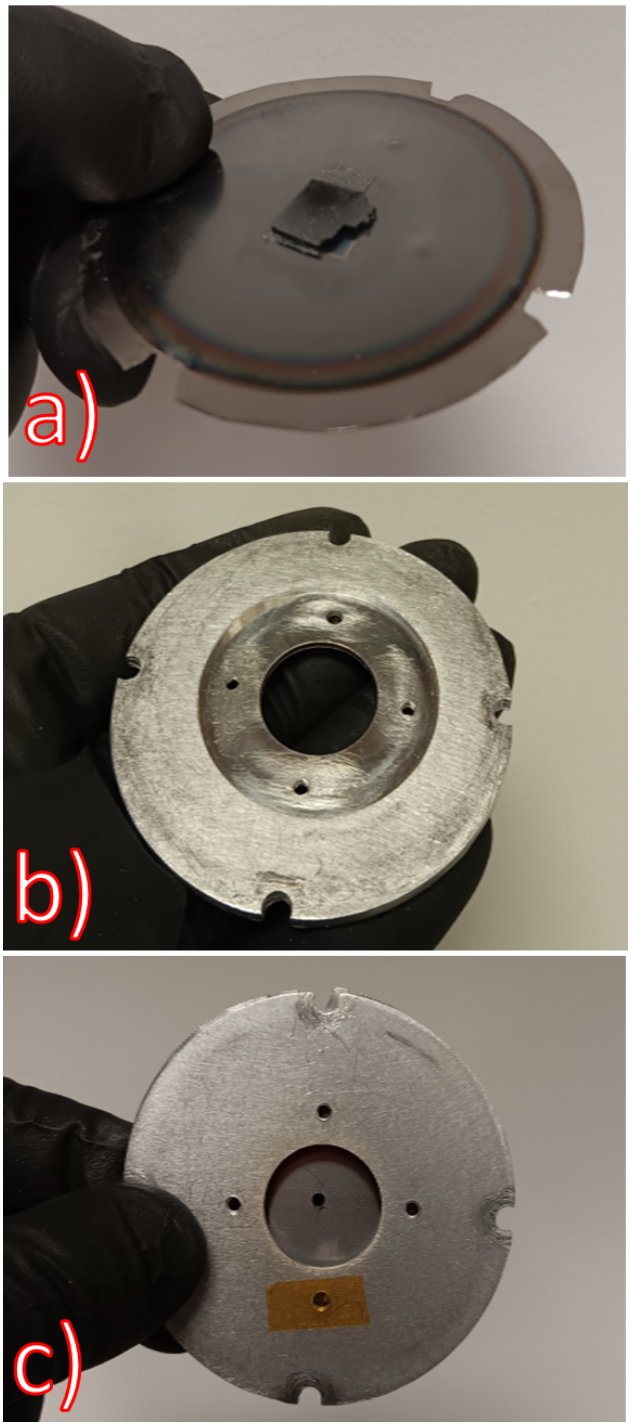

Figure 3.2 a) A shim-stock diaphragm with a CNT collimator mounted over the aperture via carbon tape. The CNT collimator was on the scale of 1 cm^2. The diaphragm was 6.75 cm in diameter. b) The mounting plate used to mount the diaphragm at the base of the upper chamber (also 6.75 cm in diameter). The wide bolt holes along the edge allowed for aperture alignment while the threaded bolt holes near the center allowed tilt of the CNT collimator. c) The diaphragm placed over the plate (opposing side to that shown in (b). The aperture over which the CNT collimator was placed can be seen in the center.

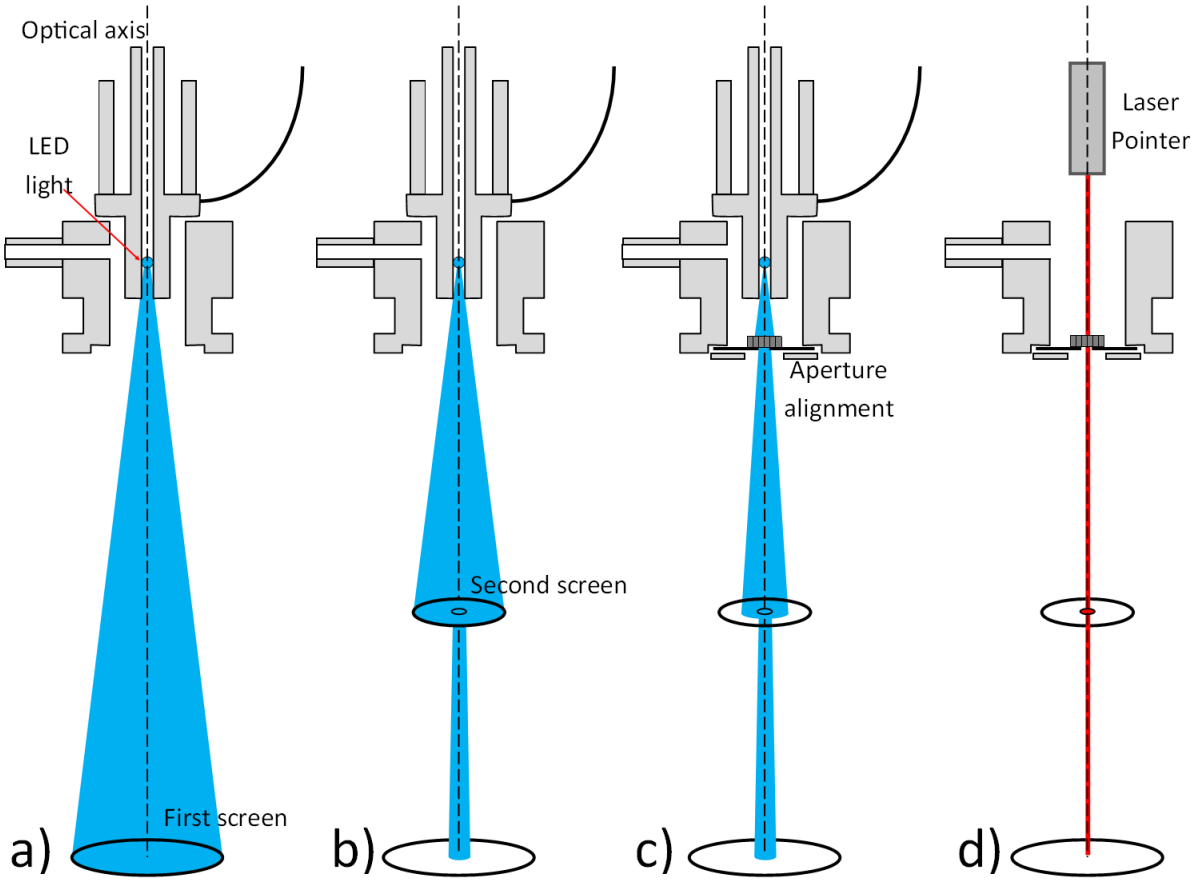

Figure 3.3 Diagram showing the alignment procedure of the shim-stock aperture and CNT collimator relative to the hollow cathode. a) A LED inserted into the hollow cathode bore illuminates the bore onto a screen. b) A second screen inserted into the path is aligned. The centers of the screens define the optical axis. c) The aperture is aligned by centering the emanating light onto the second screen. d) After removing the hollow cathode and aligning a laser to the optical axis, the CNT collimator is tilted till the interference pattern is symmetric.

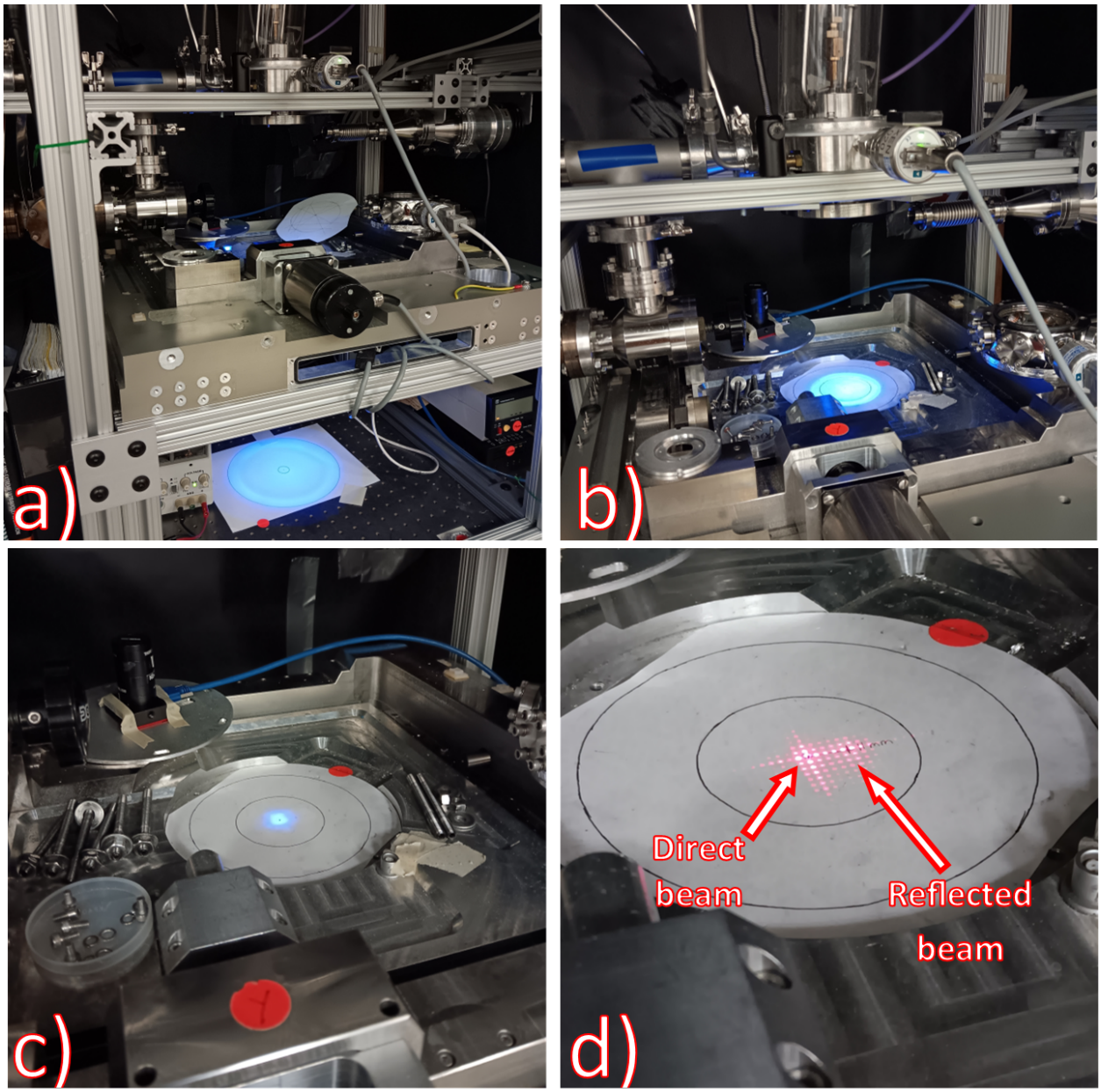

Figure 3.4 Photographs of the alignment procedure. a) The first screen is centered on the light illuminating from the bore. b) The second screen is centered using a XY stage. c) An aperture is mounted in the machined well of the anode and centered. d) After removing the hollow cathode and aligning the laser to the optical axis, misalignment of the CNT collimator can be seen in the interference pattern being asymmetric.

Variables	Collimator	A				B				C	
	Channel Width	25 microns				25 microns				50 microns	
	Height	750 microns				500 microns				760 microns	
	Aperture diameter	2.2 mm				2.1 mm				2.2 mm	
	Run	1	2	3	4	1	2	3	4	1	2
Observed	I (A)	1.00	0.91	0.81	1.00	1.00	0.91	0.90	1.01	1.00	1.00
	P_H (torr)	1.03	0.74	0.74	1.03	1.03	0.80	0.60	1.03	1.04	0.67
	P_L (torr)	0.013	0.008	0.008	0.013	0.016	0.011	0.008	0.015	0.038	0.022
	Peak Intensity (pixel value)	6.2	4.6	3.8	5.4	6.3	4.9	4.0	4.8	10.0	9.0
VUV	0th RMSE (pixel value)	0.94	0.82	0.66	0.97	1.40	1.13	1.80	1.66	2.24	2.23
Transmission	Optimal **R**	0.35	0.25	0.15	0.25	0.15	0.10	0.10	0.20	0.30	0.20
Modelling	**R** RMSE (pixel value)	0.19	0.20	0.11	0.22	0.28	0.20	0.11	0.17	0.54	0.53
Differential	Data/Model (no leak)	17.3	14.9	14.9	17.3	15.2	13.5	13.0	14.2	24.6	25.0
Pumping	Optimal Leak (L/s)	0.6	0.5	0.5	0.6	0.7	0.65	0.65	0.7	1.7	1.8
Modelling	Data/Model (leak)	1.0	1.0	1.0	1.0	1.0	1.0	1.0	1.0	1.0	1.0

Table 3.1 Runs conducted with CNT collimators A, B, and C. The first five rows list the dimensions of the CNT collimators considered, their aperture diameters, and the number of runs. The following four rows report the plasma's current in A and pressure in torr (P_H), the lower chamber's pressure in torr (P_L), and the peak intensity observed on the viewing screen in pixel value (0 to 1064). The next three rows report the results of the collimator's VUV transmission modelling as explained in the text. The bottom three rows report the results of modelling the collimator's differential pumping as explained in the text. Note that the model assuming no side wall reflection has significant discrepancies from the data (listed as "0th RMSE"). Including side wall reflection with a reflection coefficient of 0.10 to 0.30 lowers the discrepancies significantly. Note that the differential pumping model assuming no leaks also has large discrepancies. The discrepancies in this model can be minimized assuming a leak with conductance on order of 0.65 L/s.

3.4 Results and Discussion

Three CNT collimators, labelled A, B, and C, were mounted onto shim steel diaphragms and tested at various plasma pressures and currents. Their dimensions, along with the aperture diameter d, are listed in Table 3.1. Table 3.1 also lists the plasma current, plasma pressure (pressure in the upper chamber, P_H), peak intensity, and lower chamber pressure (P_L) of each run. When compared to the peak intensity observed on the viewing screen when a CNT collimator is not present(1), the VUV transmission of the CNT collimators varies from 18 to 37 %.

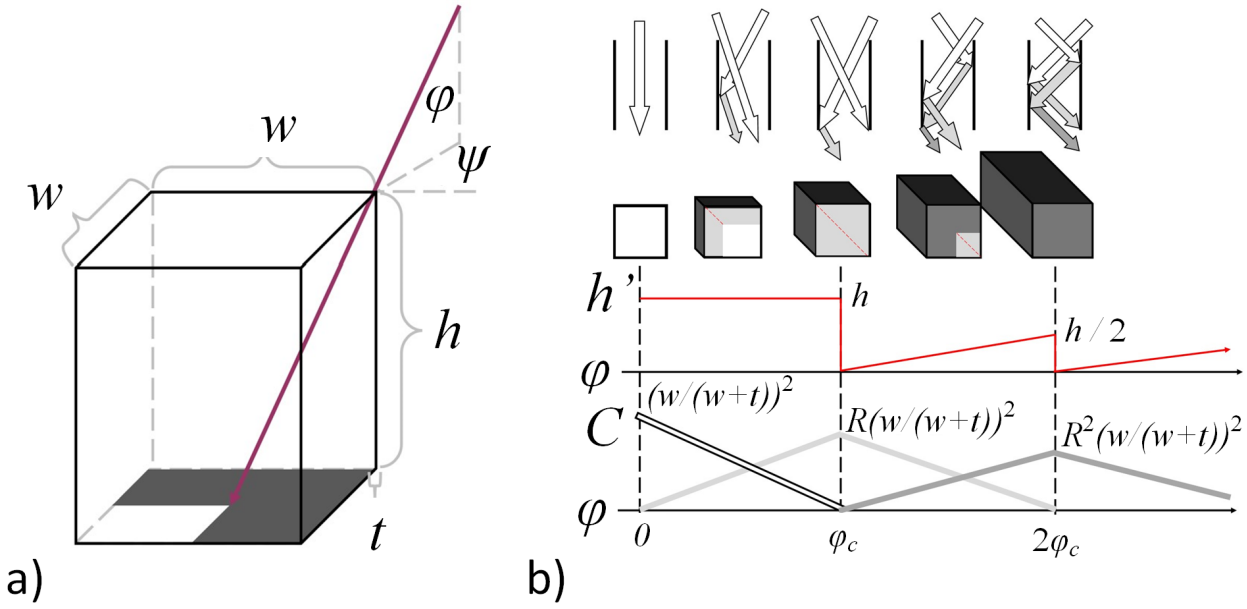

Figure 3.5 a) 0th-order model of the CNT collimator. ϕ is the polar angle of the incoming light and ψ is the azimuthal angle. Assuming the range of ϕ for a single channel is small, the loss in intensity is proportional to the loss in open area. b) Reflection model of the CNT collimator. We treat each reflection similar to the 0th-order model, but with an effective collimator height h' and a reflection factor $0 \leq \mathbf{R} \leq 1$.

3.4.1 Transmission

In our previous work, we observed the VUV emission (58.4 nm wavelength) from a hollow cathode helium plasma at various pressures and currents. We showed that the VUV intensity distribution of the plasma was nonuniform and changed significantly with the plasma parameters. We also developed an empirical model for describing the VUV intensity distribution as a function of pressure and current(1). Using this model, we can predict the CNT collimator VUV transmission. Fig 3.5, a shows our model of the light transmission through one channel of the CNT collimator when assuming that wall reflections are insignificant. We make these assumptions

- The x and y walls of the collimator are parallel to their respective axes in a Cartesian coordinate system.

- The walls are flat.
- The height of the collimator (h) over the aperture is constant.
- The dimensions of the collimator are significantly smaller than the dimensions of the overall experiment.
- The walls are completely absorptive in the 0-th order model.

These assumptions allow us to use a similar approach given by Westover et al. In that work, they developed a one dimensional geometric model for the collimator by relating intensity loss to the collimator's open area. As the collimator is tilted by an angle ϕ, the open area of the channels decrease, and therefore the amount of light that passes through the channels decreases. The angle at which there is no open area and therefore no light transmission is called the cut-off angle or collimating angle ϕ_c (9). In this work, we generalize the geometric model by introducing an azimuthal angle, ψ, and obtain:

$$C = \frac{(w - h\tan\phi\cos\psi)(w - h\tan\phi\sin\psi)}{(w+t)^2} \tag{3.1}$$

where w is the channel width, h is the channel height, t is the wall thickness, ϕ is the polar angle of the incoming light, and ψ is the azimuthal angle of the incoming light. To keep the equation from going negative at certain values of ψ, we take the absolute values of the trigonometric terms. We also need to consider the collimating angle ϕ_c, beyond which no light makes it through the channel. To make $C = 0$ beyond ϕ_c, we use Heaviside functions. We then pull out w and define $X = \frac{h}{w}|\tan\phi\cos\psi|$ and $Y = \frac{h}{w}|\tan\phi\sin\psi|$ to give:

$$C = \left(\frac{w}{w+t}\right)^2 (1-X)(1-Y)[\Theta(1-X)\Theta(1-Y)] \tag{3.2}$$

Note that in Westover et al, the light entering the CNT collimator was already collimated (9). Because the helium plasma is not a collimated source, we need to sum the light transmitted through

multiple channels of the collimator that arrive at a single point on the phosphor screen. We do this by integrating over the aperture with the Eq 3.2 as a weight function inside the integral given by(1):

$$I_p(x_p, y_p, 0) = \int \frac{CI_s(x_s, y_s, z_s)}{4\pi R^2} \delta A_a \tag{3.3}$$

where $I_p(x_p, y_p, 0)$ is the VUV intensity at a point of interest (x_p, y_p) on the phosphor screen, $I_s(x_s, y_s, z_s)$ is the VUV intensity of the plasma at (x_s, y_s, z_s) given by Olsen(1) with $x_s = x_a - (\frac{z_s}{z_a} - 1)(x_p - x_a)$ and $y_s = y_a - (\frac{z_s}{z_a} - 1)(y_p - y_a)$, (x_a, y_a, z_a) is the point on the aperture plane that light from (x_s, y_s, z_a) passes through and reaches $(x_p, y_p, 0)$, $R^2 = (x_p - x_s)^2 + (y_p - y_s)^2 + z_s^2$, $X = \frac{h}{w}|(x_p - x_a)/z_a|$, and $Y = \frac{h}{w}|(y_p - y_a)/z_a|$. A MatLab program selected 961 points (31 by 31 grid within a 10 by 10 mm area) from the image, calculated I_p for each point, and calculated the Root Mean Square Error (RMSE) between the predicted values and the observed values. The RMSE are listed in Table 3.1 under "0th RMSE".

Fig 3.6 shows the predicted distributions with the observed distributions for collimator A (Run 1 in Table 3.1). We note three discrepancies between the predicted and the observed. The observed has: 1) a lower peak intensity, 2) a "bench" feature around the peak, and 3) intensity observed beyond the collimating angle ϕ_c. These discrepancies were observed for all three CNT collimators. To explain VUV intensity beyond the collimating angle, we considered the effect of nonzero reflection off the side walls. Although VUV is readily absorbed in many materials, at grazing angles the reflection can be large (10).

To confirm side wall reflection, a third trial was conducted with CNT collimator C intentionally tilted and the resultant VUV distribution was observed (Fig 3.7). The distribution is clearly stretched out along the direction of tilt (lower right corner).

To model the side wall reflection, we consider the weight function at higher angles (Fig 3.5-b). Eq 3.2 gives the portion that experiences no reflection, and we therefore redefine it as the 0th order weight function C_0. At $\phi = 0$, $C_0 = (\frac{w}{w+t})^2$ and the portion that experiences one reflection, C_1, is equal to zero.

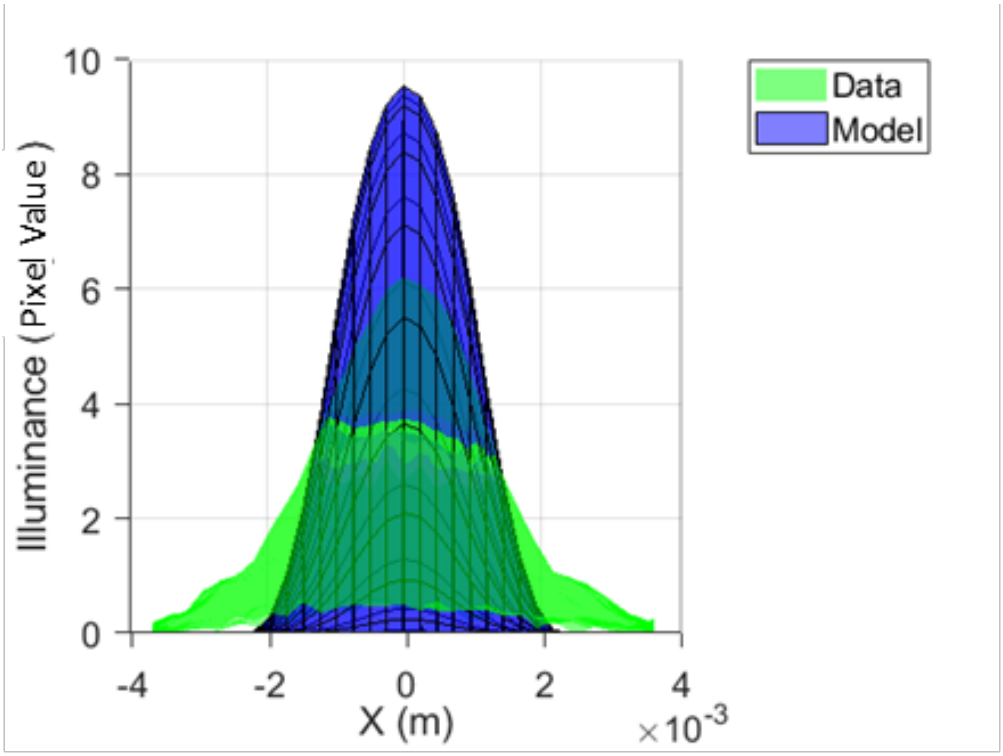

Figure 3.6 The observed (green) and predicted (blue) VUV distributions on the viewing screen from a $P = 1.03$ torr, $I = 1.00$ A plasma transmitted through CNT collimator A (Trial 1, Run 1) assuming no sidewall reflection ($\mathbf{R} = 0$). "X" is distance along the y axis on the viewing screen in millimeters. "Illuminance" is the fluorescing phosphor's intensity in pixel value. Note that the observed distribution has a lower peak intensity, has a "bench" feature, and is wider than the observed.

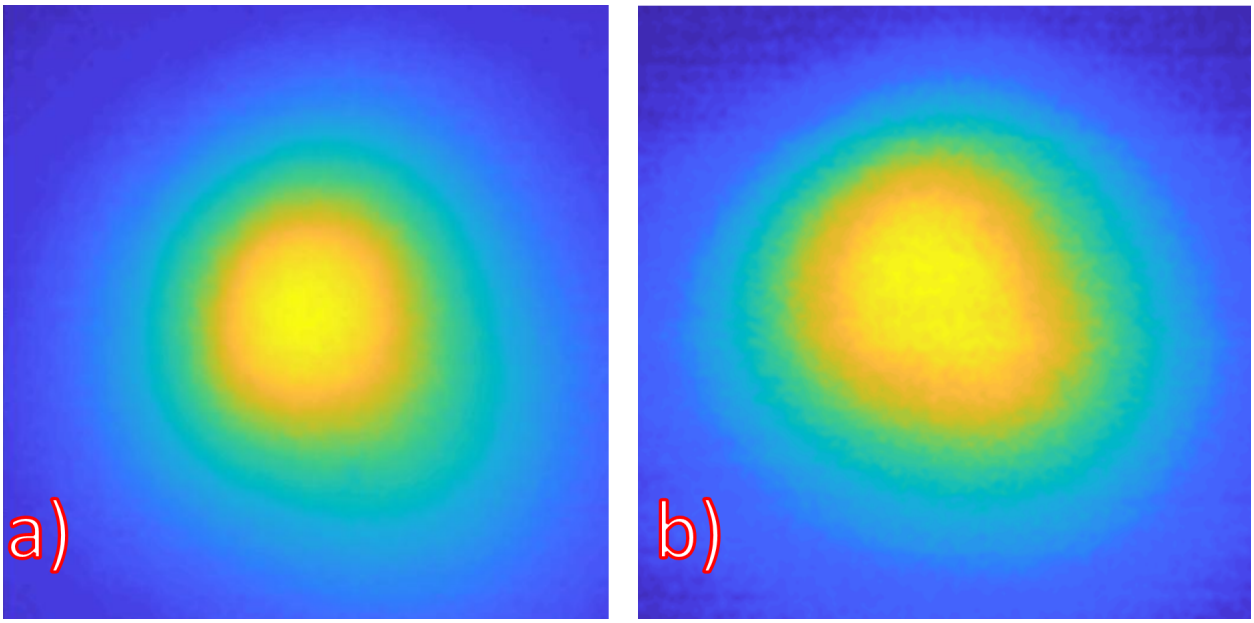

Figure 3.7 a) The observed VUV distribution for CNT collimator C with $P = 1.04$ torr and $I = 1.00$ A with the collimator aligned with the optical axis. b) The observed VUV distribution for CNT collimator C with $P = 1.04$ torr and $I = 1.00$ A with the collimator intentionally tilted. Note that the distribution is stretched in the direction of tilt (lower right corner).

As ϕ increases, C_0 follows Eq 3.2 while C_1 equals the remaining portion, $(\frac{w}{w+t})^2 XY\mathbf{R}$, where here $\mathbf{R}$ is the reflection coefficient. At the collimating angle ϕ_c, $C_0 = 0$ and $C_1 = (\frac{w}{w+t})^2$, which is equivalent to Eq 3.2 if $h = 0$. After the collimating angle, C_1 follows the same behavior as C_0 (and C_2 the same behavior as C_1) before the collimating angle. We can therefore use Eq 3.2 for the ith order reflection if we disregard the Heaviside functions and replace h with h':

$$
\begin{aligned}
w' &= \mathrm{Min}\left(\frac{w}{|\sin\psi|}, \frac{w}{|\cos\psi|}\right) \\
i &= \mathrm{Floor}\left(\frac{h|\tan\phi|}{w'}\right) \\
h' &= \begin{cases} h & \text{if } i = 0 \\ \left(\frac{h|\tan\phi|}{w'} - i\right)\left(\frac{h}{i+1}\right) & \text{otherwise} \end{cases} \\
X &= \frac{h'}{w}|\tan\phi\cos\psi| \\
Y &= \frac{h'}{w}|\tan\phi\sin\psi| \\
C_i &= \left(\frac{w}{w+t}\right)^2 (1-X)(1-Y)\mathbf{R}^i \\
C_{i+1} &= \left(\left(\frac{w}{w+t}\right)^2 \mathbf{R}^i - C_i\right)\mathbf{R}
\end{aligned}
\tag{3.4}
$$

Note that because the plasma distribution is nonuniform (1), the intensity that reflects off the x-axis parallel wall may be different than what reflects off the y-axis parallel wall. Therefore, when $i =$ odd, C_i needs to be split between C_{ix} and C_{iy}. How it is split depends on the azimuthal angle ψ:

$$
\begin{aligned}
C_{ix} &= \begin{cases} \left(\frac{w}{w+t}\right)^2 \left[(1-X)(1-Y) - \frac{(1-Y)^2}{2|\tan\psi|}\right] \mathbf{R}_x^{\frac{i+1}{2}} \mathbf{R}_y^{\frac{i-1}{2}} & \text{if } |\sin\psi| > |\cos\psi| \\ \left(\frac{w}{w+t}\right)^2 \left[\frac{(1-X)^2|\tan\psi|}{2}\right] \mathbf{R}_x^{\frac{i+1}{2}} \mathbf{R}_y^{\frac{i-1}{2}} & \text{otherwise} \end{cases} \\
C_{iy} &= \begin{cases} \left(\frac{w}{w+t}\right)^2 \left[\frac{(1-Y)^2}{2|\tan\psi|}\right] \mathbf{R}_x^{\frac{i-1}{2}} \mathbf{R}_y^{\frac{i+1}{2}} & \text{if } |\sin\psi| > |\cos\psi| \\ \left(\frac{w}{w+t}\right)^2 \left[(1-X)(1-Y) - \frac{(1-X)^2|\tan\psi|}{2}\right] \mathbf{R}_x^{\frac{i-1}{2}} \mathbf{R}_y^{\frac{i+1}{2}} & \text{otherwise} \end{cases}
\end{aligned}
\tag{3.5}
$$

where $\mathbf{R}_x$ and $\mathbf{R}_y$ are the reflection coefficients off the x-parallel and y-parallel walls, respectively.

When $i =$ even, then we have to split between $C_{(i+1)x}$ and $C_{(i+1)y}$:

$$\begin{aligned} C_{(i+1)x} &= \left(\frac{w}{w+t}\right)^2 \left[(1-X)Y + \frac{XY}{2}\right] \mathbf{R}_x^{\frac{i+1}{2}} \mathbf{R}_y^{\frac{i-1}{2}} \\ C_{(i+1)y} &= \left(\frac{w}{w+t}\right)^2 \left[(1-Y)X + \frac{XY}{2}\right] \mathbf{R}_x^{\frac{i-1}{2}} \mathbf{R}_y^{\frac{i+1}{2}} \end{aligned} \tag{3.6}$$

Now we consider the locations on the source plane that are reflected to the point of interest on the viewing plane. If the 0th order enters a column at an azimuthal angle ψ, then the 1st order-x reflection enters at $-\psi$, the 1st order-y reflection at $\pi - \psi$, and the 2nd order at ψ if $|\tan\psi| > 2$ or < 0.5, in which it reflects off two parallel walls, or at $\pi + \psi$, in which case it reflects off two perpendicular walls. Higher order reflections become more complicated to trace and may not be significant.

Reflection explains the intensity observed beyond the collimating angle ϕ_c, but it increases the discrepancy in the values near the peak of the distribution. If carbon was deposited on the phosphor screen during operation, it would absorb VUV light and affect the observed distribution. We used a Thermo Scientific K Alpha XPS system to measure the amount and location of carbon deposition on the phosphor screen. We found that there was carbon deposited throughout the observed area and a 1 mm wide approximately circular ring with an outer diameter of about 5 mm with 2-3 times more carbon deposition than the surrounding area (Fig 3.8). The carbon deposition across the screen may have caused the peak intensity discrepancy while the carbon ring may have caused the "bench" discrepancy. Because the deposited carbon reduces the intensity, we compared our model only to data that was outside the 5 mm ring. We assumed that $\mathbf{R}_x$ and $\mathbf{R}_y$ are equal and constant in this range of angles ($\mathbf{R}_x = \mathbf{R}_y = \mathbf{R}$) and varied $\mathbf{R}$ by units of 0.05 to find the minimum RMSE. Results are listed in Table 3.1 under "Optimal $\mathbf{R}$" and "$\mathbf{R}$ RMSE".

Fig 3.9 shows the predicted distribution with significant side wall reflection compared to the observed distribution for collimator A (Run 1 in Table 3.1). Note that the predicted fits well with the observed on the edges of the distribution, but the peak is much higher than observed.

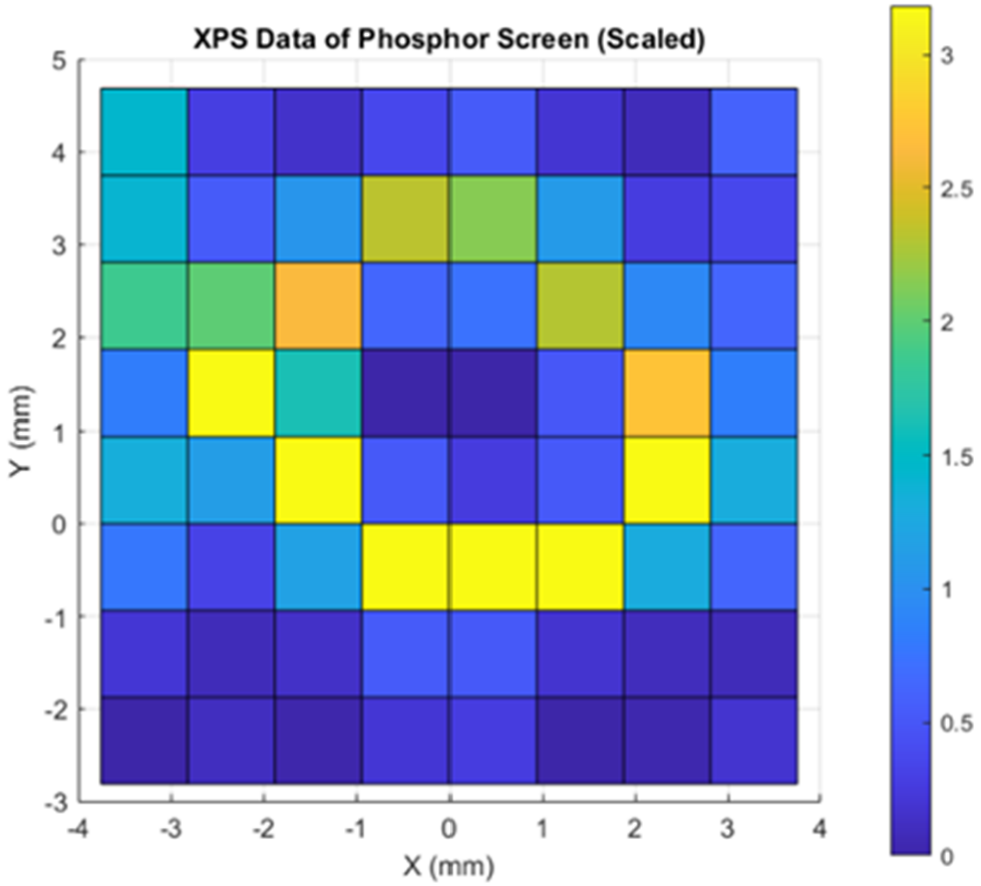

Figure 3.8 XPS data for carbon on the P43 screen. "X" is distance along the phosphor screen in the x direction in millimeters. "Y" is is distance along the phosphor screen in the y direction in millimeters. Color values are relative carbon concentration- a value of 3 means that there is three times more carbon deposition at that location than a location with a value of 1.

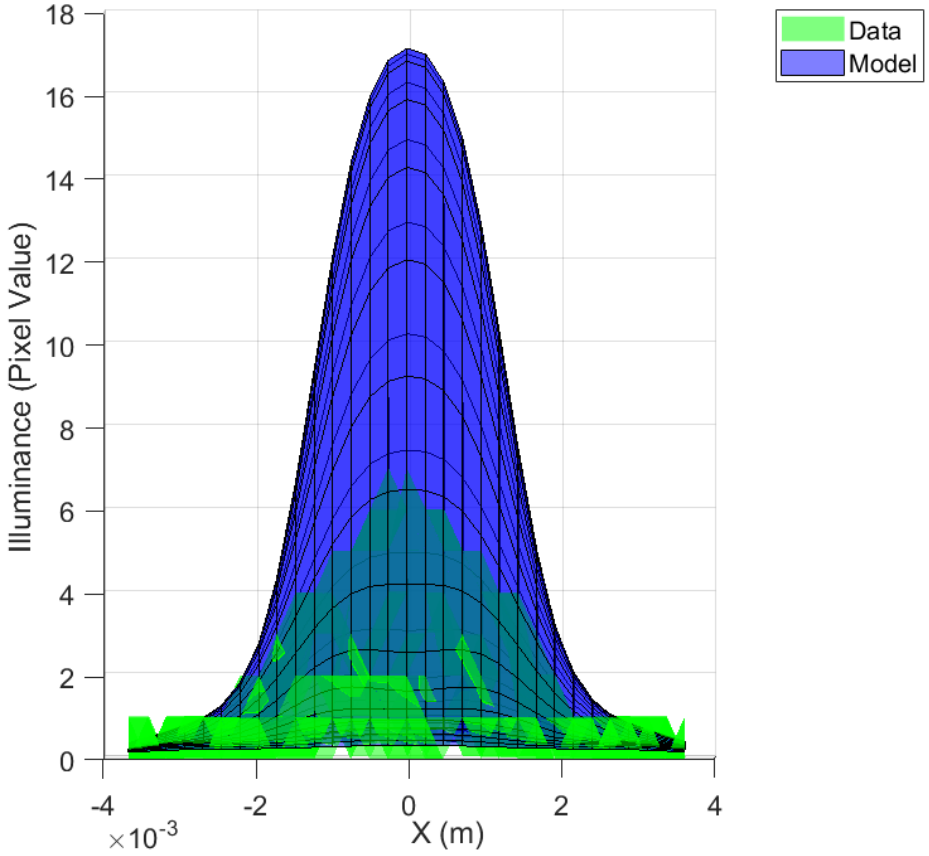

Figure 3.9 The observed (green) and predicted (blue) VUV distributions on the viewing screen from a $P = 1.03$ torr, $I = 1.00$ A plasma transmitted through CNT collimator A (Trial 1, Run 1) with sidewall reflection ($\mathbf{R} = 0.35$). "X" is distance along the y axis on the viewing screen in millimeters. "Illuminance" is the fluorescing phosphor's intensity in pixel value. Note that the predicted distribution matches well the edges of the observed distribution, but the peak discrepancy is increased.

The $\mathbf{R}_x$ values vary between the runs of a given collimator with a trend following the peak intensity values-as the intensity of the source decreases, so does the optimal reflection coefficient. This implies that the reflected portion decreases with lower pressures and currents of the plasma. Our model for the plasma's intensity distribution in the VUV range is based on work done elsewhere(1). The model assumes that in the pressure and current range of 0.50-1.00 torr and 0.50-1.00 A that the intensity distribution is two dimensional and located at the end of the cathode. In that work, we found that it may be possible that the center spot of the intensity distribution to migrate upwards into the bore of the cathode as the pressure is decreased. If this is the case, then at these lower pressures light from the plasma entered the CNT collimators at lower ϕ values. This means that the reflected portion decreases not due to the reflection coefficient changing, but due to less light striking the side walls. Variation in the reflection coefficient between collimators may be due to varying amounts of carbon infiltration from fabrication.

The ring shape of the deposited carbon is peculiar. It may be due to hydrocarbons in the lower chamber breaking down in the VUV light. The energy of VUV photons (58.4 nm wavelength) is more than the bond dissociation energies of many organic molecules(11). These molecules may have drifted into the VUV light, broke down, and deposited onto the phosphor screen. This would form a contamination ring near the edge of the VUV light. Similar phenomenon has been observed for transmission electron microscopes(12).

We suspect the main source of the carbon contamination is the carbon tape used to mount the CNT collimator onto the shim stock. Carbon tape was used because it is relatively flat and thin. Vacuum-compatible epoxy was also tried, but it shifted and tilted the CNT collimator upon contact. This made aligning the CNT collimator with the optical axis during setup very difficult. To reduce carbon contamination and alignment difficulty, a better mounting method is required.

3.4.2 Differential Pumping

To model the collimator's differential pumping, we first list several assumptions made:

- Leaks are insignificant.
- The effect of the aperture on conductance is insignificant.
- The pumping speed is constant.

These assumptions imply that the only significant contributing factor in the pressure ratio is the collimator. Using w as a characteristic length, we find that the minimum Knudsen number in the CNT collimator channels is about 14.5, which implies all collimators were in the molecular flow regime at all pressures observed. We, therefore, use a geometric conductance model. We begin with finding the conductance of a single channel:

$$C_{channel} = \frac{1}{\frac{1}{C_{opening}} + \frac{1}{C_{pipe}}} \tag{3.7}$$

where $C_{opening} = 3.64w^2\sqrt{\frac{T}{M}}$ and $C_{pipe} = 9.70\frac{w^3}{2h}\sqrt{\frac{T}{M}}$, T is temperature in Kelvin, M is the molecular weight of the gas in g/mol, h and w are the height and width of the channel in cm, respectively (13). We add the conductances of all the channels in parallel, and approximate the number of channels as equal to the total area A (cm^2) divided by the area of one channel, $w+t$, where t is the wall thickness.

$$C_c = N_{channels}C_{channel} \approx \frac{A}{A_{channel}}C_{channel} = \frac{AC_{channel}}{(w+t)^2} \tag{3.8}$$

Simplifying, we have:

$$C_c = \left(\frac{w}{w+t}\right)^2 \sqrt{\frac{T}{M}} \frac{A}{0.275 + 0.206\frac{h}{w}} \tag{3.9}$$

Dividing by the pumping speed S in L/s gives the pressure ratio:

$$\frac{P_L}{P_H - P_L} = \frac{1}{S}\left(\frac{w}{w+t}\right)^2 \sqrt{\frac{T}{M}} \frac{A}{0.275 + 0.206\frac{h}{w}} \tag{3.10}$$

The ratio between the data and this model are listed in Table 3.1 under "Data/Model (no leak)". The observed pressure ratios are 13 to 25 times higher than what the model predicts. If we consider a leak in parallel with the CNT collimator, the leak conductance can be optimized such that the model is very close to the observed data (values listed in Table 3.1 under "Optimal Leak"). However, this implies that the observed pressure ratios are mainly due to the leak, not the collimators. In an attempt to minimize the possible leak between the CNT collimator and the carbon tape, we placed epoxy around collimator B and collimator C. However, no significant change in pressure ratio was observed.

Another leak could be between the shim stock diaphragm and the anode. The simple alignment mechanisms of this experimental setup created an inherently leaky system where the leaks were significantly larger than the predicted throughput of the CNT collimator structure. A second system (Fig 3.10) for testing only the differential pumping (no alignment mechanism or light source) was used. Four CNT collimators were mounted onto KF40 2mm restrictors using epoxy and placed into the system. The collimators considered are listed by their width-height dimensions (in microns): 50-301, 50-654, 50-1045, and 200-675. Three trials were conducted for each collimator, where a trial constitutes placing the collimator into the system, pumping down both sides of the system to base pressure, then increasing the pressure on the P_H side by using a controlled air leak. Assuming that there were no leaks between the collimators and the KF40 restrictors, that the aperture's conductance was insignificant, and that the pumping speed was constant, we found the observed pressure ratios were less than the predicted ratios by factors less than 3. The discrepancies in this experiment may have been due to the aperture conductance becoming comparable to the collimators' conductances at lower pressures. Adding an aperture conductance (about 0.099 L/s) calculated using the equations provided in Ohring(13) in series with the collimators improves the theory significantly (Fig 3.11).

Note that the model fits well for the collimators with 50 μm width channels and various heights.

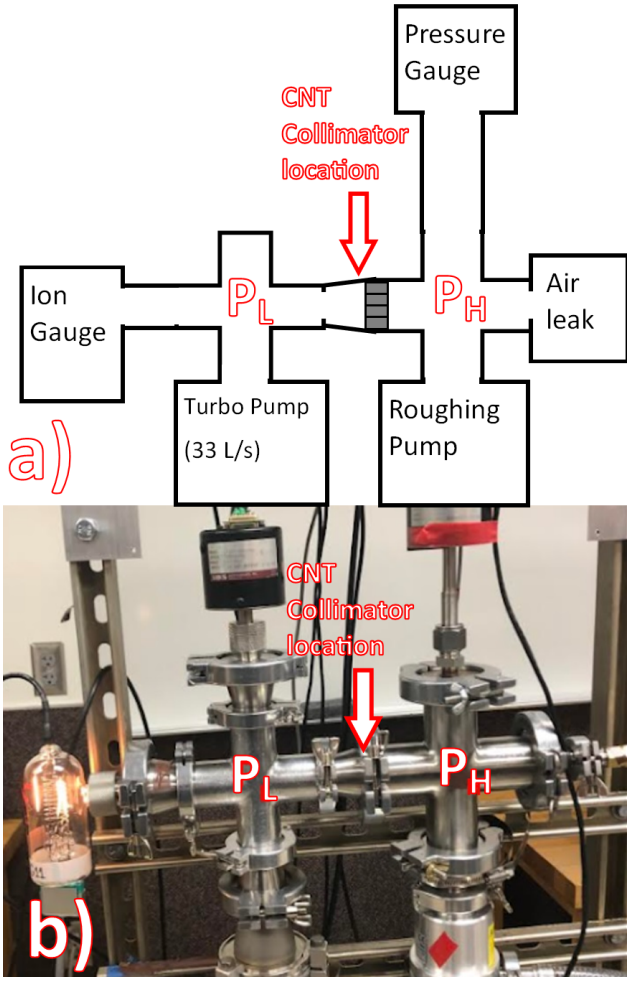

Figure 3.10 a) A diagram of the second system used to solve the possible shim stock leak. The CNT collimator was mounted to a KF40 restrictor between two sides of the system. The left side acted as the low pressure side with an ion gauge, a turbomolecular pump (33 L/s pumping speed), and a roughing pump. The right side acted as the high pressure side with a baratron, a air inlet to manually control the pressure, and a roughing pump. b) Photo of the system.

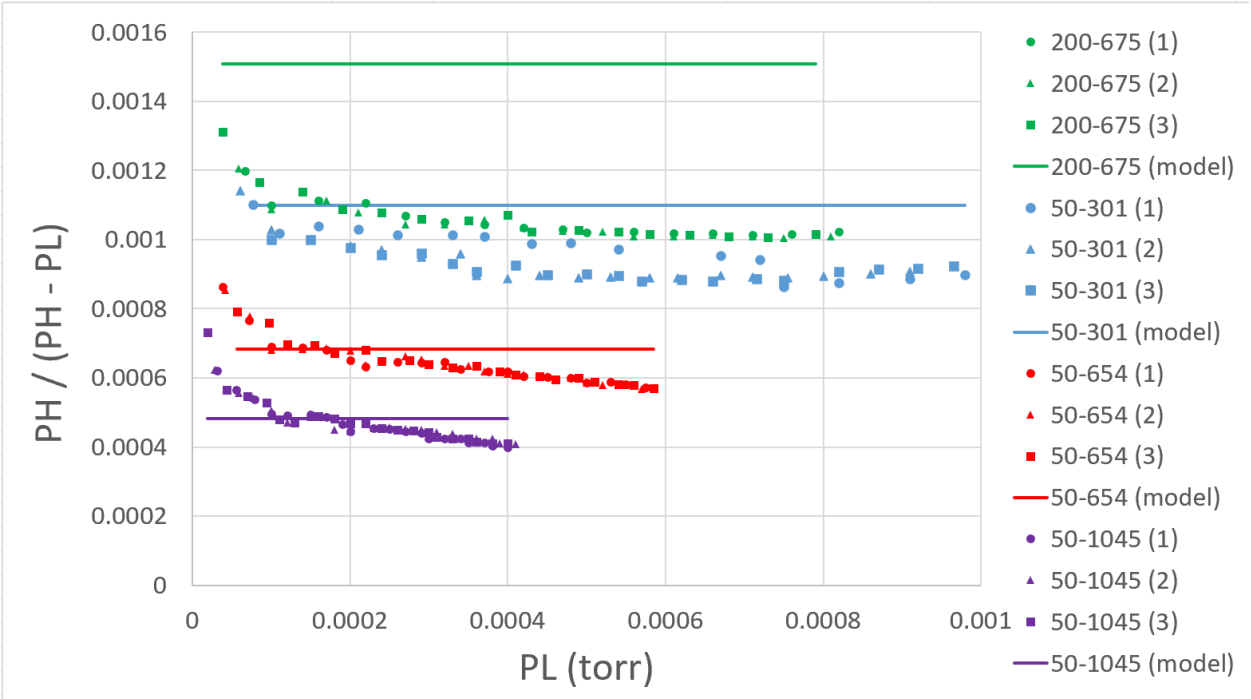

Figure 3.11 Pressure data and model of four CNT collimators with an aperture conductance of about 0.099 L/s included in the model. "P_L" is the pressure in torr of the low pressure side of the second system. "$P_L/(P_H - P_L)$" is the effective pressure ratio between the low pressure side and the high pressure side. Points represent data; lines represent model. Collimators named by their width-height dimensions in microns are a denoted by color and position: green (top) is 200-675, blue (second from top) is 50-301, red (second third from top) is 50-654, violet (bottom) is 50-1045. Different trials are denoted by point symbols: Trial 1 is circles, Trial 2 is triangles, and Trial 3 are squares.

The model for the 200 μm collimator predicts higher pressure ratios than observed. This may be due to the area approximation in the model (Eq 3.8)- as the width of the channels increases, this approximation becomes less valid. Portions of channels that are along the edge of the aperture are partially cut off. This limits the gas flow through the edge channels, which lowers the pressure ratio. The rise in the pressure ratio at lower pressures, which is present for all collimators, may be due to small leaks in the system or the low pressure side approaching its base pressure.

3.5 Conclusion

We have designed, fabricated, and characterized a carbon nanotube collimator that can act as a vacuum ultraviolet window with differential pumping. The design has many variable parameters that allow fine tuning to specific applications. The collimator is easily fabricated using common photolithography and CVD techniques. We observed the VUV transmissions of various collimators using a hollow cathode helium plasma. We found that the collimators considered had peak light transmission of 18% to 37% with carbon deposition on the screen and significant side wall reflection (**R** is about 0.21 ± 0.08 for grazing angles of 15.6 degrees and below). We also found that the collimators can exhibit pressure ratios ($P_L/(P_H - P_L)$ less than 0.001 in a less leaky system.

3.6 Conflicts of Interest

The authors state that there is no conflicts of interest.

3.7 Acknowledgments

We wish to acknowledge Brigham Young University (BYU) Physics Department, the NASA Space Grant Consortium (#NNX15AI24H) and the BYU Graduate Studies HIDRA Fellowship for funding;

BYU Electron Microscopy Facility for providing access to the equipment and expertise that allowed this project to be performed; John Ellsworth and Jeremy Peterson (BYU Physics Machine Shop) for system design and assembly.

Data Availability Statement

The data that support the findings of this study are available from the corresponding author upon reasonable request.

3.8 References

Bibliography

[1] S. Olsen, D. Allred, and R. Vanfleet. Empirical analysis of a hollow cathode's intensity distribution in the vacuum ultraviolet range. Under review for Journal of Vacuum Science and Technology A, 2024.

[2] F. Roberts and S. Anderson. Note: Hollow cathode lamp with integral, high optical efficiency isolation valve: A modular vacuum ultraviolet source. *Rev Sci Instrum*, 84(126101), 2013.

[3] A. Giuliani, I. Yao, B. Lagarde, S. Rey, J. Duval, P. Rommeluere, F. Jamme, V. Rouam, F. Wein, C. De Oliveira, M. Ros, A. Lestrade, K. Desjardins, J. Giorgetta, O. Laprevote, and C. Herbaux. A differential pumping system to deliver windowless VUV photons at atmospheric pressure. *AIP Conf Proc*, 18:546–549, 2011.

[4] R. Preston, C. Brookes, and F. Clutterbuck. Vacuum ultraviolet radiance transfer standard based on an argon mini-arc with integral differential pumping unit. *J Phys E Sci Instrum*, 13:1206–1213, 1980.

[5] K. Nishizawa, K. Ohshimo, and T. Suzuki. Vacuum ultraviolet and soft x-ray photoelectron spectroscopy of liquid beams using a hemispherical photoelectron spectrometer with a multistage system. *J Chin Chem Soc-TAIP*, 60:1403–1410, 2013.

[6] R. Filho, A. Lago, M. Homem, S. Pilling, A. de Brito. Delivering high-purity vacuum ultraviolet photons at the Brazilian toroidal grating monochromator (TGM) beamline. *J Electron Spectrosc*, 156-158:168–171, 2007.

[7] D. Hutchison, N. Morrill, Q. Aten, B. Turner, B. Jensen, L. Howell, R. Vanfleet, and R. Davis. Carbon nanotubes as a framework for high-aspect-ratio MEMs fabrication. *J Microelectromech S*, 19(1):75–82, 2010.

[8] K. Laughlin, R. Vanfleet, and R. Davis. Mechanically robust vertically aligned carbon nanotube composites for applications in ultralow reflectance optical elements. *ACS Appl Nano Mater*, 2022.

[9] T. Westover, S. Olsen, Z. Westhoff, N. Morrill, R. Davis, and R. Vanfleet. Visible and short-wavelength infrared light collimation through carbon nanotube, parallel-hole collimators. *Opt Express*, 30:22679–22686, 2022.

[10] D. Attwood and A. Sakdinawat. Cambridge University Press, 2 edition, 2016.

[11] S. Blanksby and G. Ellions. Bond dissociation energies of organic molecules. *Accounts Chem Res*, 36(4):255–263, 2003.

[12] L. Reimer and M. Wachter. Contribution to the contamination problem in transmission electron microscopy. *Ultramicroscopy*, 3:169–174, 1978.

[13] M. Ohring. Academic Press, 2002.

Chapter 4

Field emission from flipped and patterned vertically aligned carbon nanotube arrays

4.1 Abstract

Carbon nanotubes (CNTs) possess many unique properties that make them ideal for field emission. However, screening due to high density and poor substrate adhesion limits their application. We tested the field emission of various patterned vertically aligned carbon nanotube (VACNT) arrays adhered to copper substrates using carbon paste. After many fabrication steps to improve uniformity, we found that the field emission was dominated by individual CNTs that were taller than the bulk VACNT arrays. After testing a sample with silver epoxy as the binder, we found that the failure mechanism was adhesion to the substrate. Using energy dispersive xray spectroscopy (EDX), we found that the carbon paste migrated into the VACNT bulk volume.

4.2 Introduction

Carbon nanotubes (CNTs) are excellent candidates for field emission. Their thermal, mechanical, and chemical properties make them stable at high temperatures within a high vacuum environment. Their conductivity and high aspect ratio causes the electric field near their tips to increase to hundreds of times greater than the average field, an effect called field enhancement. Applications of CNT field emitters include flat monitors, xray sources, lighting tubes, and microwave radiation generators. However, their performance suffers from issues such as degradation and screening. One cause of degradation is mechanical failure between the CNT and the substrate (1). To avoid this failure, adhesion to the substrate needs to be improved. Various groups have tested many methods of improving adhesion (2). Su, et al improved adhesion by exposing the CNTs to microwaves (3). Li, et al used dopamine as a dopant(4). Yokoyama et al found that the substrate that spray-coated CNTs are deposited on influenced the field emission(5). Srividya et al used a titanium buffer layer deposited onto the substrate before CNT growth. They found that the buffer layer not only improved adhesion, but also reduced CNT density(6).

Reduction of grown CNT density is beneficial to minimize screening. Screening is when the CNTs are so close together that the field enhancement effect is reduced. There is variation in the literature as to the ideal spacing of CNTs, some reporting that it should be twice the height of the CNTs while others reporting it should be half the height (1). Methods of reducing screening include tape activation and plasma treatment by various gases (7). Hazra et al found that patterning the CNTs into hollow pillars also reduced screening(8). Yi et al considered field emission from cracks within CNT films. They found that the films had good field emission due to the cracks reducing screening(9). Poa et al reduced screening by controlling the CNT density mixed into a polystyrene matrix(10). Many of these works involved complicated methods that risk damage to the CNTs.

In this work, we observed field emission from vertically aligned CNT (VACNT) arrays that are adhered to copper substrates via a binder. Patterning has been found to improve the field emission

of VACNT arrays(11). By having various patterns, we could determine if the patterns influenced screening. For binders, we considered first carbon paste and then silver epoxy. We found that the failure mechanism of the samples considered is adhesion to the substrate. The adhesion mechanism of the carbon paste was ion migration from the paste into the VACNT bulk, while the silver epoxy did not show evidence of ion migration. The higher electric field at failure for the carbon paste samples implies that ion migration increases adhesion to the substrate.

4.3 Methods

4.3.1 Fabrication

The procedure followed closely to that given by Hutchison(12). Substrate preparation started with reactive sputtering 70 nm of alumina onto an n-doped Si (100) wafer. The wafer was spin coated with hexamethyldisilazane (HMDS), then photoresist AZ3330, both at 6000 rpm for 60 seconds. After baking at 90 C for one minute, the VACNT pattern was transferred to the photoresist using a Karl Suss Aligner (MA 150 CC) and developed in an alkaline solution. Four nanometers of iron using a thermal evaporator. After dicing the wafer, the die were sonicated in N-Methyl-2-pyrrolidone (NMP) for 20 minutes and dried with nitrogen.

A 1 inch diameter quartz tube furnace (Lindberg/Blue, model number TF55030COMA-1) was used to grow VACNTs. As the furnace heated, the die was under a hydrogen atmosphere (311 sccm) to reduce the iron. CNT growth happened at 750 C with ethylene (338 sccm) and hydrogen for 30 minutes. The ethylene and hydrogen were then replaced with argon (300 sccm) until the furnace cooled to 200 C. The die were removed and allowed to cool to room temperature.

A copper substrate (5.4 x 1.2 x 0.3 cm) was fabricated with a 0.4 mm deep well filled with carbon paste (PELCO High Temperature Carbon Paste, product number 16057). The VACNTs were placed in the carbon paste and the Si wafer was tapped lightly with tweezers to ensure immersion.

The samples were placed into a glass boat, sonicated in a water tank for 5 minutes and placed inside a furnace (Campbell Thermolyne 6000 furnace, model number F6020C-80). The samples were cured at 30 C for 2 hours, 90 C for two hours, and 260 C for two hours with 10 minute, 30 minute, and 60 minute ramp-ups between each. After curing, the samples were allowed to cool to room temperature. The Si wafer was removed by lifting upwards on the corner of wafer using tweezers.

4.3.2 Experiment

The vacuum chamber used to condition the VACNT arrays was a 10 inch conflat cross with two viewports, a side door, a N2 needle valve for venting, two electrical feedthroughs, a vacuum gauge (Type 0531, Varian), and a ionization gauge (Varian, 0563-K2466-303). The chamber was pumped down with a roughing pump (Edwards, model number nXDS10iC 100/24DV) to 1e-2 torr scale. A turbomolecular pump (Pfeiffer model TC 110, model number PM C01 790 A) to 1e-7 Torr scale. During conditioning, an ion pump (Gamma Vacuum, serial number 305058509) pumped down to 1e-8 torr scale. The electrical feedthroughs were connected to a high voltage power supply (Spellman, model number SL6PN300/ESL/115), a pulse generator (Agilent, MY 50004694 33522A), and a high voltage pulse generator (DEI, serial number PVX-4110 110-244). An oscilloscope (Tektronix, MDO34 C018760) read the pulse voltage and current into the program.

Inside the chamber was a test fixture, shown in Fig 4.1. This fixture had a stainless steel base plate (7.6 x 7.6 x 0.6 cm), a stainless steel top plate (7.6 x 7.6 x 1.3 cm) with a threaded hole, and ceramic spacers (3.8 cm long) between them. For conditioning (Fig 4.1-b), the base plate acted as the cathode with the copper substrate clamped down using two stainless steel plates (4.5 x 1.5 x 0.3 cm). An anode (3.3 cm diameter, 1.0 cm thick) was threaded into the top plate and adjusted to a specific height above the copper substrate. The height was set using feeler gauges.

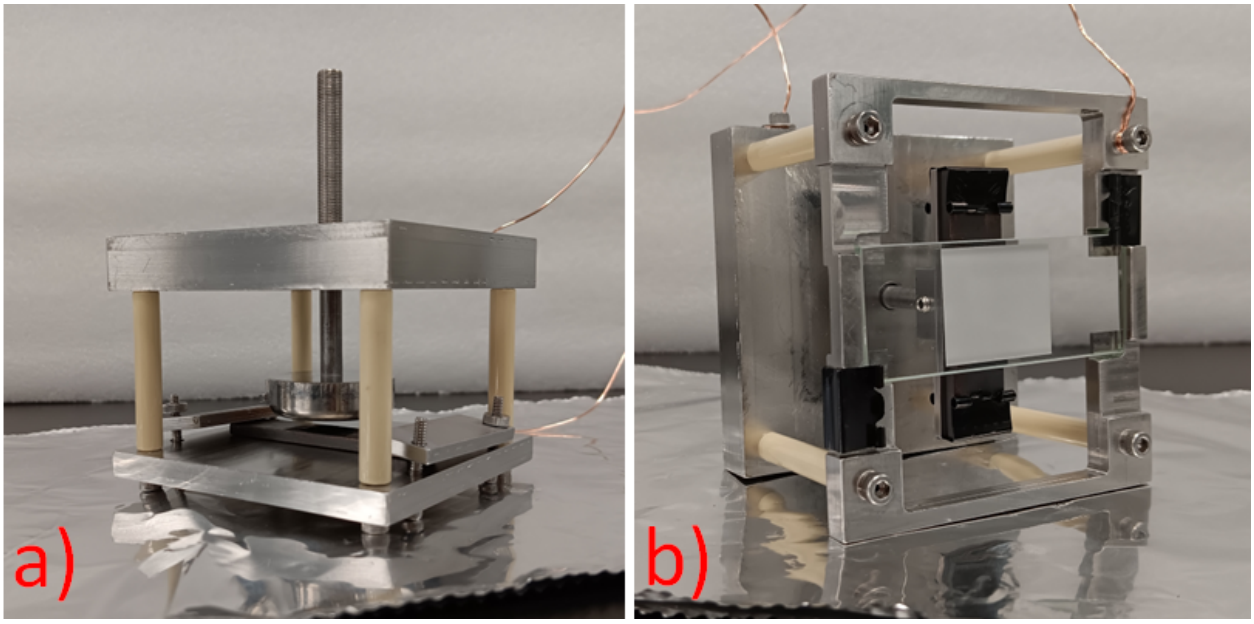

Figure 4.1 a) The testing fixture in the conditioning configuration. The copper substrate is clamped to the base plate underneath the anode. b) The testing fixture on its side in the phosphor screen configuration. For taking phosphor screen images, the fixture base plate was changed for a frame with a mounted phosphor screen and the anode was replaced by a mounting plate to hold the copper substrate (behind the phosphor screen).

For phosphor screen testing (Fig 4.1-c), the same fixture was used but in a flipped configuration. The base plate was replaced with a frame for holding a phosphor screen (0.3175 x 2.54 x 6.35 cm, P43, provided by Scintek) and was wired as the anode. The phosphor screen was held in place with binder clips. The top plate was wired as the cathode and a mounting plate was threaded into the top plate. The copper substrate was mounted to the mounting plate using binder clips and the gap between the substrate and phosphor screen was set using feeler gauges.

4.4 Results and Discussion

Four 9x9 mm patterns were considered: an unpatterned VACNT array (called the 'unpatterned' sample), a grid pattern with 50 micron square channels and 4 micron thick walls (50 micron sample), a grid pattern with 100 micron square channels (100 micron), and a grid pattern with 200 micron square channels (200 micron). SEM images of the 100 micron sample after each processing step are shown in Fig 4.2 and 4.3.

4.4.1 Fabrication

Samples were grown to 1 mm heights. For the 50 and 100 micron samples, this took 30 minutes of growth. For the 200 micron and unpatterned samples, this took 60 minutes. Multiple attempts were tried to mount unpatterned samples to the carbon paste without success. Residual carbon paste on the unpatterned VACNT arrays showed that the samples had good contact with paste, but did not adhere. The unpatterned samples were disregarded for the rest of the study.

After mounting the samples in carbon paste, curing the paste, and removing the Si substrate, the patterns of the VACNT arrays remained relatively intact (Fig 4.3, a). Height images (Fig 4.2, a) show that the samples had outlier CNTs above the height of the bulk. From preliminary trials we found that these outliers tend to dominate the field emission due to their much higher enhancement factor and closer proximity to the anode. In an attempt to remove the outliers, we etched the VACNT arrays using a laser cutter (Universal Laser Systems, PLS6MWXXXX021319119066) with a knife edge fastened to a micrometer to control the height.

After laser cutting, some of the samples still had a significant number of outliers (Fig 4.2, b). The 200 micron sample in particular had many scattered throughout the top. Using a handheld fan, we subjected the samples to a 30 mi/hr air flow for 1 min in an attempt to remove loose CNTs and particulates.

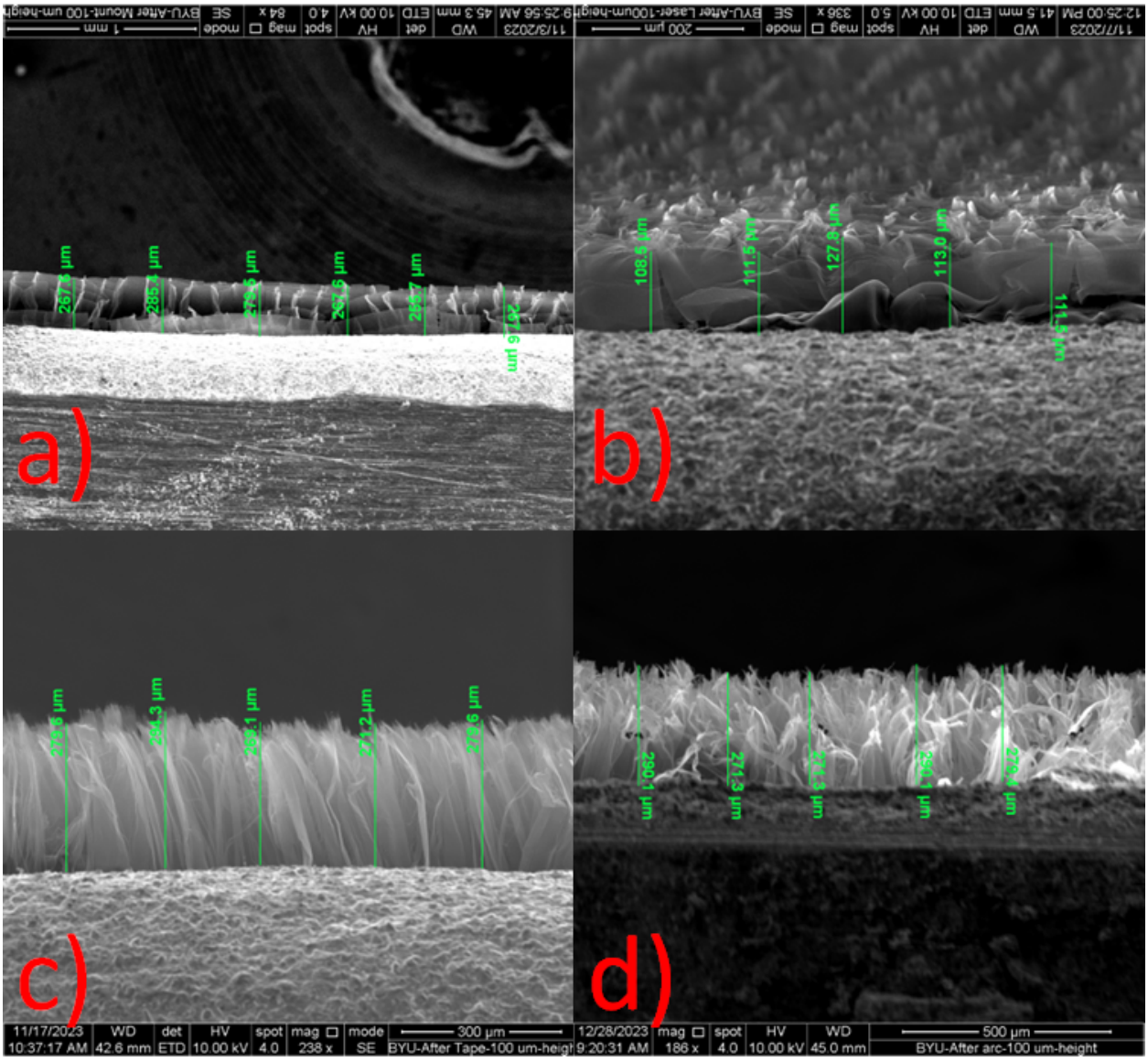

Figure 4.2 The 100 micron sample after: a) mounting, b) laser cutting, c) air flow and tape liftoff, and d) conditioning. In b we see that the laser cutting process is successful in decreasing the height, but not at eliminating outliers. Carbon nanotubes fraying out from the tape liftoff is evident in c, and d shows that the vertically aligned carbon nanotube array became much more disordered through conditioning.

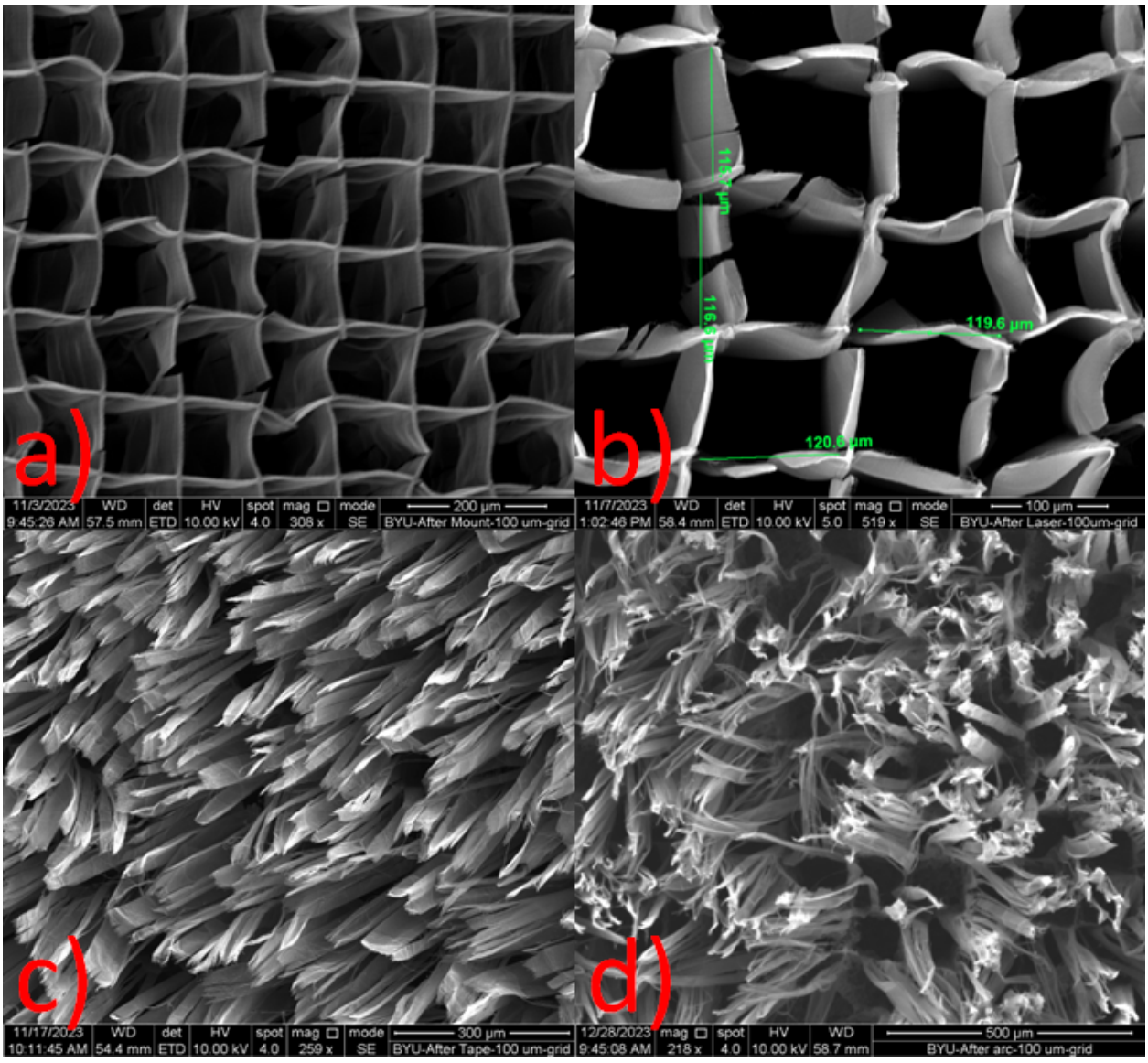

Figure 4.3 The 100 micron sample after: a) mounting, b) laser cutting, c) air flow and tape liftoff, and d) conditioning. In a, we can see that the walls of the vertically aligned carbon nanotube arrays after mounting in carbon paste have a degree of waviness. This waviness seems to be localized near the ends as it doesn't appear close to the substrate after laser cutting in b. Tape liftoff seems to break walls as seen in c. In d, we see that the walls seem to have redistributed during the conditioning process.

We then placed a polyimide film on the samples with 100 um thick paper spacers (calling the step a "tape liftoff"). We did six tape liftoffs for each sample, as well as removed with tweezers any CNTs that could be visually seen. Looking at Fig 4.2 image c, we see that the tape liftoffs compressed many of the CNTs upwards and caused them to fray out. Fig 4.4 shows a zoomed in image of this CNT fraying. In Fig 4.3, c, we also see that the tape liftoffs fractured many of the walls of the samples. The general grid pattern in the 50 micron and 100 micron was still discernible. The 200 micron sample's walls may have been too short to fracture and were instead removed entirely.

4.4.2 Experiment

After tape liftoff, the samples were conditioned in the vacuum chamber. During preliminary trials, we found that the outlier CNTs emitted visible light when driven at high enough voltages (Fig 4.5 shows the 50 micron sample at 950 V and 1.18 V/μm as an example). This may be due to Ohmic heating, which has been observed to degrade CNTs at lower electric fields (1). The heating up of the CNT causes more emission current, which leads to more heating. If the rate of heat dissipation cannot match the rate of heat production, the CNT will continue to heat until there is a vacuum breakdown (13). To avoid this, we conditioned the samples with 100 ms pulses and a 1% duty cycle with small voltage step sizes. After a voltage step, the visible light emission from the sample was watched until it decreased significantly before taking the next step. This procedure continued until the samples arced. We found that the three samples considered arced near the same electric field value: 1.16 V/μm.

SEM images of the samples after they arced (Fig 4.2, d and Fig 4.3, d) show that the 50 micron and 100 micron VACNT arrays became much more disordered. This may be due to electrostatic forces between the fractured CNT walls pushing each other. This introduces a new failure mechanism-VACNT walls breaking due to electrostatic forces.

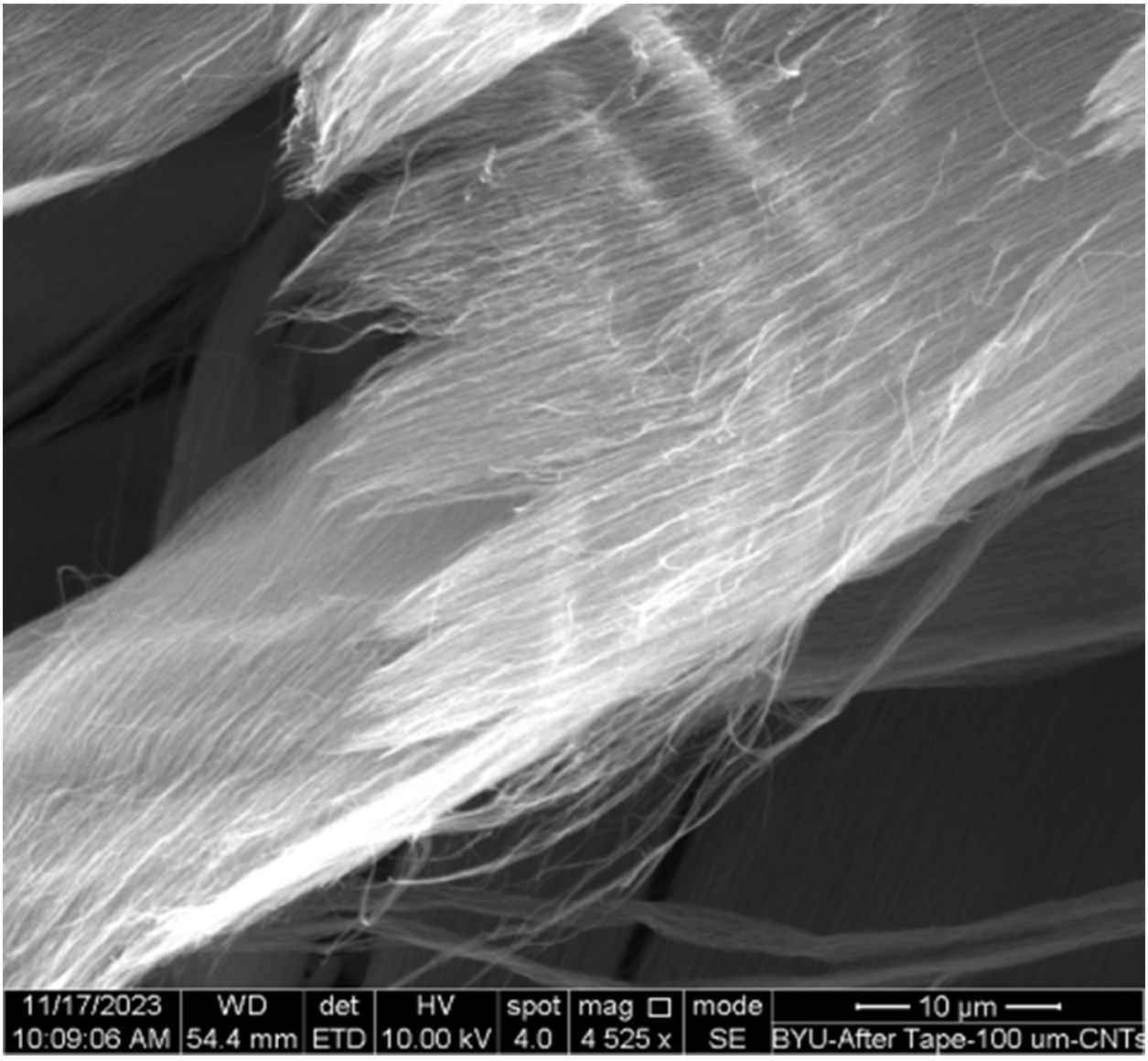

Figure 4.4 The top of a carbon nanotube wall from the 100 μm sample after tape liftoff.

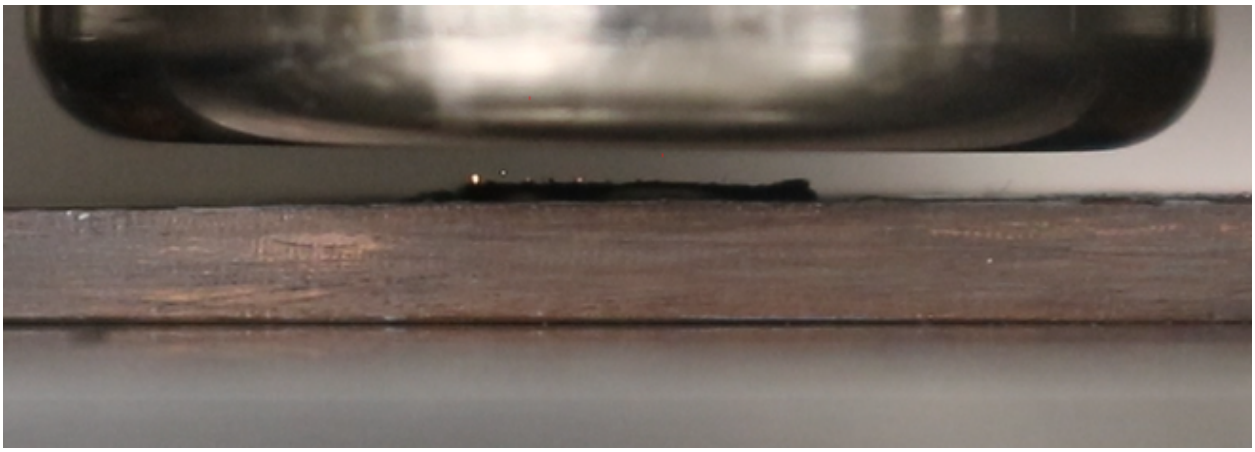

Figure 4.5 The 50 50 μm close to the electric field at failure (1.18 V/μm). Note the visible light emission from the outlier carbon nanotubes.

Sample	$E_{fail}(V/\mu m)$	β	A (cm2)
50 μm	1.18 ($\pm$0.03)	8037	1e-11
100 μm	1.17 ($\pm$0.04)	10524	5e-13
200 μm	1.15 ($+0.03, -0.04$)	8581	9e-11

Table 4.1 Conditioning and modelling results of the three VACNT array samples considered. Values for the field enhancement factor β and the effective emission area A were determined using data shown in Fig 4.8 and Eq 4.2.

To determine which failure mechanism was occurring (adhesion to substrate or breaking due to electrostatic forces), we fabricated another sample using with 100 micron square channels, 4 micron thick walls, and silver epoxy (MG Chemicals, 8331D-14G) as an adhesive (called the 100-silver sample). The 100-silver sample was subject to the same processing steps as the carbon paste samples. SEM images taken after each step showed that the 100-silver sample behaved very similar to the carbon paste samples: the 100 micron square channel pattern was preserved after mounting, waviness in the walls was removed after laser cutting, tape liftoff fractured the walls, and the walls moved during conditioning. However, unlike the carbon paste samples, the 100-silver sample arced at an electric field of 0.91 $(+0.03, -0.04)$ V/μm. The change in E_{fail} with changing the adhesive implies that the failure mechanism is adhesion to the substrate and that the adhesion mechanisms of the carbon paste and silver epoxy are different.

To investigate the adhesion mechanism, energy dispersive xray spectrscopy (EDX) was performed on the 100 micron and the 100-silver samples (Fig 4.6 and 4.7, respectively). Note that for the 100 micron sample, potassium and silicon from the paste is present in the VACNTs up to about 90 microns. EDX on the 100-silver sample showed no migration of silver from the epoxy. If adhesive migration into the VACNT arrays was related to adhesion strength, we would expect the unpatterned sample to not only mount successfully, but also fail at 1.16 V/μm. It has been observed that the upper portion of VACNT arrays tend to have a higher density than the bulk(14). The higher density may have restricted migration of the potassium and silicon molecules into the bulk and therefore weaken the adhesion. The 50, 100, and 200 micron samples also had the upper portion, but their open channels allowed the anions and cations to enter the VACNT bulk from the side, thus enabling high migration into the VACNT arrays. Aligned CNTs have been noted to have high wettability for potassium (15) and low wettability for silver (16).

Current vs. voltage curve data was taken for the carbon paste samples from 0 to about 1 V/um with a 5000 ms pulses and 1% duty cycle (Fig 4.8, a).

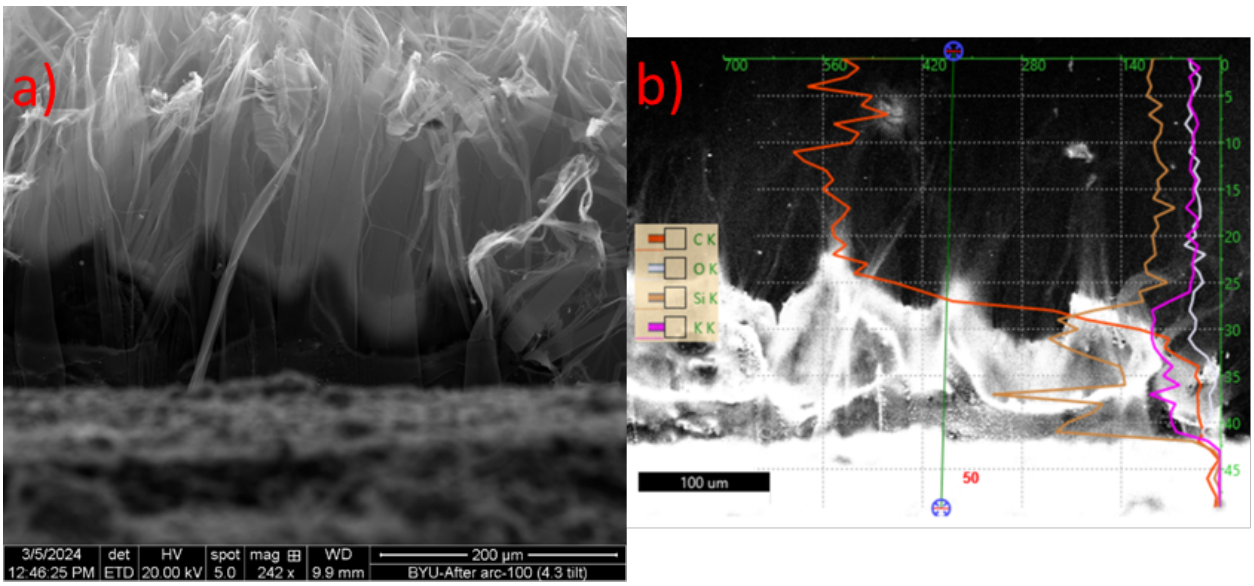

Figure 4.6 a) Scanning electron microscope image from the side of a region of the 100 micron sample. The migration of material from the carbon paste is evident by the darker area of the vertically aligned carbon nanotube array. Note that the sample is tilted by 4.3 degrees. b) Energy-dispersive X-ray spectroscopy image of the region in (a). The darker area seems to have a high proportion of silicon and potassium.

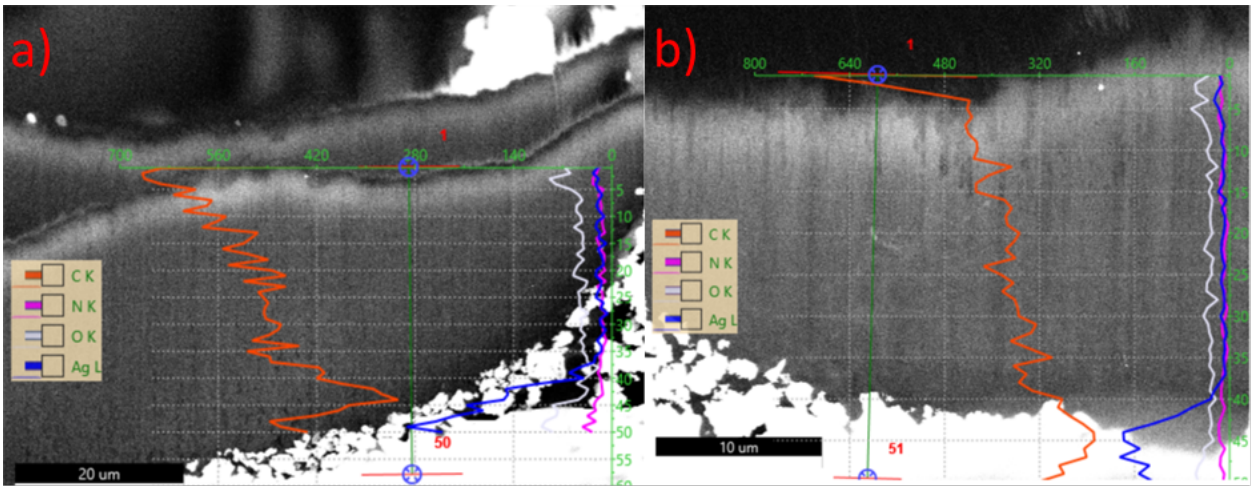

Figure 4.7 a) Energy-dispersive X-ray spectroscopy (EDX) image from the side of a region of the 100 (silver) sample. b) EDX image from the side of a second region. No migration of epoxy components into the vertically aligned carbon nanotube (VACNT) arrays is evident in either region. The epoxy seems to curve upwards near the intersections of the VACNT walls. It also appears that the silver in the epoxy is in the form of microparticles.

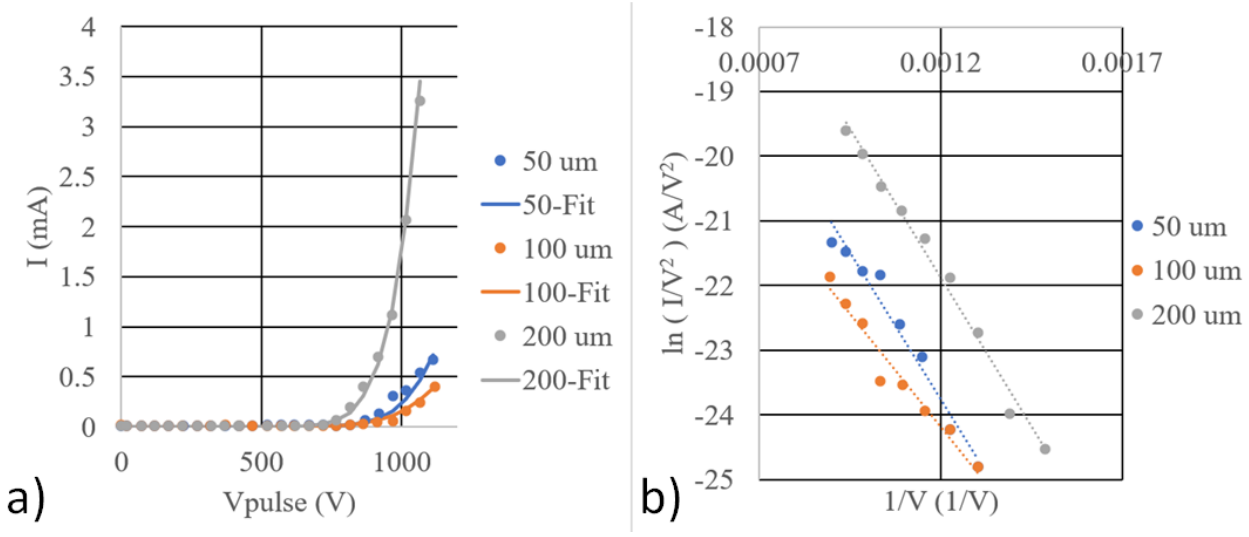

Figure 4.8 a) Currenet vs. Voltage curves for the carbon paste samples. Data are points. Solid lines are fits using Eq 4.2 and values listed in Table 4.1. b) Fowler-Nordheim plot of current vs. voltage data (points) with linear fits (dotted lines).

Fitting a line to a Fowler-Nordheim plot of the data (Fig 4.8, b), we obtained the slopes of the linear portions of the data and calculated the field enhancement factor β using the equation:

$$\beta = \frac{-6.44 * 10^9 \phi^{1.5} d}{m} \tag{4.1}$$

provided by Kim, et al (17), where ϕ is the work function of carbon (5 eV), d is the distance between the anode and the cathode in meters, and m is the slope of the linear fit. We then found the effective emission area A of each sample using the equation (17):

$$I = (1.5 * 10^{-6}) \left(\frac{A}{\phi}\right) \left(\frac{\beta V}{d}\right)^2 e^{\frac{10.4}{\sqrt{\phi}}} e^{\frac{-6.44*10^9 \phi^{1.5} d}{\beta}} \tag{4.2}$$

fitted to each sample with A in m2 and V in V. Both β and A are reported in Table 4.1. The high values of β and the low values of A imply that the field emission is due mainly to outlier CNTs still present on the sample. To observe this, phosphor screen images were taken of the samples, shown in Fig 4.9. It appears that even after the laser cutting, air flow, tape liftoff, and tweezer removal steps, outlier CNTs are still prevalent.

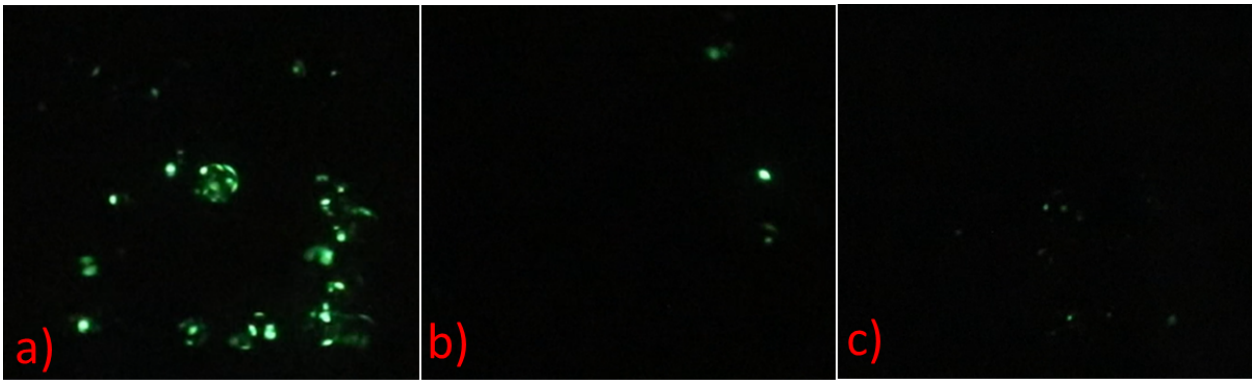

Figure 4.9 Phosphor screen images of the carbon paste samples. Note that the samples are not on the same scale, nor at the same electric field. a) 50 μm, b) 100 μm, c) 200 μm.

4.5 Conclusion

We have investigated the field emission of patterned VACNT arrays flipped into carbon paste and silver epoxy after they have been processed via laser cutting, air flow, tape liftoff, and tweezer removal. We found that the carbon paste samples were able to tolerate a higher electric field than the silver epoxy sample due to the higher wettability of potassium in the paste than silver in the epoxy.

4.6 Conflicts of Interest

The authors state that there are no conflicts of interest.

4.7 Acknowledgments

We wish to acknowledge the support of Brigham Young University (BYU), Varex Imaging Corporation, BYU College of Physical and Mathematical Sciences, and the University of Utah Nanofab.

Data Availability Statement

Data available on request from the authors.

4.8 References

Bibliography

[1] Bocharov G and Eletskii A. Theory of Carbon Nanotube (CNT)-Based Electron Field Emitters. *Nanomaterials-Basel*, 3:393–442, 2013.

[2] Lai R, Shiu J, Chang Y, Lin K, Chang P, Juan C, Tai H, and Cheng H. Properties of Carbon Nanotubes Via a Thin Ti Capping Layer on the Pretreated Catalyst. *J Electrochem Soc*, 154(3):J109, 2007.

[3] Su H, Chen C, Chen Y, Yao D, Chen H, Chang Y, and Yew T. Improving the adhesion of carbon nanotubes to a substrate using microwave treatment. *Carbon*, 48:805–812, 2010.

[4] Li W et al. Enhanced adhesion of carbon nanotubes by dopamine modification. *Langmuir*, 35:4527–4533, 2019.

[5] Yokoyama M, Hung P, Su S, and Sun M. Field emission characteristics of carbon nanotubes deposited on various metal cathodes. In *2013 International Symposium on Next-Generation Electronics*, pages 510–512, 2013.

[6] Srividya S et al. Titanium buffer layer for improved field emission of CNT based cold cathode. *Appl Surf Sci*, 256:3563–3566, 2010.

[7] Kim J, Jeong T, Baik C, Park S, Han I, Kim G, and Yu S. Field-emission performance and structural change mechanism of multiwalled carbon nanotubes by oxygen plasma treatment. *Thin Solid Films*, 547:202–206, 2013.

[8] Hazra K, Gigras T, and Misra D. Tailoring the electrostatic screening effect during field emission from hollow multiwalled carbon nanotube pillars. *Appl Phys Lett*, 98:123116, 2011.

[9] Yi C, Wu H, Li J, Song Y, Song Y, Chen X, Ou-Yang W. Crack-assisted field emission enhancement of carbon nanotube films for vacuum electronics. *Acs Appl Nano Mater*, 2:7803–7809, 2019.

[10] Poa C, Smith R, and Silva S. Field emission from nonaligned carbon nanotube-polymer matrix cathodes. *J Vac Sci Technol B*, 21:1715–1719, 2003.

[11] Pimenov S, Frolov V, Zavedeev E, Abanshin N, Du H, Chen W, Chen L, Wu J, and Chen K. Electron field emission properties of highly dense carbon nanotube arrays. *Appl Phys A-Mater*, 105:11–16, 2011.

[12] Hutchison D, Morill N, Aten Q, Turner B, Jensen B, Howell L, Vanfleet R, and Davis R. Carbon Nanotubes as a Framework for High-Aspect-Ratio MEMS Fabrication. *J Microelectromech S*, 19(1):75–82, 2010.

[13] Huang N, She J, Chen J, Deng, S, Xu N, Bishop H, Huq S, Wang L, Zhong D, Wang E, and Chen D. Mechanism responsible for initiating carbon nanotube vacuum breakdown. *Phys Rev Let*, 93(7):075501, 2004.

[14] Zhang L, Li Z, Tan Y, Lolli G, Sakulchaicharoen N, Requejo F, Mun B, and Resasco D. Influence of a top crust of entangled nanotubes on the structure of vertically aligned forests of single-walled carbon nanotubes. *Chem Mater*, 18:5624–5629, 2006.

[15] Qin L, Lei Y, Wang H, Dong J, Wu Y, Zhai D, Kang F, Tao Y, and Yang Q. Capillary encapsulation of metallic potassium in aligned carbon nanotubes for use as stable potassium metal anodes. *Adv Energy Mater*, 9(29):1901427, 2019.

[16] Gopee V. *Vertically aligned multiwalled carbon nanotubes as electronic interconnects*. University of Surrey (United Kingdom), 2016.

[17] Kim Y, Hur J, Kim I, Park S, Jung T, Kim D, Kim H, Cha S, Han I, and Kim J. Activation-free printed carbon nanotube field emitters. *Nanotechnology*, 22(435601):435601, 2011.

[18] Kim Y et al. The exterior of single-walled carbon nanotubes as millimeter-long cation-preferring nanochannel. *Chem Mater*, 30:5184–5193, 2018.

Chapter 5

Conclusion

We have presented the current research done for various EUV and xray applications of CNT devices. Some of this research provides foundation for future work, such as:

- Field emission from vertically aligned carbon nanotube arrays-the adhesion mechanisms presented in this work do not include all the mechanisms that have been considered. Other mechanisms are being researched to determine their potential.

- Tungsten infilled lobster eye optic (Appendix A)-the tungsten ALD system at BYU is currently under repair. When repaired, a CNT collimator draped onto a spherical surface can be tested for reflectance and rigidity.

- CNT supported microplasma (Appendix C)-the modelling presented in this work shows that EUV and xray emission from Sn and Cu doped vertically aligned CNT arrays is feasible, but there is no data to support this. It may be worthwhile to determine if this application is indeed feasible and beneficial.

Appendix A

Carbon nanotube collimator as a lobster eye optic

A.1 Introduction

Wolter-Schwarzschild mirrors have been used in previous astronomical instruments, such as the WFC (1), and the EUVE (2). In the EUV-SXR regime, these mirrors can have high reflectance by utilizing total external reflection. However, the angle at which total external reflection occurs depends on the material, the wavelength being observed, and is generally very small (close to the surface) (3). This greatly limits the field of view, and lowers the resolution for off-axis sources. To increase the resolution, the telescope must be very large. As an example, the Chandra mission telescope had a resolution of 1 arc second, but was over 10 meters long (4).

An alternative to Wolter-Schwarzschild mirrors is lobster eye optics (LEOs). Macruran crustaceans, such as lobsters, have small square channels along the surface of their eyes. Inside these channels the surface is reflective. The hemispherical arrangement of the channels focuses light onto a hemispherical retina (Fig A.1).

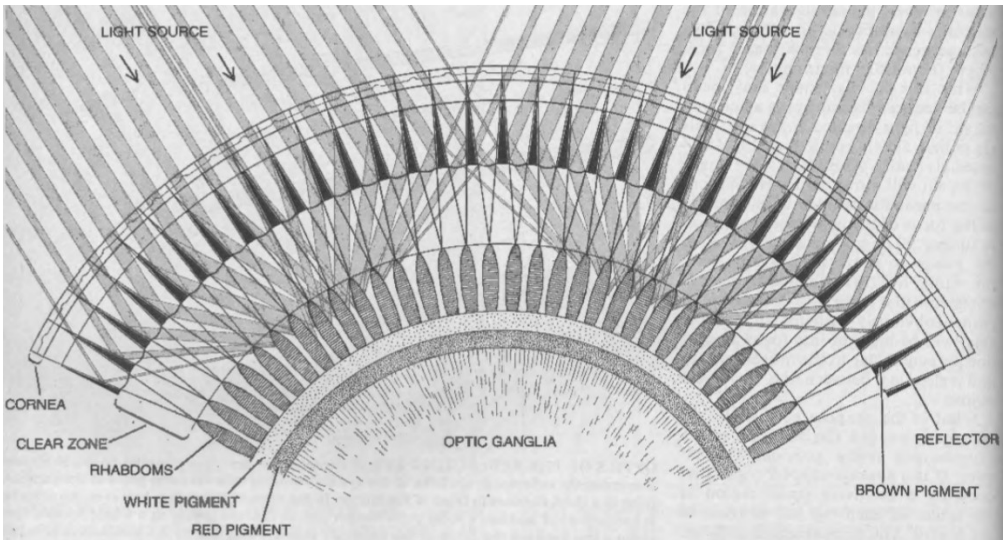

Figure A.1 Diagram of a lobster's eye, courtesy of (4).

Because the surface is spherical, there is no preferred axis, eliminating off-axis aberrations. The design also has no theoretical limit to the field of view. The square shape of the channels aids in focusing. It has been found that the less square the channels are, the more broad the focus becomes. No LEOs have been included in xray missions as of date due to difficulty in fabricating them to meet necessary image requirements (4).

We propose an LEO design that involves conforming a CNT collimator onto a spherical surface, then infiltrating the collimator to maintain shape and improve reflectivity. Multiple attempts to fabricate a CNT LEO have been conducted. We found that it is possible to conform a CNT collimator to a spherical or cylindrical surface while maintaining the integrity of the collimator structure. Infiltration of the CNT collimator to maintain its shape proved to be more difficult.

A.2 Method

Fabrication involved 2 requirements: conforming the CNT collimator to shape, and infiltrating the collimator with the material to hold the shape and improve reflectivity. Multiple fabrication attempts

were considered, including:

- Infiltration with parylene-C and bending the CNT collimator into shape.
- Draping the collimator into shape after growth, then infiltration with carbon.
- Bending the collimator into shape during growth, then infiltration with carbon.
- Draping the collimator onto a spherical surface and infiltrating with tungsten.

A.2.1 Parylene-C

We first considered parylene-C. Parylene has many unique properties, such as being bioccompatible, biostable (5), high tensile strength, and high mechanical strength (6). The tensile strength may allow the CNT collimator to be bent mechanically, meaning it would have a tunable focal length. The conformal coating may diminish surface roughness, allowing for high reflectance, improving the collimator's focusing ability. And the chemical inertness allows for many of the processing steps to remain unchanged, such as KOH etching. A parlyene LEO would involved a parylene-infiltrated collimator mounted to a flexible diaphram that is later curved to obtain the desired focal length.

Parylene infiltration was done for various CNT samples: 4 collimators, 2 die of beams of various widths used for 3-point-bending tests, and 2 die of circular post arrays. Half the samples were ozone treated. The samples were then mounted to a clean wafer via carbon tape. About 211 nm of parylene was deposited using the University of Utah Nanofab's system. Samples were then removed from the wafer. A non-ozone treated and ozone treated 3-point-bending post were removed from the substrate, cut using a knife edge, and imaged in a SEM (Fig A.2 and A.3, respectively). We note that the parylene is a very conformal but shallow infiltration.

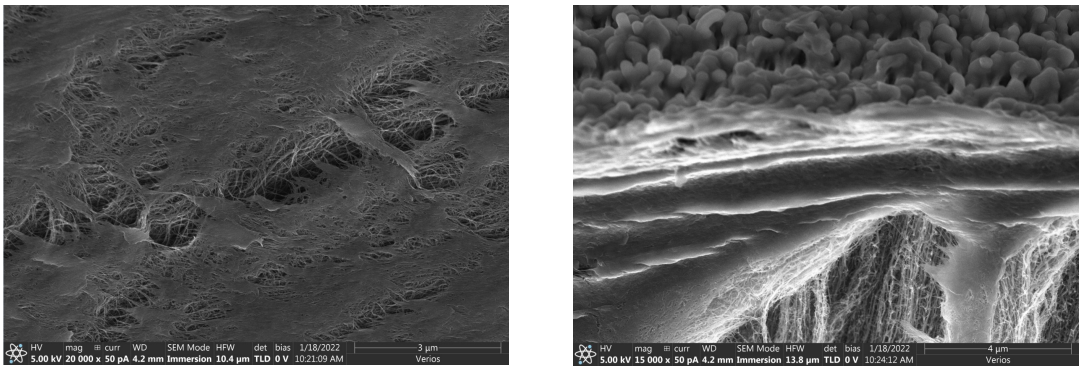

Figure A.2 Non-ozone treated 3-point-bending CNT sample infiltrated with 211 nm of parylene-C

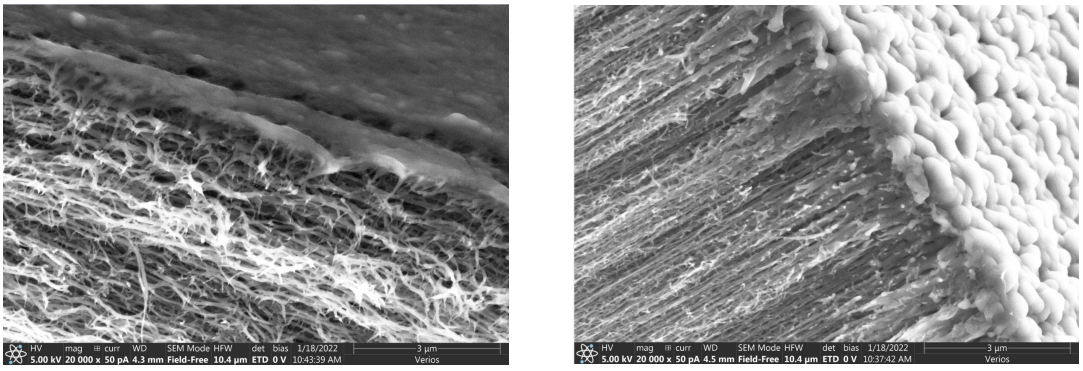

Figure A.3 Ozone treated 3-point-bending CNT sample infiltrated with 211 nm of parylene-C

The non-ozone treated samples had low adhesion between the CNTs and the parylene-it appears from the images that as the knife edge cut into the beam, the parylene outer layer was stretched over the surface, ripping in a few places, exposing the bare CNTs underneath. The ozone treated samples had higher adhesion-the samples were significantly more stiff, and the knife edge made a clean cut.

Because the walls of the collimator pattern are fairly thin (about 4 microns), a shallow infiltration from both sides may still fully infiltrate the collimator. Fig A.4 shows the walls of an ozone-treated collimator that was cut using a knife edge. The collimator had 100 micron square pores and was about 1 mm tall. We note that the collimator was infiltrated thoroughly, even to the base.

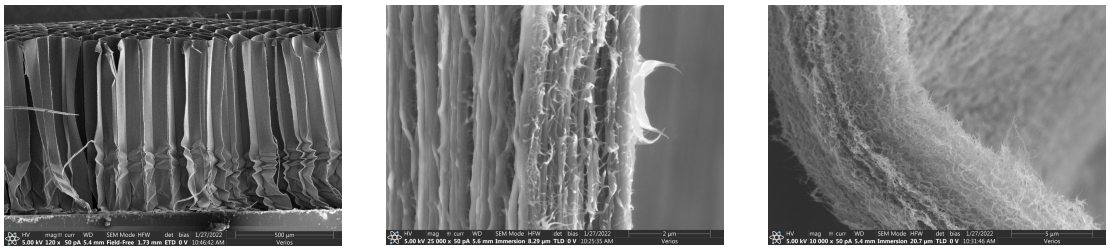

Figure A.4 Images of ozone treated CNT collimator infiltrated with 211 nm of parylene-C

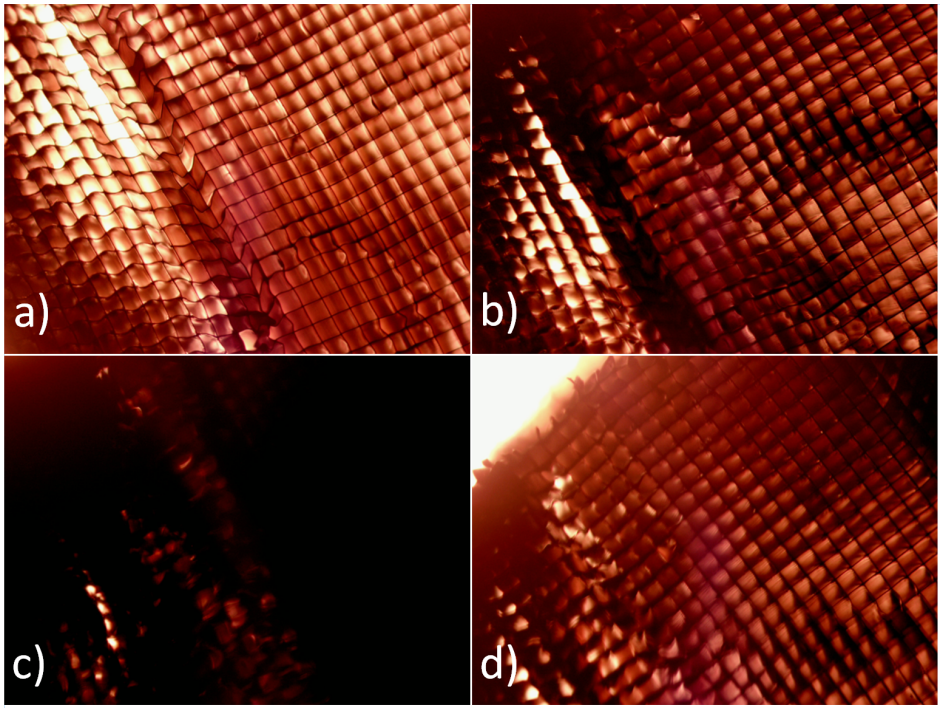

Figure A.5 Parylene-C infiltrated CNT collimator exhibiting elastic behavior, viewed using an optical microscope. a) No compression. b) Intermediate compression. c) Maximum compression. d) No compression. Note the integrity of the channels is maintained after maximum compression.

The same collimator was removed from the substrate via a KOH bath. Portions of the collimator separated or contracted, leaving only a small portion available for testing. The remaining portion was mounted to a small shim stock diaphram and illuminated with a 405 nm LED. The parylene LEO was found to be elastic (Fig A.5) and have significant side wall reflection (Fig A.6). However, we could not confirm that it focused the light, and after prolonged use it began to degrade and rip.

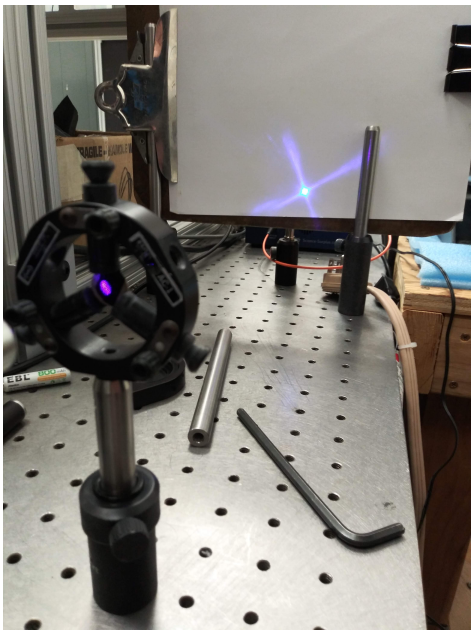

Figure A.6 Light transmission demonstrated for the parylene-C infiltrated CNT collimator. The direct beam interference pattern and the reflected interference pattern were both observable. However, focusing of light was not observable.

A.2.2 Carbon

We next considered C infiltration. 50, 100, and 200 μm channel width collimators were grown via CVD and etched using a heated 45% KOH bath. The samples would float when placed in the solution. Once the substrate was removed, the Si die would sink while the collimators remained floating. The 200 μm collimators tended to collapse, the 100 μm were occasionally successful, and the 50 μm were often successful. The floating may be due to the multiwalled CNTs being hydrophobic (7). The collapsing may be due to internal stresses. In the case of the 50 μm, the internal stresses are balanced by the solution present in the column. For the 200 μm, the solution in the column is low enough that the CNT walls can glide over the surface with less effort, causing the whole to collapse. 100 μm seems to be the limit for the given KOH concentration.

After the KOH bath, the CNT collimators were removed using a curved quartz boat to conform the collimator to shape. We note that the integrity of the collimator was maintained after removal.

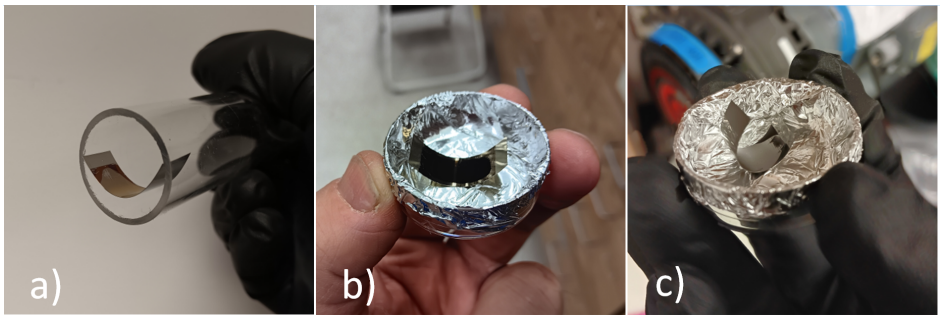

Figure A.7 a) Shim stock substrate with CNT collimator pattern placed in quartz tube preparatory for CNT growth. b) CNT collimator grown on shim stock substrate. Note that the substrate maintains the curfe after removal from the quartz tube. c) CNT collimator grown on shim stock substrate and infiltrated with carbon. Note that the curvature of the substrate increased during the infiltration.

The sample was then placed in a CVD furnace, heated to 900 C under a H atmosphere, and infiltrated using ethylene for several minutes. It was found that the C infiltration destroyed the collimator, as only debris was left afterwards. This may be due to KOH being highly reactive to C at high temperatures (8). However, we found that if the KOH was removed via water from the sample before infiltration, the CNT collimator would collapse.

It appeared that in order for carbon infiltration to be successful, the CNT collimator must be conformed to a curved surface without involving KOH. To do this, we grew the CNT collimators on a curved surface using shim stock substrates. The substrates were roughly 0.3 x 1.0 x 3.0 mm. They were polished and coated with 50 nm of Al2O3. After photolithography, 4 nm of iron were deposited via thermal evaporation. For growth, the substrates were placed inside a 2.2 mm diameter quartz tube, which caused the substrates to bend (Fig A.7, a). Growth was done at 750 C for 5 minutes and 30 minutes. After growth, the shim stock substrate remained curved (Fig A.7, b). Using an optical microscope, we observed that the integrity of the CNT channels was also preserved. Carbon infiltration was done at 900 C for 5 minutes. After infiltration, the shim stock substrate curved significantly (Fig A.7, c). The sample was placed in a KOH bath. However, after several weeks in the bath, the CNT collimator did not separate from the substrate.

A.2.3 Tungsten

We next considered an atomic layer deposition (ALD) process. We have two ALD systems at BYU: a tungsten system and an aluminum oxide system. The tungsten system is inoperable. We intend to repair the tungsten system and create a CNT LEO by etching the CNT collimator off a silicon substrate via a KOH bath, draping the collimator onto a curved surface, infiltrating with tungsten, then remove the collimator from the curved surface by rinsing with water.

A.3 References

Bibliography

[1] R.S. Warwick. *EUV Astronomy with the Rosat Wide Field Camera*, pages 57–66. Springer Netherlands, Dordrecht, 1994.

[2] M.M. Sirk, J.V. Vallerga, D.S. Finley, P. Jelinsky, and R.F. Malina. Performance of the extreme ultraviolet explorer imaging telescopes. *The Astrophysical Journal*, 110:347–356, 1997.

[3] D. Attwood and A. Sakdinawat. Cambridge University Press, 2 edition, 2016.

[4] S. Barbour. Lobster eye optics: A theoretical and computational model of wide field of view x-ray imaging optics, 2015.

[5] T. et al Xiaolong. Patterned parylene c for cell adhesion, spreading and alignment studies. *Microelectronic Engineering*, 175:56–60, 2017.

[6] X. et al Xiong. Directed asembly of high density single-walled carbon nanotubes patterns on flexible polymer substrates. *Nanotechnology*, 20(29), 2009.

[7] Haruka Kyakuno, Mamoru Fukasawa, Ryota Ichimura, Kazuyuki Matsuda, Yusuke Nakai, Yasumitsu Miyata, Takeshi Saito, and Yutaka Maniwa. Diameter-dependent hydrophobicity in carbon nanotubes. *The Journal of Chemical Physics*, 145(6):064514, 08 2016.

[8] E. Raymundo-Piñero, P. Azaïs, T. Cacciaguerra, D. Cazorla-Amorós, A. Linares-Solano, and F. Béguin. Koh and naoh activation mechanisms of multiwalled carbon nanotubes with different structural organisation. *Carbon*, 43(4):786–795, 2005.

Appendix B

Vertically aligned carbon nanotube arrays as templates for zone plate arrays

B.1 Introduction

Due to the high absorbance and the refractive index being less than 1, unique optical element designs and materials are necessary in the EUV-SXR range. Included in these unique designs are Fresnel zone plates, which use diffraction to focus incoming light. Zone plates can focus 2D images with a resolution approaching the diffraction limit. They also have multiple orders of focus, and can be designed with additional functionality, such as modifying the angular momentum of the incoming radiation (1).

CNTs have been used to make zone plates in the visible region (2). A high resolution CNT zone plate would be difficult in the EUV-SXR range due to the resolution of a zone plate being proportional to the outermost zone width (1), and the difficulty of fabricating CNTs with high precision. However, this assumes that the zone plate is optically thin (said to be in in the Raman-Nath regime).

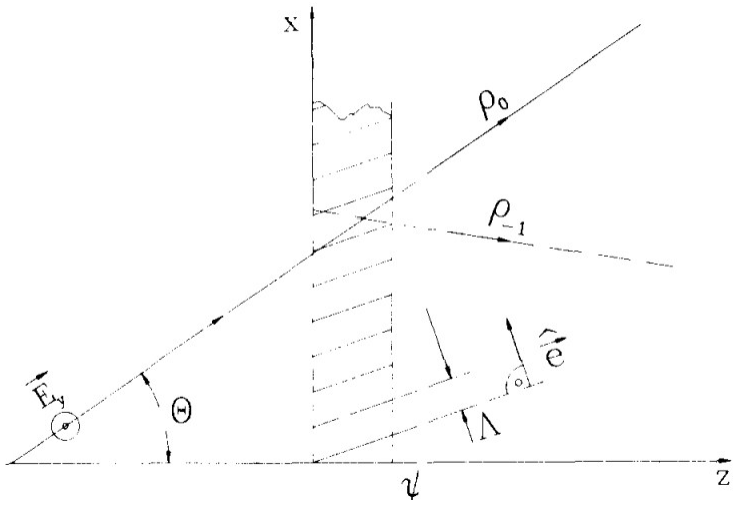

Figure B.1 Coupled Wave Theory Approach used by (3) to describe the effect of a grating on an incident electric wave. Image courtesy of (3).

If the zone plate is optically thick (Bragg regime), then the resolution depends on the zones meeting the Bragg condition. Intermediate of these two extremes can produce resolution better than the outermost zone would traditionally allow (3). We may be able to utilize the high aspect-ratio of CNTs to fabricate a EUV-SXR zone plate with high resolution.

B.2 Theory

The approach used by (3) to describe this intermediate regime was coupled wave theory (CWT), where the zone plate is treated like a grating, shown in Fig B.1. We consider an incident plane wave $\vec{p_0}$ onto a zone plate with a grating vector $\vec{G} = (2\pi/\Lambda)\hat{e}$, where $\Lambda = 2dr_n$, dr_n is the width of the nth zone, and $\hat{e}$ is the unit vector perpendicular to the zones. A set of eigenmodes p_l will be excited in the grating according to the conservation of momentum:

$$p_l = p_0 + l\vec{G} \tag{B.1}$$

Each eigenmode will have an amplitude A_l. The resulting electric field will then be the sum of the eigenmodes:

$$E(z) = E_0 \sum_{l=-\infty}^{\infty} A_l e^{-i\vec{p}_l \cdot \vec{r}} \tag{B.2}$$

where z is the thickness of the grating (in our case the height of the CNTs), and E_0 is the incident electric field at the front of the grating $z = 0$. $E(z)$ must obey the wave equation, here written as:

$$\nabla^2 \cdot E(\vec{r}) - \gamma^2 E(\vec{r}) = 0 \tag{B.3}$$

where $-\gamma^2 = -i\omega\mu_0\sigma + (\omega^2/c^2)\varepsilon_r'$ is the complex propogation constant, $\sigma = \omega\varepsilon_0\varepsilon_r''$ is the electrical conductivity, c is the speed of the light in a vacuum, ω is the angular frequency, ε_0 is the permittivity of free space, μ_0 is the permeability of free space, ε_r' is the real part of the relative permittivity of the zone plate, and ε_r'' is the imaginary part. Here we account for the shape of the zone plate by describing it in terms of the permittivity. We set:

$$\hat{\varepsilon}_r = \varepsilon_{r0}' - i\varepsilon_{r0}'' + (\varepsilon_{r1}' - i\varepsilon_{r1}'')C \sum_{h=1}^{\infty} N_h \sin(h\vec{G} \cdot \vec{r}) \tag{B.4}$$

where $\varepsilon_{r0}' - i\varepsilon_{r0}''$ is the average permittivity and $\varepsilon_{r1}' - i\varepsilon_{r1}''$ is the modulation depth. Substituting Eq B.2 and B.4 into the wave equation, neglecting second derivatives, we have:

$$[-l(G/k)\sin\psi + \cos\theta]\frac{\partial A_l}{\partial z} + (\alpha + i\vartheta_l)A_l + \hat{\kappa}C \sum_{h=-\infty}^{\infty} N_h(A_{l+h} - A_{l-h}) = 0 \tag{B.5}$$

where k is the wave number in the material of the grating, ψ is the angle of the zones with respect to the central axis, θ is the angle of the incident wave with respect to the central axis, $\alpha = k/\varepsilon_{r0}''$ is the average absorption constant, ϑ_l describes how 'far' the wave is off from the Bragg condition and $\hat{\kappa} = (k/4\varepsilon_{r0}')(\varepsilon_{r1}' - i\varepsilon_{r1}'')$ is the complex coupling constant.

Now, we can substitute values for our CNT zone plate, simplify the equation, and use an ODE solver to evaluate the A_l terms. First, CNTs grow perpendicular to the surface of the substrate. This means $\psi = 0$. Next, if we consider a point source located at the focus, we have $\cos\theta = \frac{f}{\sqrt{f^2+r^2}}$,

where r is a location along the zone plate. ϑ is equal to $\frac{k^2-p_l^2}{2k}$, where we can write $p_l^2 = \vec{p}_l \cdot \vec{p}_l = p_0^2 + 2l\vec{p}_0 \cdot \vec{G} + G^2$. $p_0^2 = k^2$, $G^2 = (2\pi/\Lambda)^2$, and $\vec{p}_0 \cdot \vec{G} = \frac{2\pi kr}{\Lambda\sqrt{f^2+r^2}}$.

We next derive the equation for the permittivity function $\hat{\varepsilon}_r$ to describe the shape of the zone plate. The equation for a normalized square wave is $f(x) = \frac{4}{\pi}\sum_{k=1}^{\infty} \frac{\sin\frac{(2k-1)\pi x}{L}}{2k-1}$, where L is the length of a period. We then invert it, reflect across the y axis by multiplying by $\frac{x}{|x|}$, and make L a function of position- half of L is the distance between two zones r_n and r_{n-1}. We estimate $L = 2(r_n - r_{n-1}) = 2(\sqrt{n\lambda f} - \sqrt{(n-1)\lambda f})$, using equations from (1). We then scale and offset to complete $f(x)$, match its terms with those of $\hat{\varepsilon}_r$ to find C and N_h. We use the arguments inside the sine terms to rewrite the k index of $f(x)$ into the h index of $\hat{\varepsilon}_r$.

Solving for $\frac{\partial A_l}{\partial z}$ in Eq B.5, substituting these and other necessary values we have the final ODE to solve:

$$\frac{\partial A_l}{\partial z} = (a+ib)A_l - c\sum_{h=-\infty}^{\infty} \frac{1}{h}(A_{l+h} - A_{l-h}) \tag{B.6}$$

where:

$$a = \frac{-\pi\varepsilon''_{r0}\sqrt{\varepsilon'_{r0}}\sqrt{f^2+r^2}}{\lambda f} \tag{B.7}$$

$$b = \frac{\pi l r}{f dr_n} + \frac{\pi\lambda\sqrt{f^2+r^2}}{4f dr_n^2\sqrt{\varepsilon'_{r0}}} \tag{B.8}$$

$$c = \frac{-r(\varepsilon'_r - 1 - i\varepsilon''_r)dr_n\sqrt{f^2+r^2}}{2\lambda f|r|\sqrt{\varepsilon'_{r0}}(\sqrt{n\lambda f} - \sqrt{(n-1)\lambda f})} \tag{B.9}$$

$$dr_n = \frac{\sqrt{n\lambda f}}{2n} \tag{B.10}$$

with the assumptions:

- The CNTs grow perpendicular to the zone plate
- The light source is a point source located at the focus

B.3 Results and Discussion

Eq B.6 was solved (with finite h) using ode45 in Matlab with $\lambda = 13.5$ nm; $f = 1$, 0.5, and 0.1 m; for carbon, aluminum, silicon, and silicon nitride, with 20% and 100% infiltration. The intensity $A_l^* A_l$ of several diffraction orders l were plotted as functions of zone plate height z at various locations along the zone plate. Plots for all materials with $f = 1$ m are given in Figures B.6 and B.11.

The highest $A_l^* A_l$ value appears to be about 0.25 in the first order at $z = 0.7$ microns for 100% silicon nitride. Less infiltration seems to stretch the peak to $z = 2$ microns and $A_l^* A_l \approx 0.1$. Shortening the focal length f did not have a noticeable effect.

CNT growth tends to be very fast, about 15 microns after 1 min as a reference. A uniform height of 0.7 microns would be very difficult to achieve. Also, these results do not consider misalignment of the CNTs, which could "fuzz" out the zone boundaries, diminishing intensity and resolution. Also, the surface roughness of the CNTs may play a factor. Compared to the theoretical intensity in the first order of zone plates (about 0.10, (1)), a tall CNT zone plate may not be a worthwhile endeavor.

Though a tall zone plate composed of CNTs may not be worthwhile, an array of zone plates patterned by CNTs might be. A zone plate array (ZPA) can be used in maskless lithography, which is beneficial for low-volume manufacturing, experimentation, and design verification. Scanning electron beam lithography is common, but is very limited in throughput. ZPA lithography uses a computer to modulate the light on individual zone plates while moving a wafer through the zone plates' focal plane. By synchronizing the wafer movements and light modulation, patterns are printed in a dot matrix fashion (4).

Figure B.12 shows the process by which a CNT ZPA could be fabricated. We begin with vertically aligned CNTs. We then infiltrate the CNTs using atomic layer deposition (ALD), alternating between two materials.

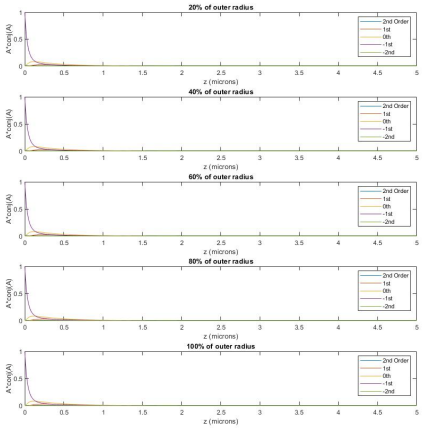

Figure B.2 Aluminum

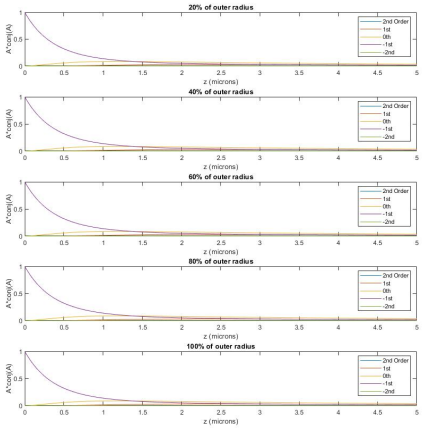

Figure B.3 Silicon

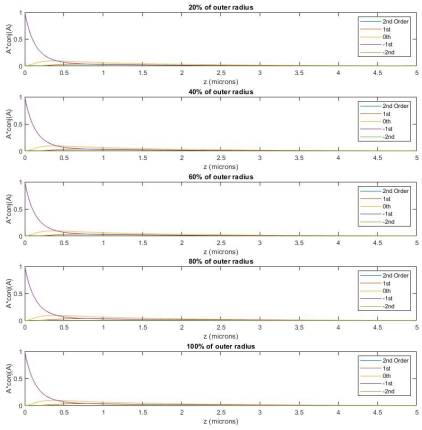

Figure B.4 Carbon

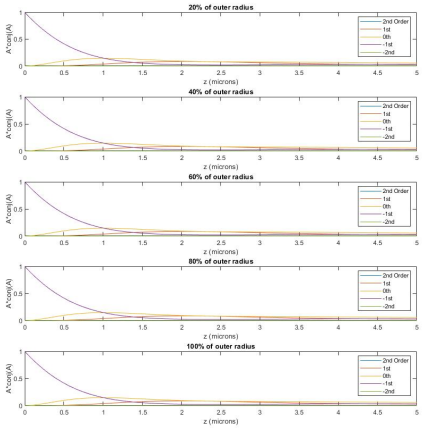

Figure B.5 Si3N4

Figure B.6 20% Infiltration, $\lambda = 13.5$ nm, $f = 1$ m.

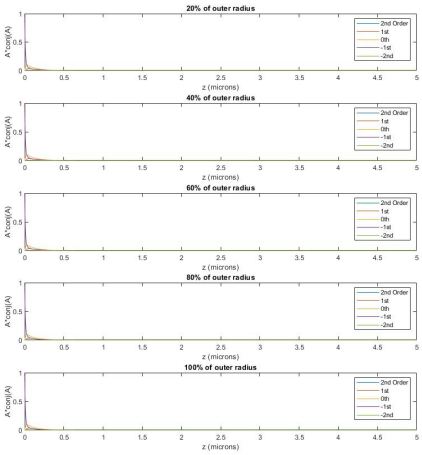

Figure B.7 Aluminum

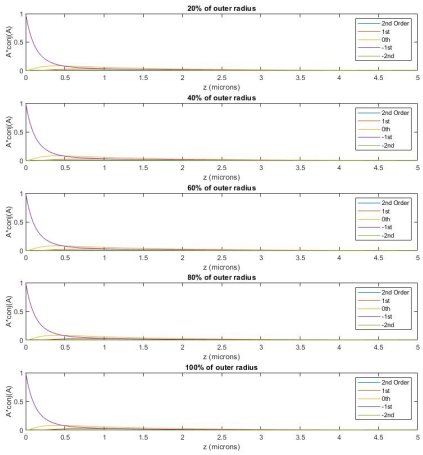

Figure B.8 Silicon

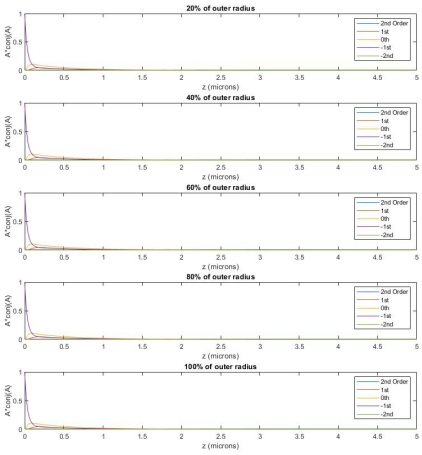

Figure B.9 Carbon

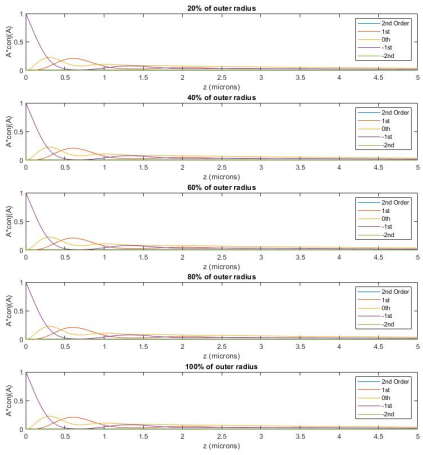

Figure B.10 Si3N4

Figure B.11 100% Infiltration, $\lambda = 13.5$ nm, $f = 1$ m.

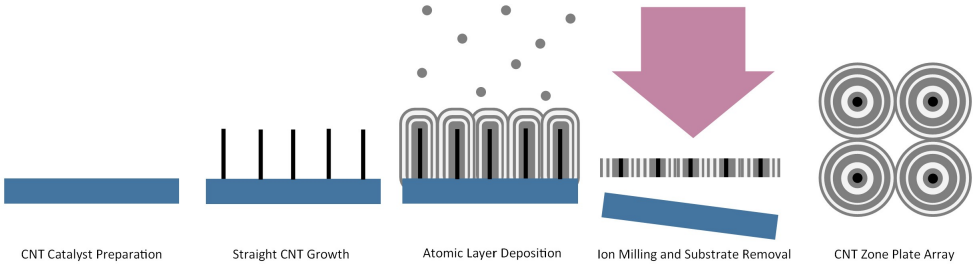

Figure B.12 Possible process of a CNT-templated zone plate array (ZPA)

We then directionally etch the surface to make the infiltrated CNTs a desired thickness. A support layer can then be deposited on top, and the substrate removed. The result is a ZPA with the zone plate locations defined by the CNTs and zone thicknesses defined by the ALD process. Because ALD can deposit very thin layers, the outermost zones of the zone plates may be very thin, improving resolution.

The first challenge in designing a CNT ZPA is to grow CNTs that are straight. It has been observed by several groups that an electric field parallel to the CNT axis encourages directional growth ((5), (6), (7), (8)). An apparatus was designed to grow CNTs subject to an electric field in a quartz furnace (Figure B.13). The apparatus involved a smaller quartz tube, mounted to a KF40 blank via epoxy, with 4 slits on the opposing end to suspend two copper plates parallel to each other. Wires spot-welded to the plates connected to a high voltage connection also mounted to the KF40 blank via epoxy. A small opening was cut near the KF40 end on the quartz tube to ensure feedstock would flow inside the tube. The high voltage connection was connect to a voltage source. Growths were done with various voltages at 750 C, with 311 sccm hydrogen and 338 sccm ethylene for about 1 minute duration.

Voltages ranged from -2500 to 2000 V (with the CNT substrate being ground). Figures B.14 thru B.18 give SEM images of the CNTs with -2300, -1300, 0, 1000, and 2000 V.

Figure B.13 Apparatus for CNT growth in presence of electric field by CVD quartz tube furnace.

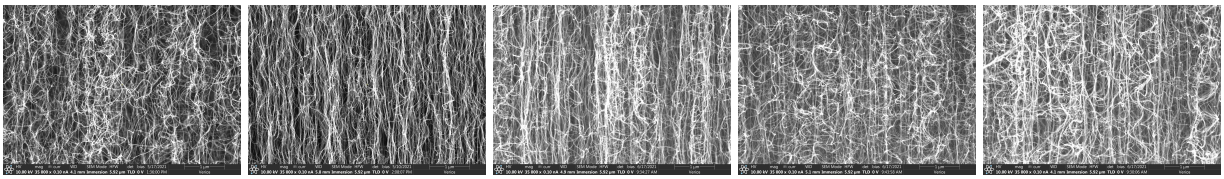

Figure B.14 -2300 V

Figure B.15 -1300 V

Figure B.16 0 V

Figure B.17 1000 V

Figure B.18 2000 V

With a 6 mm gap between the copper plates, this corresponds to electic fields of about -380000, 217000, 0, 167000, and 333000 V/m. We observe no significant influence by the electric field on CNT straightness. This may be due to several factors. One factor may be the process gases removing charge at the end of the CNTs as they flowed past. Without charge buildup at the ends of the CNTs, there would be no force to straighten the CNTs. Another factor may be the van Der Waals forces between the CNTs. These forces between the CNTs may have been greater than the force between the CNTs and the electrode.

B.4 References

Bibliography

[1] D. Attwood and A. Sakdinawat. Cambridge University Press, 2 edition, 2016.

[2] S. et al. Deng. Carbon nanotube array based binary gabor zone plate lenses. *Scientific Reports*, 7, 2017.

[3] J. Maser and G. Schmahl. Coupled wave description of the diffraction by zone plates with high aspect ratios. *Optical Communications*, 89:355–362, 1992.

[4] H. et al. Smith. Zone-plate-array lithography: A low-cost complement or competitor to scanning-electron-beam lithography. *Microelectronic Engineering*, 83:956–961, 2006.

[5] T. et al. Matsuda. Role of negative electric field biasing on growth of vertically aligned carbon nanotubes using chemical vapor deposition. *Japanese Journal of Applied Physics*, 47(9):7436–7439, 2008.

[6] Y. Avigal and R. Kalish. Growth of aligned carbon nanotubes by biasing during growth. *Applied Physics Letters*, 78(16):2291–2293, 2001.

[7] C. Luo, G. Liu, and M. Zhang. Electric-field-induced microsctructure modulation of carbon nanotubes for high-performance supercapacitors. *Frontiers of Materials Science*, 13(3):270–276, 2019.

[8] J. AuBuchon, L. Chen, A. Gapin, and S. Jin. Electric-field-guided growth of carbon nanotubes during dc plasma-enhanced cvd. *Chemical Vapor Deposition*, 12:370–374, 2006.

Appendix C

Vertically aligned carbon nanotube array supported microplasma for EUV production

C.1 Introduction

With a shorter wavelength of 13.5 nm, compared to the commonly used 193 nm, EUV can be used in lithography to produce smaller and finer features. However, EUV lithography involves several complications. One is a high power light source. A laser-produced Sn plasma is an attractive source due to its strong radiation in the EUV range. However, the Sn debris deposits onto the reflective optics of the lithography system, lowering their reflectivity over use (1).

Multiple solutions of this debris problem have been employed, such as electrostatic fields, magnetic fields, and ambient gas. One solution is to lower the Sn density in the target. It has been found that targets containing 15% Sn emit more strongly near the 13.5 nm peak than solid Sn targets. It was later found that the optimal Sn concentration in Sn-doped foam targets for EUV emission is less than 1%, at the price of a slightly lower conversion efficiency (2).

We considered the EUV produced by a Sn-infiltrated CNT forest. The advantages of using CNT

forests include:

- It has been noted that CNTs in a vacuum may not be damaged when exposed to laser intensities below $5 \cdot 10^{12}$ W/cm^2 (1.25 micron wavelength) (3), meaning the CNT forest may be a reusable target.
- The interaction of a CNT with incident light is a function of polarization (4), meaning absorption of the IR laser by the CNTs may be minimized, perhaps leaving more energy to be absorbed by the Sn particles.
- CNT forests are mostly empty space (5), meaning there is less material to absorb the produced EUV.
- Because the CNTs may not be destroyed, Sn particles evaporated in the IR laser path may redeposit onto CNTs located elsewhere, minimizing debris, and allowing for multiple runs with a single target.
- The majority of the Sn debris is ions when using mass-limited targets (6). With CNTs being electrically conductive (5), a voltage may be applied to the target to produce an electrostatic field, which will attract the Sn ions, further minimizing debris on the optics, and making the target more reusable.

C.2 Theory

Fig C.1 shows our model of the CNT-supported microplasma. The two factors we would like to optimize are the Sn concentration and the width of the target. We begin by considering the amount of power $\delta P_{absorbed}$ absorbed at a given location in the CNT forest (r, θ, z), where r is the distance from the optical axis and z is the distance into the sample.

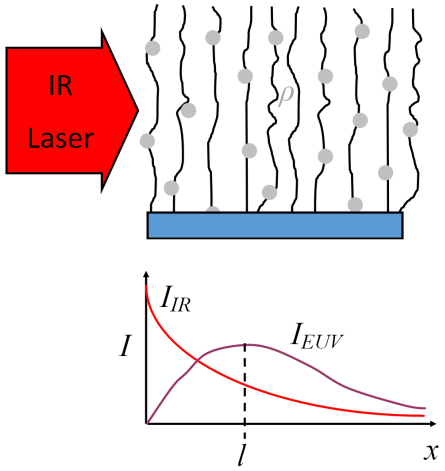

Figure C.1 Model for vertically aligned carbon nanotube array supported microplasma for EUV production. An IR laser irradiates the CNT array that is doped by a volume fraction ρ of Sn particles. We anticipate the intensity of the IR laser to decrease exponentially through the CNT array. This causes the EUV intensity to increase initially due to production, reach a maximum, then decrease due to absorption.

For an infinitismal area δA at (r,θ,z) we then have:

$$\delta P_{absorbed} = (I_{in} - I_{out})\delta A \tag{C.1}$$

Assuming the Sn-infiltrated CNT forest absorbs some of the IR, we have $I_{out} = I_{in} exp(\frac{-4\pi\beta_{IR}\delta z}{\lambda_{IR}})$, where β_{IR} is the imaginary part of the refractive index for IR laser wavelength λ_{IR}. Because δz is infinitismal, we can approximate the exponential term using a Taylor series. We then have:

$$\delta P_{absorbed} = I_{in}\left(\frac{4\pi\beta_{IR}\delta z}{\lambda}\right)\delta A \tag{C.2}$$

The fraction of the energy absorbed that is emitted as EUV is described using the Coefficent of Efficiency C_E (2). Substituting the proper equation for I_{in}, writing δA into cylindrical coordinates, we have the EUV power emitted at point (r,θ,z):

$$\delta P_{emitted} = C_E I_{IR} e^{\frac{-4\pi\beta_{IR}z}{\lambda_{IR}}}\left(\frac{4\pi\beta_{IR}}{\lambda_{IR}}\right)\rho r\delta r\delta\theta\delta z \tag{C.3}$$

Where I_{IR} is now the incident intensity profile of the laser, a function of r and θ. Assuming that this

power is emitted spherically, we can write:

$$\delta I_{EUV} = \frac{\delta P_{emitted} e^{\frac{-4\pi\beta_{EUV}R}{\lambda_{EUV}}}}{4\pi R^2} \tag{C.4}$$

where R is the distance from (r,θ,z) to a location of interest (r',θ',z'). If we focus our attention to the EUV intensity on the optical axis immediately past the CNT forest, we can set $R^2 = r^2 + (l-z)^2$, where l is the width of the CNT forest. We can then combine equations C.3 and C.4:

$$\delta I_{EUV} = I_{IR}\left(\frac{C_E\beta_{IR}\rho}{\lambda_{IR}(r^2+(l-z)^2)}\right) e^{\frac{-4\pi\beta_{IR}z}{\lambda_{IR}}} e^{\frac{-4\pi\beta_{EUV}\sqrt{r^2+(l-z)^2}}{\lambda_{EUV}}} r\delta r\delta\theta\delta z \tag{C.5}$$

Summing all the portions within the laser's profile we have the total EUV intensity on the optical axis just outside the CNT forest. Rearranging the terms, assuming I_{IR} is symmetric so that the $\delta\theta$ integral is trivial, we have:

$$I_{EUV} = \frac{2\pi\beta_{IR}\rho}{\lambda_{IR}} \int_0^l \int_0^R \frac{C_E I_{IR} \exp\left(-4\pi\left[\frac{z\beta_{IR}}{\lambda_{IR}} + \frac{\sqrt{r^2+(l-z)^2}\beta_{EUV}}{\lambda_{EUV}}\right]\right)}{r^2+(l-z)^2} r\delta r\delta z \tag{C.6}$$

where R is redefined as the radius of the laser intensity profile.

C_E is left inside the integral as it is a function of laser intensity (therefore a function of r and z), as well as a function of ρ (2). A rough linear fit with respect to $\log(I_{IR})$ and ρ to data provided by (2) (Fig C.2) gives C_E as:

$$C_E = (0.278\rho + 1.921)\log(I_{IR}) - (2.499\rho + 12.276) \qquad \log(I_{IR}) \leq -0.387\rho + 11.931 \tag{C.7}$$

$$-(0.791\rho + 0.704)\log(I_{IR}) + (9.106\rho + 10.355) \quad \log(I_{IR}) > -0.387\rho + 11.931 \tag{C.8}$$

$$\tag{C.9}$$

where I is in units of W/cm2, and ρ is in units of % volume.

β_{IR} and β_{EUV} are also functions of ρ. To estimate β_{IR}, we first determine the effective permittivity of the CNTs, the derivation is given by (4).

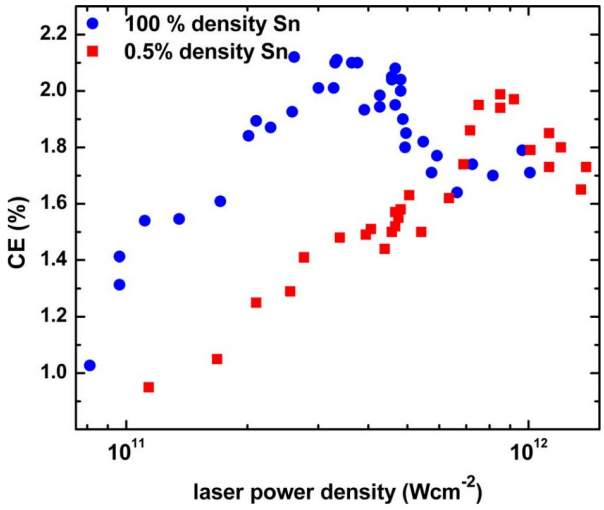

Figure C.2 Coefficient of Efficiency C_E for various tin concentrations and laser intensity. Image courtesy of (2).

We model the CNTs as solid, perfectly straight graphite rods:

$$\varepsilon_{eff}^{\perp} = \frac{\sqrt{\varepsilon_e \varepsilon_o}(1+f) + \varepsilon vac(1-f)}{\sqrt{\varepsilon_e \varepsilon_o}(1-f) + \varepsilon vac(1+f)} \tag{C.10}$$

$$\varepsilon_{eff}^{\parallel} = f\varepsilon_o + (1-f)\varepsilon_{vac} \tag{C.11}$$

where $\varepsilon_{eff}^{\perp}$ is for polarization perpendicular to the CNTs, $\varepsilon_{eff}^{\parallel}$ is for polarization parallel to the CNTs, ε_o is the ordinary dielectric function of graphite, ε_e is the extraordinary dielectric function of graphite, f is the fill factor, and $\varepsilon_{vac} = 1$. To account for misalignment, we can introduce an alignment factor x:

$$\varepsilon_{CNT}^{\perp} = x\varepsilon_{eff}^{\perp} + (1-x)\varepsilon_{eff}^{\parallel} \tag{C.12}$$

$$\varepsilon_{CNT}^{\parallel} = x\varepsilon_{eff}^{\parallel} + (1-x)\varepsilon_{eff}^{\perp} \tag{C.13}$$

We assume that the emitted EUV is unpolarized, therefore β_{EUV} can be calculated common EUV/SXR databases using carbon with CNT density.

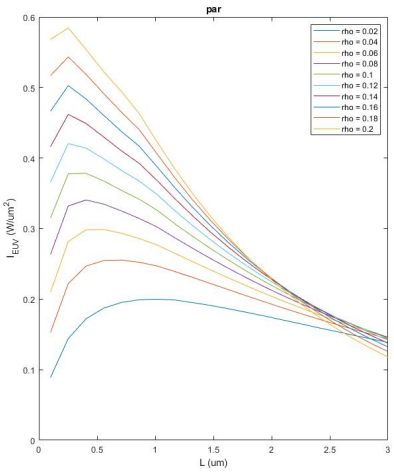

Figure C.3 I_{EUV} along optical axis just outside CNT forest infiltrate with ρ volume ratio of Sn with the IR laser polarization parallel to the CNT axis.

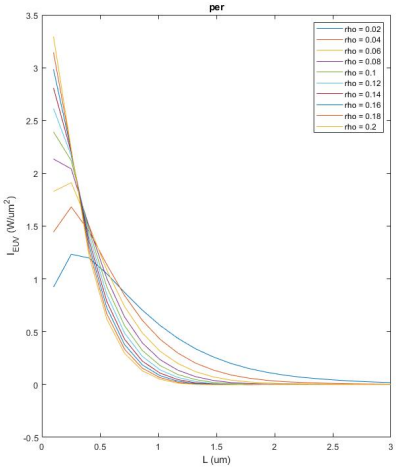

Figure C.4 I_{EUV} along optical axis just outside CNT forest infiltrate with ρ volume ratio of Sn with the IR laser polarization perpendicular to the CNT axis.

To account for the Sn particles, we use the Maxwell-Garnet Approximation(7):

$$\varepsilon = \varepsilon_{CNT}\left[1+\frac{3\rho(\varepsilon_{Sn}-\varepsilon_{CNT})}{\varepsilon_{Sn}+2\varepsilon_{CNT}-\rho*(\varepsilon_{Sn}-\varepsilon_{CNT})}\right] \tag{C.14}$$

and then use $(1-\delta+i\beta)^2 = \mathrm{Re}\{\varepsilon\}+i\mathrm{Im}\{\varepsilon\}$ (4) to find β_{IR} and β_{EUV}.

C.3 Results and Discussion

Equations C.6, C.9, and C.14 were written into a Matlab script to test various ρ and l values. For all tests, the IR laser was assumed to have a Gaussian profile with $\lambda_{IR} = 800$ nm, $\sigma = 12.5$ microns, $I_{peak} = 10000$ W/micron2. For the CNTs, for all tests $f = 0.03$ and $x = 0.95$. Figures C.3 and C.4 give I_{EUV} as a function of l for various ρ with $\lambda_{EUV} = 13.5$ nm for parallel and perpendicular polarization of the IR beam, respectively.

Note that the perpendicular results give much higher intensity. However, the optimal length l is under 1 micron for both polarizations. Growing CNT forests below this optimal length can be difficult.

We may be able to increase l to more practical values by changing from $\lambda = 13.5$ nm for EUV lithography to $\lambda = 1$ nm for X-ray lithography (8). The advantage of 1 nm is that in this region carbon is transparent. This may increase the intensity and/or increase l to a more practical length. Neon-like copper is known to produce 1 nm xrays (9).

However, there does not appear to be much literature on the Coefficient of Efficiency for neon-like Cu as a function of laser intensity and Cu concentration. To determine the influence of C_E on the optimal l and ρ, we repeated the results for Sn and $\lambda = 13.5$ nm with C_E equal to a constant. The optimal l and ρ were about equal to the ones found previously, implying that they are weakly influenced by C_E. Assuming the same for Cu, we obtained the plots in Figures C.5 and C.6 with $C_E = 0.02$.

The optimal l for perpendicular is still below 1 micron, but at much higher intensity (assuming that C_E is indeed 2%). For parallel, l is extended to around 1 micron.

Upon further investigation, the CNT permittivity in the IR seems to be the greatest contributing factor to low l.

C.4 Conclusion

As technology grows, so will the need for a 13.5 nm light source with minimal debris. CNTs doped with Sn may be an efficient, reusable target material. Such target material would need to be less than a micron thick and have 20% or less mass density of Sn. The target may also be used with similar dimensions and mass density of Cu to produce 1 nm light for xray lithography.

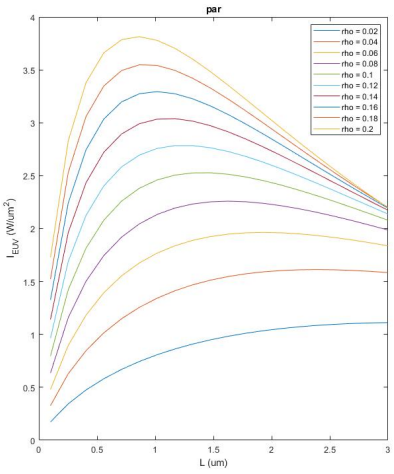

Figure C.5 I_{EUV} along optical axis just outside CNT forest infiltrate with ρ volume ratio of Cu with the IR laser polarization parallel to the CNT axis.

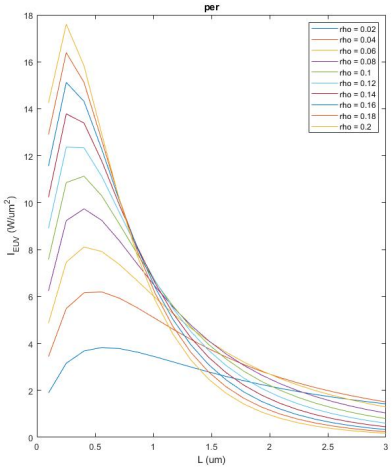

Figure C.6 I_{EUV} along optical axis just outside CNT forest infiltrate with ρ volume ratio of Cu with the IR laser polarization perpendicular to the CNT axis.

C.5 References

Bibliography

[1] D. Attwood and A. Sakdinawat. Cambridge University Press, 2 edition, 2016.

[2] S. et al. Harilal. Spectral control of emissions from tin doped targets for extreme ultraviolet lithography. *Journal of Physics D: Applied Physics*, 39:484–487, 2006.

[3] C. et al. Stanciu. Third-harmonic generation in carbon nanotubes: theory and experiment. volume 5352, 2004.

[4] J. et al Lehman. Carbon nanotube-based black coatings. *Applied Physics Reviews*, 5(011103), 2018.

[5] D. et al. Hutchison. Carbon nanotubes as a framework for high-aspect-ratio mems fabrication. *Journal of Microelectromechanical Systems*, 19(1):75–82, 2010.

[6] S. et al. Fujioka. Properties of ion debris emitted from laser-produced mass-limited plasmas for extreme ultraviolet light source applications. *Applied Physics Letters*, 87, 2005.

[7] Wikipedia contributors. Effective medium approximations — Wikipedia, the free encyclopedia, 2024. [Online; accessed 1-May-2024].

[8] F. Cerrina. X-ray imaging: applications to patterning and lithography. *Journal of Physics D: Applied Physics*, 33:R103–R116, 2000.

[9] CJ et al Gaeta. High-power compact laser-plasma source for x-ray lithography. *Japanese Journal of Applied Physics*, 41:4111–4121, 2002.

Appendix D

High harmonic generation from carbon nanotube collimators

D.1 Introduction

High harmonic generation (HHG) is a method of producing high energy radiation using nonlinear optics. A near-infrared laser illuminates a noble gas, causing inner electrons to tunnel out of an atom, oscillate, and return to the atom. The returning electron emits a photon of energy higher than that of the near-infrared laser, typically in the EUV regime. The EUV produced can be in femtosecond pulses, and is spatially coherent. However, the intensity may be low due to several effects. First, the gas absorbs a portion of the EUV. Second, due to infrared and EUV having different refractive indices through the gas, EUV emitted at the entrance of the gas portion is out of phase with the EUV emitted at the exit. This creates a "dephasing distance," beyond which destructive interference occurs (1). Efficient HHG sources must be developed with these issues in mind.

We considered using the CNT collimator to optimize HHG. The model is shown in Figures D.1 and D.2. Connected to one collimator is a gas leak, and the other a vacuum. As demonstrated earlier,

the high aspect ratio restricts gas flow from the leak to the vacuum, maintaining a desired pressure in the spacing between them. Because of the high electrical conductivity of CNTs (2), the infrared laser can be replaced by connecting the two collimators to a high frequency source. The collimators then act as a parallel-plate capacitor. The oscillating electric field between the collimators may cause HHG. The size of the columns can be designed to correlate with the EUV refractive index in the gas, thus eliminating concern for the dephasing distance. With the infrared laser removed, infrared filters can be removed, which may also increase the EUV intensity.

We will derive the necessary parameters for HHG. This is will begin with modelling the CNT collimators for a given photon energy U. The model will then be applied to EUV generation ($U = 91.84$ eV). The parameters for EUV generation will then judge if such a design is feasible/practical.

D.2 Theory

We determine the following in the given order:

- The necessary electric field E_0 for a given frequency ω to enable HHG for a desired photon energy U.
- The necessary pressure P for HHG.
- The structures' column width w and wall thickness t such that the photons with U are emitted in phase.
- The potential field and electric field between the structures.
- The necessary voltage V applied and expected gain G.

Steps 1, 2, 3, and 5 are done analytically. Step 4 is done using an iterative method. We begin with the equation for HHG emission (1):

$$U = 3.17\left(\frac{e^2E_0^2}{4m\omega^2}\right) + I_p \tag{D.1}$$

where e is the electron charge, m is the electron mass, and I_p is the ionization energy for the gas type. Rearranging this equation we have the electric field magnitude as a function of U, I_p, and ω:

$$E_0 = \omega(2.678579 \times 10^{-6})\sqrt{U - I_p} \tag{D.2}$$

where E_0 is in V/m, ω in rad/s, and U and I_p are in eV.

We can now substitute Eq D.2 into the function for the electron displacement outside the atom (1):

$$x(t) = \left(\frac{eE_0}{m\omega^2}\right)[(\cos\phi - \cos\phi_0) + (\phi - \phi_0)\sin\phi_0] \tag{D.3}$$

where $\phi = \omega t$ and for maximum return energy $\phi_0 = \pi/10$ (1). Finding the first maximum and taking the absolute value we have:

$$x_{max} \approx 5.29966956 \times 10^5 \frac{\sqrt{U - I_p}}{\omega} \tag{D.4}$$

in meters. If another ionized atom is located near this distance, the electron may combine with it instead of it's parent atom, releasing less energy than anticipated. To ensure this does not happen, we will restrict x_{max} to no more than half the distance between the parent and the other atom. The distance between atoms in a gas can be described using the mean free path λ_{mfp} (**?**):

$$\lambda_{mfp} = \frac{RT}{\pi d^2 N_A P\sqrt{2}} \tag{D.5}$$

where R is the universal gas constant (8.314 J/Kmol), T is temperature in K, d is the atom's diameter in m, N_A is Avogadro's number, and P is pressure in Pa.

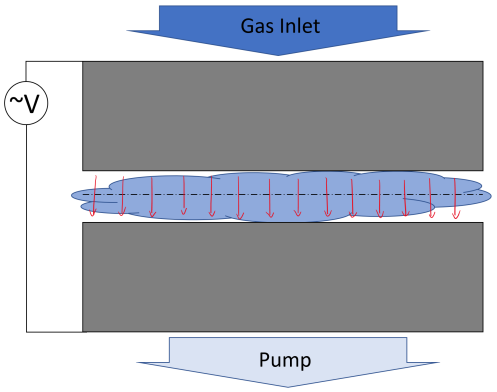

Figure D.1 Region between two parallel walls. The potential in the center (dotted line) is expected to be uniform, similar to a parallel-plate capacitor.

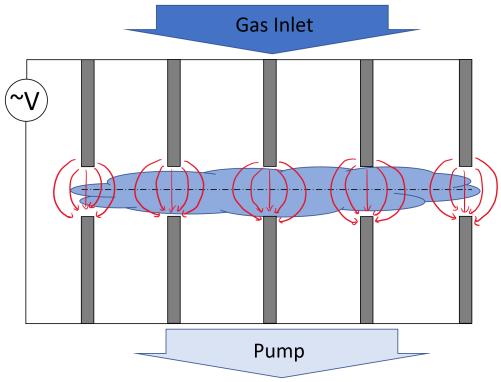

Figure D.2 Region between two columns. The potential in the center (dotted line) is expected to oscillate, with peaks between the cross walls.

We can set $\lambda_{mfp} = 2x_{max}$ and rearrange to solve for P:

$$P_{max} = 6.59696271 \times 10^{-6} \frac{\omega}{d^2\sqrt{U - I_p}} \tag{D.6}$$

where P_{max} is now in torr and d is now in pm, assuming room temperature $T = 300$K. Eq D.6 then gives the maximum pressure allowed for producing U energy photons at a driving frequency of ω for a gas with I_p ionization energy and d atomic diameter.

With the pressure known, the refractive index n for the desired photon energy U can be found using available EUV/SXR databases. We are now in a position to consider the dimensions of the structure. We assume that the two CNT structures used have the same dimensions and are perfectly aligned. There are two regions of interest, shown in Figures D.1 and D.2. Looking forward, we anticipate the electric field strength between the structures for D.1 to be fairly uniform, similar to a parallel plate capacitor. This will have a long pulse duration, which is undesirable for most HHG applications. We anticipate the electric field strength in D.2 to peak directly between the cross walls, and to decrease towards the center of the columns. The varying field strength may cause photons of varying energy to be emitted. We intend for the photons of desired energy U to be emitted at the

peak.

We consider a photon emitted at position 0. As it travels, it reaches position X at time T, where another photon is emitted. Two photons are emitted during one voltage period, therefore to be in phase, X must equal $(m+0.5)\lambda/n$, where λ is the wavelength in vacuum. For the second photon to be emitted when the first arrives, $T = \frac{\pi}{\omega}$. The phase velocity of the photon is then:

$$\frac{X}{T} = \frac{(m+0.5)\lambda\omega}{n\pi} = \frac{c}{n} \tag{D.7}$$

Solving for m we have:

$$m+0.5 = \frac{\pi c}{\lambda\omega} \tag{D.8}$$

We can then substitute this in to solve for X, and set X equal to a multiple (j) of $w+t$:

$$w+t = \frac{X}{j} \tag{D.9}$$

With the dimensions of the structures determined, we can then model the potential field between the two structures. This is done using a iterative method. We describe the region using a matrix, with spacing Δx. The potential at the walls is constant and normalized. We begin with all other regions equal to zero. We then calculate the potential at each point by taking the average of the neighboring points (excluding the walls):

$$\Phi(i,j) = \frac{1}{4}(\Phi(i+1,j)+\Phi(i-1,j)+\Phi(i,j+1)+\Phi(i,j-1)) \tag{D.10}$$

After each iteration we take the Euclidean norm of the distribution to observe convergence. When the norm stabilizes, we consider the resulting matrix the solution.

To calculate the electric field at a given point, we take the difference between the points before and after, divided by $2\Delta x$:

$$|E(i,j)| = \sqrt{\left(\frac{\Phi(i-1,j)-\Phi(i+1,j)}{2\Delta x}\right)^2 + \left(\frac{\Phi(i,j-1)-\Phi(i,j+1)}{2\Delta x}\right)^2} \tag{D.11}$$

Given the symmetry of the design, we anticipate the electric field along the center of the spacing to be perpendicular to the horizontal (refer to Fig D.2). Because the photons are emitted perpendicular to the electric field (1), the photons emitted along this line will be parallel to the horizontal, and therefore be able to exit the design. Photons emitted elsewhere will not be parallel, and therefore may strike the inner walls of the structures. Therefore we only need to consider the electric field along the center. Both the x and y components can then be plotted as functions of position along the horizontal, with the x component anticipated to be approximately zero.

In the iterative method, we set the voltages of the top and bottom structures to +1 and -1, respectively. Because the iterative method is linear, we can then scale the matrix by a constant C (in Volts) so that the voltage on the structures is $V = C(\pm 1) = C$, and that $C|E(i,j)| = E_0$ along the center. Determining this constant then gives us the necessary voltage applied to the CNT structures:

$$V = C = \frac{E_0}{|E(i,j)|} \tag{D.12}$$

The gain G is determined by summing the constructively interfering pulses within one decay length. The decay length is given (1):

$$l_{decay} = \frac{\lambda}{4\pi\beta} \tag{D.13}$$

The intensity of each pulse is reduced by

$$I = I_0 e^{\frac{-r}{l_{decay}}}, \tag{D.14}$$

where I_0 is a constant and r is the distance traveled. This is proportional to the electric field squared. Taking the square root to solve for the electric field, summing the fields for all the pulses within l_{decay}, then solving back for the intensity, we have:

$$G = \frac{I}{I_0} = \left(\sum_{i=0}^{n} e^{\frac{-iX}{2l_{decay}}} \right)^2 \tag{D.15}$$

Where $n = \lfloor l_{decay}/X \rfloor$.

Gas	I_p (eV)	d (pm)	E_0 (V/m)	P_{max} (torr)	δ	β
Neon	21.565	76	1.411E7	85.604	1.27E-6	1.36E-6
Argon	15.76	142	1.468E7	23.567	3.75E-7	1.13E-7
Krypton	14.00	176	1.485E7	15.167	-2.18E-8	2.67E-7
Xenon	12.13	216	1.503E7	9.951	-5.74E-8	8.71E-7

Table D.1 Materials' properties and subsequent calculated values. Ionization energies and atomic diameters were taken from ptable.com. Refractive indices were taken from CXRO.

D.3 Results and Discussion

We consider a HHG for a 13.5 nm wavelength ($U = 91.84$ eV). We restrict our study to neon, argon, krypton, and xenon. We consider a 100 GHz voltage source. With these parameters, we have the following values listed in Table D.1.

With the refractive indices, we can determine w and t. Solving for $m + 0.5$ in Eq D.8 we have $m \approx 111,034.2437$. Rounding this to 111,034.5 requires decreasing ω and P_{max} by 2.31E-4%. X is very close to a reasonable integer 1499 microns. This requires us to change the wavelength from 13.5 nm to 13.5003 nm (≈ 91.838 eV), which changes δ and β by no more than 0.4%, an effect we will consider negligible. If the wall thickness t is large, then the structure approaches Fig D.1, which we anticipate to have a long pulse duration. For short pulses, we'd like t as small as possible. Therefore we will set $t = 1$ micron, the resolution limit of CNT fabrication. w can have a maximum value of 1498 microns ($j = 1$ in Eq D.9). We can divide this into smaller regions within reason. Doing so would produce more pulses closer together. We will set $w = 374.75$ microns, which is possible with modern lithography.

Figure D.3 shows an example of the iterative process ran for $s = 0.95$ micron with $\Delta x = 0.05$; Figure D.4 provides a zoomed-in view of features. For all values of s, with 100 iterations the Euclidean norm varied by no more than 0.08%.

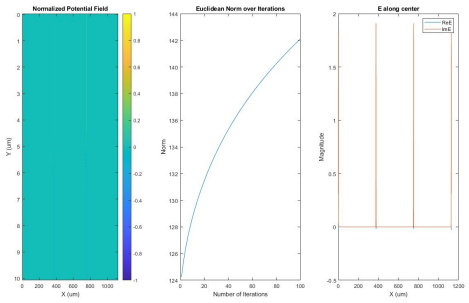

Figure D.3 Example of Iterative Method with $s = 0.95$ microns and a step size of 0.05 microns

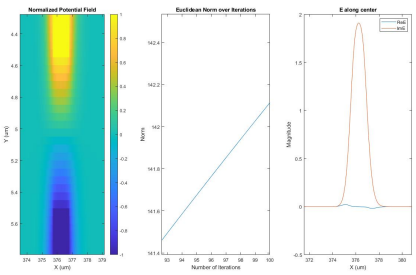

Figure D.4 Zoom-in view of example. Note that the nonzero E_x may be due to the discretization method.

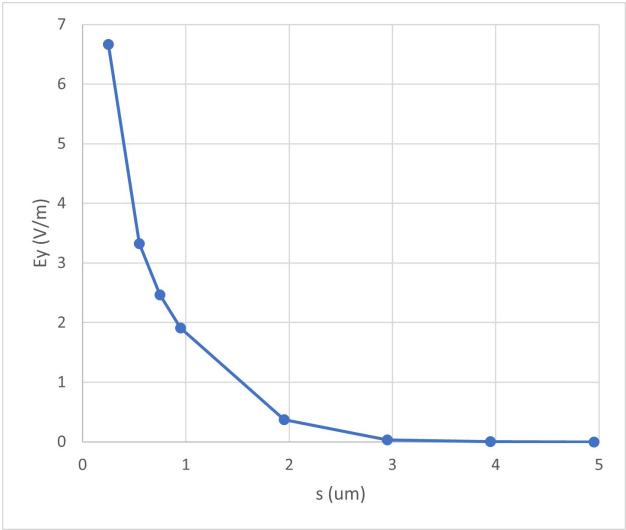

Figure D.5 $|E|$ along the center between the CNT structures as a function of s

Note that there is a small horizontal component of the electric field, which implies that the field along the center is not perpendicular to the horizontal. This may be due to the discretization of the potential in the iterative method. Therefore we will still consider $E_x = 0$.

Calculating $|E(i, j)|$ along the center for multiple values of s we obtain Figure D.5. Note that the electric field decays rapidly as the CNT collimators are moved further apart. Calculating for C, we find that in order to keep the applied voltage V under 10 MV, s must be less than about 1 micron.

Gas	P_{max} (torr)	V (MV)	L (mm)	Gain
Argon	23.567	7.69	8.994	31.3
Krypton	15.167	7.78	2.998	6.3

Table D.2 Parameters for a EUV HHG source

l_{decay} is too small for neon and xenon, therefore we consider only argon and krypton. For argon, $l_{decay} \approx 9507$ microns, which gives $G = 31.3$. For krypton, $l_{decay} = 4024$ microns and $G = 6.3$. These gains for argon and krypton can be obtained with CNT collimators 8.994 and 2.998 mm long, respectively. Longer structures can be made, but absorption will make any additional gain negligible.

The results for a 13.5003 nm HHG source, composed of two CNT structures with $w = 374.75$, $t = 1$, and $s = 0.95$ microns that are L long, ran at (about) 100 GHz are summarized in Table D.2.

The most difficult parameter to meet is perhaps the applied voltage. If we were to decrease the voltage to a more reasonable level, ω would also need to decrease. Conceptually this means that the tunnelled electron needs a longer trajectory to acquire the necessary energy for EUV emission. This would increase the mean free path λ_{mfp}, decreasing the pressure, decreasing the number of atoms present, decreasing the number of photons emitted, and therefore decrease the intensity. We can estimate the intensity decrease by considering a 2 dimensional array of atoms, spaced λ_{mfp} apart, between structures that are W wide. The number of atoms in the array are:

$$N = \frac{sW}{\lambda_{mfp}^2} \tag{D.16}$$

The probability that a given atom will emit a photon is on the order of $\rho = 10^{-1}$ to 10^{-2} (1). Then multiplying by the energy per photon U we have the energy per pulse.

$$E_{pulse} = \frac{sW\rho U}{\lambda_{mfp}^2} \tag{D.17}$$

If we assume the pulse's spatial length to be about equal to the structure's wall thickness t, the

duration of the whole pulse is t/c. We then divide by this duration and the area (sW), and multiply by the gain to get the EUV intensity in a single pulse:

$$I = \frac{\rho U c G}{\lambda_{mfp}^2 t} \tag{D.18}$$

For the pressures listed in Table D.2, we have about 63.8 mW/cm2 for argon and 12.5 mW/cm2 for krypton, assuming $T = 300$ K and $\rho = 10^{-2}$. Decreasing the necessary voltage to 7.69 and 7.78 kV, decreases ω to about 100 MHz, the pressures to 23.567 and 15.167 mtorr, and the intensities to 0.0638 and 0.0125 uW/cm2.

D.4 Conclusion

We modelled a pair of CNT collimators as electrodes for producing HHG. We determined the necessary dimensions, pressures, frequencies, and voltages for a given gas to produce 13.5 nm light. We found that if HHG is possible, argon would be the ideal gas for collimators with 1 μm thick walls, $\approx 375\mu$m wide columns, and $\approx 1\mu$m spacing with a 7.69 MV, 100 GHz source. Such would produce about 63.8 mW/cm2. Typical HHG sources obtain values of 10^6 to 10^{10} W/cm2 (1). We therefore conclude that HHG utilizing CNT collimators as electrodes would not be an effective EUV source.

D.5 References

Bibliography

[1] D. Attwood and A. Sakdinawat. Cambridge University Press, 2 edition, 2016.

[2] D. et al. Hutchison. Carbon nanotubes as a framework for high-aspect-ratio mems fabrication. *Journal of Microelectromechanical Systems*, 19(1):75–82, 2010.